DESY 95-232

Investigation of the Nonlinear Effects of Wiggler and Undulator Fields on the Beam Dynamics of Particle Storage Rings in the case of DORIS III

Dissertation
zur Erlangung des Doktorgrades
des Fachbereichs Physik
der Universität Hamburg

vorgelegt von
Winfried Decking
aus Ibbenbüren

Hamburg
1995

Gutachter der Disseration :	Prof. Dr. C. Kunz Dr. habil. J. Roßbach
Gutachter der Disputation :	Prof. Dr. R.D. Kohaupt Dr. habil. J. Roßbach
Datum der Disputation :	10.8.1995
Sprecher des Fachbereichs Physik und Vorsitzender des Promotionsausschusses :	Prof. Dr. B. Kramer

Zusammenfassung

In dieser Doktorarbeit untersuche ich den nichtlinearen Einfluß von Wiggler- und Undulatormagnetfeldern auf die Strahldynamik von Speicherringen. Als Beispiel dient DORIS III, DESY's Synchrotronstrahlungsquelle.

Wiggler und Undulatoren werden in Speicherringen zur Erzeugung hochintensiver Synchrotronstrahlung oder zur Kontrolle der Strahldimensionen eingesetzt. Die Benutzung dieser Magnetstrukturen in Speicherringen ist wegen der stark nichtlinearen Struktur der Magnetfelder nicht unproblematisch. Eine detailierte Analyse der nichtlinearen Dynamik der gespeicherten Teilchen unter dem Einfluß der Wigglerfelder und deren Feldfehler ist deshalb erforderlich und liegt mit dieser Arbeit vor.

Das Problem wird dabei auf analytischer, numerischer und experimenteller Ebene behandelt.

Der analytische Zugang erfolgt mit Hilfe einer störungstheoretischen Behandlung der entsprechenden Hamiltonfunktion. Als Magnetfeldbeschreibung wird hierbei eine Fourierserie verwandt, die die wesentlichen Merkmale von Wiggler- und Undulatorfeldern enthält. Wichtigster Einfluß der idealen Wiggler und Undulatoren ist die Anregung von zusätzlichen Synchro-Betatronresonanzen vierter Ordnung.

Um Feldfehler und andere Details der Magnetfelder zu erfassen, ermittle ich das Magnetfeld durch die Integration über geeignet verteilte magnetische Flächenladungsdichten. Dies erlaubt eine einfache Modellierung verschiedenster Parameter wie Breite der Magnetpole, Periodizitäts- und Gradientenfehler.

Die Bewegungsgleichungen in den so berechneten Feldern lassen sich nur numerisch integrieren. Dies ist für die Verwendung in Teilchenverfolgungsprogrammen viel zu langsam, deshalb wird eine Transferfunktion, basierend auf der numerischen Taylorentwicklung einer entsprechenden Erzeugungsfunktion, berechnet.

Die numerische Analyse der Strahldynamik unter dem Einfluß der Wigglerfelder mit verschiedensten zusätzlichen Parametern ist dadurch möglich. Kriterien für die aus strahldynamischer Sicht nötigen Polbreiten und tolerierbaren Feldfehler werden erstellt.

Einen Hauptteil der Arbeit stellt die experimentelle Charakterisierung der Wigglereinflüsse auf DORIS III dar. Dabei untersuche ich lineare und nichtlineare Effekte, wie Änderung des Q-Wertes und der geschlossenen Bahn, Anregung von Resonanzen, Strahlprofile sowie dynamische Akzeptanzen. Spezielle Experimente zu den Einflüssen der Polbreite und von Multipolfehlern in Wigglern werden durchgeführt. Die experimentellen Ergebnisse stimmen, unter Berücksichtigung der Magnetfeldmessungen, mit den theoretischen Vorhersagen überein. Der Haupteffekt der Wiggler besteht in der analytisch vorhergesagten Anregung von Synchro-Betatronresonanzen vierter Ordnung. Feldfehler führen zu zusätzlichen Resonanzen und einer Verringerung der horizontalen dynamischen Akzeptanz in DORIS III.

Ein Experiment an der Advanced Light Source in Berkeley zeigt den Einfluß eines Undulators auf eine Synchrotronstrahlungsquelle der sogenannten dritten Generation.

Abstract

In this thesis I analyze the effects of wiggler and undulator magnetic fields on the beam dynamics of electron/positron storage rings. DORIS III, DESY's synchrotron radiation source is taken as an example.

Wigglers and undulators are used for the production of synchrotron radiation or to control beam sizes in storage rings. Their introduction in the lattices of storage rings causes some problems due to the strong nonlinearities of the magnetic fields. Therefore a detailed analysis of the particle dynamics under the influence of wiggler magnetic fields and their field errors is necessary. This thesis provides such an analysis.

The problem will be attacked analytically, numerically and experimentally.

The analytic approach is based on the treatment of the appropriate Hamiltonian with perturbation theory. The magnetic fields are described with a Fourier series, which covers the main characteristics of wiggler and undulator fields. The main effect of wigglers and undulators is the excitation of fourth order synchro-betatron resonances.

The description of field errors and other details of the magnetic fields is achieved by integrating over appropriately distributed current sheets. This allows the modeling of different parameters such as magnet pole width, periodicity errors and errors in the field gradients.

The equations of motion in the fields calculated with this method can only be integrated numerically. This would be much too slow to be used in particle tracking codes. Therefore a transfer map based on the numerical Taylor expansion of an appropriate generating function is calculated.

The transfer map allows the numerical analysis of the beam dynamics of DORIS III under the influence of wigglers and undulators for various sets of parameters. Criteria for the pole width, periodicity errors and tolerable multipoles are developed.

A main part of this work is the experimental characterization of the wiggler effects in DORIS III. I investigate linear and nonlinear beam parameters, such as tune shifts, closed orbit variations, resonances, beam profiles and dynamic acceptances. Dedicated experiments on the influence of pole width and multipole errors of wiggler fields are performed. The experimental results agree with theoretical predictions, if field measurements of the wigglers and undulators are taken into account. The main effect of the wigglers on DORIS III is the excitation of fourth order synchro-betatron resonances, as predicted by the analytic theory. Field errors lead to additional resonance excitations and a reduction of the horizontal dynamic acceptance of DORIS III.

An experiment at the Advanced Light Source in Berkeley shows the influence of an undulator on a so-called third generation light source.

Contents

1 Introduction **1**

2 Magnetic Fields of Wigglers and Undulators **4**
2.1 Synchrotron Radiation from Wigglers and Undulators 4
2.2 Analytical Description of Wiggler Fields 6
2.3 Types of Insertion Devices 8
2.3.1 Pure Permanent Magnet Arrays 8
2.3.2 Hybrid Devices 9
2.3.3 Electromagnetic Devices 10
2.4 Comparison of the Series Expansion and the Current Sheet Method . . . 10
2.5 Magnetic Field Errors in Wigglers and Undulators 12
2.6 Multipole Expansion of Measured Field Integrals 13
2.7 Modeling of Field Errors with the Current Sheet Method 16

3 Single Particle Motion in a Storage Ring with Wigglers **18**
3.1 The Equations of Motion in a Storage Ring 18
3.2 Perturbation Theory 22
3.3 The Hamiltonian of a Wiggler 23
3.4 Numerical Analysis of Particle Dynamics 27
3.5 Transfer Maps for Arbitrary Magnetic Fields 29
3.6 Comparison of the Different Transfer Maps for Wigglers 34

4 Numerical Investigation of Wiggler Effects **39**
4.1 General Remarks 39
4.2 The Synchrotron Radiation Source DORIS III 40
4.2.1 Wigglers and Undulators at DORIS III 43
4.3 Effects of Field Errors 44
4.3.1 Periodicity Error 44
4.3.2 Pole Width 44
4.3.3 Multipole Errors 46
4.4 Tracking Studies for DORIS III 49
4.4.1 Resonances 49
4.4.2 Dynamic Acceptance 49

5 Measurements of Wiggler Effects on Beam Characteristics **54**
5.1 Linear Effects 54
5.1.1 Intrinsic Linear Focusing 54
5.1.2 Closed Orbit Distortion due to Field Errors 56
5.2 Nonlinear Tune Shift with Amplitude 59
5.3 Resonances 60
5.3.1 Resonances in the Vicinity of $Q_y = 4.75$ 61
5.3.2 Resonances in the Vicinity of $Q_y = 4.25$ 64
5.4 Beam Profiles 66
5.5 Acceptance 69
5.6 Measurements in the Fringe Field 70
5.7 Wiggler with Large Multipole Errors 72
5.8 Influence of an Undulator on the Advanced Light Source 73
5.8.1 The 3rd Generation Light Source ALS 73
5.8.2 Measurement of Resonance Excitation caused by an Undulator . . 75

6 Summary **79**

Appendix **82**
A Numerical Evaluation of Multipole Coefficients from Field Integral Measurements 82
B Beam Lifetime in Electron Storage Rings 83
C Parameter Lists of DORIS III and the ALS 84

Bibliography **88**

1 Introduction

Light is one of the most important tools of natural science: it enables us to view the universe - from galaxies down to atoms. Until the end of the last century, only the small portion of the spectrum of light which covers the visible light was obtainable, which allowed the investigation of structures down to a few μm. The discovery of X-rays opened the door to smaller dimensions, and the ongoing development of particle accelerators pushes the frontier further down to smaller and smaller dimensions. Figure 1.1 displays the spectrum of light from gamma rays to radiowaves showing the corresponding wavelength and photon energies together with objects of comparable size along the bottom and artificial light sources which are built to produce the light along the top.

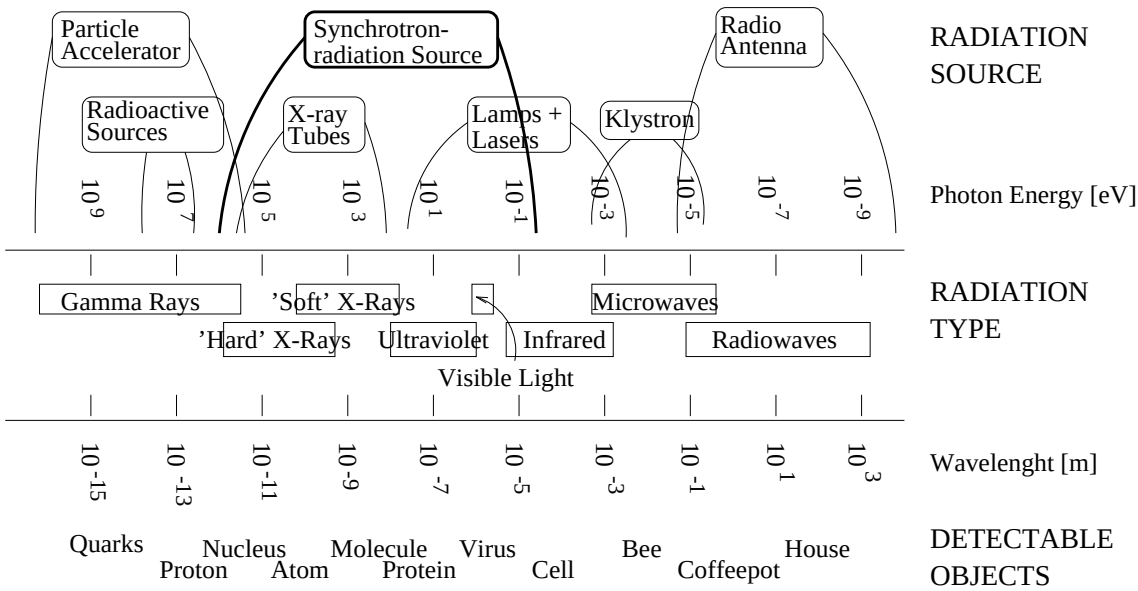

Figure 1.1: *The spectrum of light from gamma rays to radiowaves with artificial sources of the light along the top and objects of comparable size to the wavelength along the bottom (from [Win87])*

But it is not only the wavelength which allows the observation of a certain object. The resolution of an experiment using light is determined by the amount of light which is emitted within a certain area and solid angle, giving the spot size and the photon flux on the probe. This parameter is named the brilliance of a light source.

Synchrotron radiation is one of the most powerful and general light sources available today. Synchrotron radiation is emitted by accelerated moving charged particles and was first observed in an electron synchrotron in 1947. Its unique properties are:

- Continuous spectrum: Synchrotron radiation is emitted in a broad continuous spectrum from infrared to 'hard' X-rays, which allows a wide range of experiments covering the investigation of objects from cells to the nucleus of atoms (see figure 1.1, where the spectral range covered by synchrotron radiation is emphasized). Easy tuning and variation of the wavelength is another advantage of the broad spectrum.

- High flux: The flux of photons in a given frequency interval is usually higher than from any other light source (X-ray tube or laser) available.

- High brightness: The strong forward emission of synchrotron light and the small size of the source (the electron beam) allows for highest brightness.

- Time structure: The bunched structure of a stored electron beam leads to the same time structure of the synchrotron radiation, which enables time resolved experiments.

After the potential of these properties was recognized, synchrotron radiation experiments were started at storage rings or synchrotrons which were built specifically for high energy physics. These parasitically used storage rings are called the 1st generation of synchrotron light sources. The steadily growing demand on these sources lead to the construction of dedicated synchrotron light sources (the 2nd generation), optimized for the requirements of the synchrotron radiation users. The invention of wigglers and undulators, special magnet structures which allow the photon flux and the brilliance to be increased by several orders of magnitudes, made the design of the next generation of synchrotron light sources necessary. These storage rings allow the operation of many wigglers and undulators and are optimized for smallest source sizes. In the meantime, many of these 3rd generation light sources are in operation or under construction worldwide, and some of the older storage rings have been reconstructed to match the requirements for the installation of wigglers and undulators. The next generation of synchrotron light sources, using the concept of free electron lasers, comes in sight.

These developments were accompanied by several problems dealing with experimental techniques and photon beam line designs, as well as with the solution of problems concerning the physics of storage rings serving as synchrotron radiation sources. Introducing wigglers and undulators as magnetic structures into the storage ring magnet lattices, the effects of these structures on the stored electron[a] beam have to be investigated.

The topic of this thesis is to provide such an investigation, leading to a further understanding of the effects of wigglers[b] on the nonlinear beam dynamics. Several authors have already attacked this problem analytically, numerically or experimentally (see for example [Smi86], [Wru88], [Bru92], [KB90]).

I will develop and apply numerical tools which take into account not only the ideal magnetic fields of wigglers but also magnetic field errors and their influence with respect

[a] Some of the synchrotron light sources are operated with positrons. The beam dynamics of positrons and electrons is similar, thus I will not distinguish between them in the following.

[b] The name 'wiggler' will be used to include both wigglers and undulators unless a distinction between them is necessary.

to the undulating electron path in a wiggler. These lead to tolerance criteria for the design and construction of wigglers and undulators.

The main part of this thesis is the experimental proof of the analytical and numerical predictions as well as a characterization of non-predicted wiggler effects by dedicated beam dynamics experiments. These experiments have been performed at the storage ring DORIS III of the Deutsches Elektronen-Synchrotron (DESY) in Hamburg and at the Advanced Light Source (ALS) at the Lawrence Berkeley Laboratory (LBL) in Berkeley. DORIS III is a state of the art 1st generation light source, which was reconstructed to provide space for up to 10 wigglers and undulators. The ALS is one of the first operating 3rd generation sources. Due to the dissimilarities of both storage rings, different problems could be investigated.

The procedure will be as follows:
First the magnetic fields of wigglers and undulators are introduced and the different field descriptions are compared with respect to their usefulness in theoretical beam dynamics investigations. The various treatments of field errors as multipole expansions of the field integrals or by an individual field modeling with the current sheet method are described.

The following chapter explains some accelerator physics concepts and gives an analytical treatment of the nonlinear beam dynamics in the presence of wiggler fields, based on a 6-dimensional Hamiltonian theory. The basic concepts of single particle tracking are introduced. The various treatments of wiggler fields in tracking codes are developed and compared.

In chapter 4 numerical investigations of different wiggler field errors and field characteristics, such as pole width, periodicity errors and field gradient errors are presented for DORIS III. The resonance pattern and the dynamic aperture is evaluated.

The 5th chapter summarizes the results of the experiments performed at DORIS III and the ALS. Linear and nonlinear effects of wigglers are measured and compared with analytical and numerical results.

The results and conclusions are presented in chapter 6, and an outlook on further applications of the described techniques will be given.

2 Magnetic Fields of Wigglers and Undulators

The basis of every investigation of the effects of wigglers on beam dynamics is an adequate description of the magnetic fields. As an introduction, the main characteristics of the radiation spectra emitted from bending magnets, wigglers and undulators will be summarized. The different design possibilities for building a wiggler or undulator are presented. The generally used analytic description of the magnetic field is given and compared with the real fields. A discussion of wiggler and undulator field errors follows, including a possible description of these errors for studies of the beam dynamics.

2.1 Synchrotron Radiation from Wigglers and Undulators

The radiation emitted from a relativistically moving charge is evaluated in several textbooks (see for example [Jac82]). The radiative part of the electric ($\vec{E}$) and magnetic ($\vec{B}$) fields observed far away from the charge is[a]:

$$\vec{E}(t) = \frac{\mathrm{e}}{4\pi\varepsilon_0 \mathrm{c}} \left(\frac{\vec{n} \times ((\vec{n} - \vec{\beta}) \times \dot{\vec{\beta}})}{(1 - \vec{n}\vec{\beta})^3 R} \right)_{\text{at } t_{ret.}} \tag{2.1}$$

$$\vec{B}(t) = \left(\frac{\vec{n} \times \vec{E}}{\mathrm{c}} \right)_{\text{at } t_{ret.}} . \tag{2.2}$$

Where e is the electron charge, c the speed of light, ε_0 the permittivity of free space, $\vec{n}$ and R represent the direction and distance between charge and observer, $\vec{\beta}$ the normalized velocity of the charge, and the equations in brackets have to be evaluated at the retarded time $t_{ret.} = t - R(t_{ret.})/\mathrm{c}$, which takes into account the time of travel of the electromagnetic wave from the charge to the observer. With these formulae, one can evaluate the emitted power or photon flux distribution in space and frequency. For simple geometries such as constantly curved orbits analytical solutions exist, while in other cases one has to compute the electric fields by calculating the motion of a charged particle numerically through guide fields of any kind.

In principle one distinguishes between three different sources of synchrotron radiation:

[a] MKSA-units will be used throughout this work.

• Bending Magnets

Bending magnets are the 'natural' source of the synchrotron radiation in storage rings. They produce a constant magnetic field B, which bends particles with impulse p on a curve with the inverse radius

$$\frac{1}{\rho} = \frac{\mathrm{e}}{p} B \quad . \tag{2.3}$$

The properties of synchrotron radiation from a bending magnet have been calculated analytically by various authors (first by [Sch49], for an overview see [Hof90]). The photons are mainly emitted into a small cone with an opening angle $\sim \frac{1}{\gamma}$ (where $\gamma = \frac{E}{\mathrm{m_0 c^2}}$ the ratio between the energy of the particle and its rest energy) in the plane of motion of the charge and perpendicular to the direction of the acting force. The photon frequency spectrum is divided into two halves by the critical frequency $\omega_c = \frac{3c\gamma^3}{2\rho}$, e.g. half of the photons are emitted with energies above/below ω_c.

• Wigglers

A Wiggler is a device which consists of a chain of alternating bending magnets. The particles pass through the alternating magnetic field, emitting synchrotron radiation with similar spectral properties to that from a bending magnet, but with higher photon flux into a certain observation angle.

• Undulators

An Undulator is a wiggler with a very short period length. The dimensionless, so-called undulator parameter

$$K = \frac{\mathrm{e}}{2\pi \mathrm{m_0 c}} B_{max}\, \lambda = 0.934\, B_{max}[\mathrm{Tesla}]\, \lambda[\mathrm{cm}] \tag{2.4}$$

helps to distinguish between wigglers and undulators. B is the maximum magnetic field on the axis of the undulator and λ the period length of the undulator. K gives the ratio of the peak angular deviation of the electron path from the undulator axis and the opening angle of the radiation cone. A device with $K < 1$ is called an undulator, with $K \gg 1$ is called a wiggler. The border between these devices is floating. The small period length of an undulator leads to an emission of most of the photons within a small cone ($\sim \frac{1}{\gamma}$) around the undulator axis. This enables a constructive interference between the emitted photons at certain 'resonant' wavelengths λ_r. This wavelength also depends on the directions of observation θ_x, θ_y and is:

$$\lambda_r = \frac{\lambda}{2\gamma^2}\left(1 + \frac{K^2}{2} + \gamma^2(\theta_x^2 + \theta_y^2)\right) \quad . \tag{2.5}$$

Figure 2.1 shows the photon flux per second, normalized to an unit solid angle and unit source size in a relative bandwidth. This value is generally known as brilliance:

$$brilliance = \frac{flux}{4\pi^2 \Sigma_x\, \Sigma_y\, \Sigma_{x'}\, \Sigma_{y'}}$$

where $\Sigma_{x,y}$ is the effective horizontal and vertical source size and $\Sigma_{x',y'}$ the effective divergence which is obtained by adding quadratically the contributions of the beam emittance and the opening angle of the radiation. The spectra are calculated for different devices at the storage rings DORIS III, BESSY II [BES89], PETRA [BBH+95] and

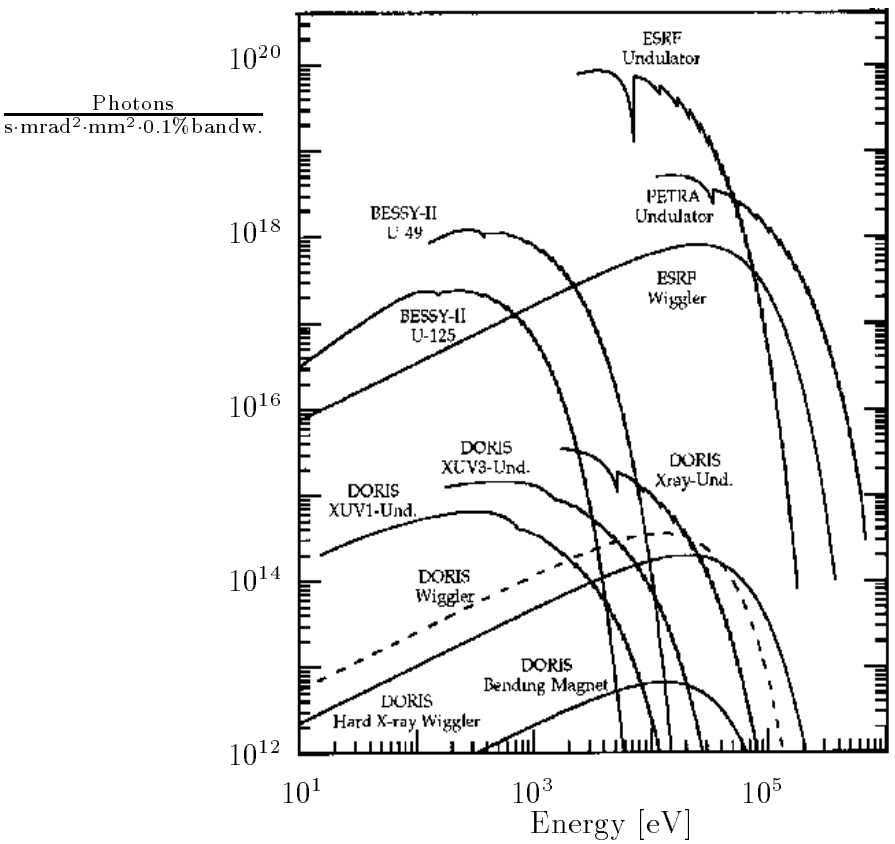

Figure 2.1: *Spectral brilliance of synchrotron radiation produced by different wigglers and undulators in different storage rings (from [Gür]). Typical beam currents have been assumed for all storage rings (100mA for DORIS and BESSY II, 60mA for PETRA and 200mA for the ESRF).*

ESRF [Hän92]. The higher brilliance of the latter is due to their smaller emittances, i.e. source sizes. The resonant increase of the brilliance of an undulator at certain frequencies can be seen, and also the increase in brilliance between the DORIS wiggler and bending magnets, which have comparable magnetic field amplitudes.

2.2 Analytical Description of Wiggler Fields

In this chapter the basic properties of the magnetic fields of wigglers and undulators will be discussed. Any description of the magnetic fields has to fulfill Maxwell's equations in free space

$$\vec{\nabla}\,\vec{B} = 0 \qquad\qquad \vec{\nabla} \times \vec{B} = \vec{0} \tag{2.6}$$

where the vector operator $\vec{\nabla}$ is in cartesian coordinates:

$$\vec{\nabla} = \left(\frac{\partial}{\partial x}, \frac{\partial}{\partial y}, \frac{\partial}{\partial z}\right) \quad .$$

This, together with the need for periodicity and some basic symmetry conditions leads to the field description for planar devices, which was first suggested by Halbach [Hal81]:

$$\begin{aligned} B_x &= \frac{k_x}{k_y} B_1 \sinh(k_x x) \sinh(k_y y) \cos(kz) \\ B_y &= B_1 \cosh(k_x x) \cosh(k_y y) \cos(kz) \\ B_z &= -\frac{k}{k_y} B_1 \cosh(k_x x) \sinh(k_y y) \sin(kz) \end{aligned} \tag{2.7}$$

where the coefficients $k_x,\ k_y$ are related by

$$k_x^2 + k_y^2 = k^2 = \left(\frac{2\pi}{\lambda}\right)^2 \tag{2.8}$$

in order to fulfill Maxwell's equations. The field is described in a right handed cartesian coordinate system with z the longitudinal axis through the wiggler, x the horizontal and y the vertical direction (see figure 2.2). B_1 is the on-axis vertical field amplitude. Depending on the horizontal wave number k_x, these equations describe a different behavior of the fields for varying horizontal displacements:

$$\begin{aligned} k_x = 0 \quad &: \quad \partial B_y/\partial x = 0, \text{ i.e. horizontally infinitesimal extended blocks} \\ k_x = \text{imaginary} \quad &: \quad \partial B_y/\partial x < 0, \text{ wigglers with planar poles} \\ k_x = \text{real} \quad &: \quad \partial B_y/\partial x > 0, \text{ wigglers with a different (concave) pole shape} \quad . \end{aligned}$$

The scalar (V) and vector potential ($\vec{A}$) will also be used in the following. They are related to the magnetic fields by:

$$\vec{B} = \vec{\nabla} \times \vec{A} \qquad\qquad \vec{B} = \vec{\nabla} \cdot V \quad .$$

This gives

$$V = -\frac{B_1}{k_y} \cosh(k_x x) \sinh(k_y y) \cos(kz) \tag{2.9}$$

$$\begin{aligned} A_x &= \frac{B_1}{k} \cosh(k_x x) \cosh(k_y y) \sin(kz) \\ A_y &= -\frac{B_1}{k} \frac{k_x}{k_y} \sinh(k_x x) \sinh(k_y y) \sin(kz) \\ A_z &= 0 \quad . \end{aligned} \tag{2.10}$$

where the vector potential has been chosen in a simple form (gauge transformation). Equations (2.7) serve as the first terms of a series expansion of the form:

$$\vec{B} = \sum_{n=1}^{N} B_n \vec{f}_n(k_{x,n}, k_{y,n}, nk, x, y, z) \qquad \text{with} \qquad k_{x,n}^2 + k_{y,n}^2 = (nk)^2 \tag{2.11}$$

where the function $\vec{f}_n$ is of the form described in (2.7) and B_n is the field amplitude of the different harmonics. This set of equations forms the basis for most of the analysis of wiggler effects on beam dynamics. They have the advantage of a closed analytic form and are relatively simple. On the other hand, a complete description of the magnetic fields is only possible with a large number of harmonics, choosing the ratio $(k_{x,n}/k_{y,n})^2$ in a sufficient way for every harmonic. Therefore a comparison of the series expansion (2.11) with a more realistic field model will be given in chapter 2.4.

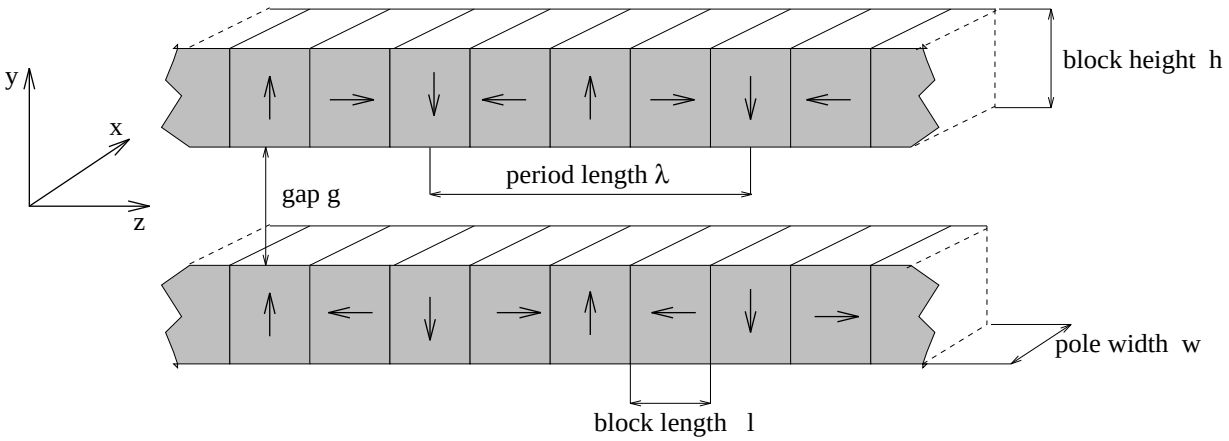

Figure 2.2: *Section of a permanent magnet array together with the definition of the cartesian coordinate system and of the geometrical dimensions block length l, block height h and pole width w of a permanent magnet block. The arrows indicate the direction of magnetization of each block.*

2.3 Types of Insertion Devices

2.3.1 Pure Permanent Magnet Arrays

Pure permanent magnets play an important role in the construction of insertion devices. Permanent magnets used in undulator design are out of NdFeB or SmCo. These unique materials give remanent magnetic fields of $B_r = 0.9 - 1.35\mathrm{T}$ with an approximately linear magnetization curve with unit slope, i.e. the magnetic permeability μ is in the range $1.0 - 1.1$. This allows an analytical calculation of the fields of a permanent magnet block as well as the superposition of field components from different magnet blocks. The field of a permanent magnet block can be calculated by the current sheet method. Due to the unit permeability of the material, the block can be treated as free space with current sheets on its surfaces. The field is calculated by integrating over each block surface [FP82]:

$$\vec{B} = -\frac{\mu_0}{4\pi} \int\int \frac{(\vec{M}\cdot\vec{r})\vec{dn} - (\vec{r}\cdot\vec{dn})\vec{M}}{r^3} \tag{2.12}$$

where μ_0 is the permeability of free space, $\vec{n}$ is the vector normal to the block surface, $\vec{M}$ the magnetization vector and $\vec{r}$ the radius vector to the field point.

In the case of cubic blocks with block faces parallel to the cartesian coordinate axes, the integration can be performed analytically and involves a summation of the contributions of each of the block corners. This model allows the computation of the fields inside the gap of a pure permanent wiggler.

Planar wigglers are constructed out of two parallel arrays of permanent magnet blocks with alternating direction of magnetization (see figure 2.2). The on-axis field amplitudes of the different harmonics of a two-dimensional undulator (i.e. horizontally infinitesimal extended blocks) can be calculated by:

$$B_n = 2B_r \exp(-nkg/2)(1 - \exp(-nkh))\sin(n\pi\, l/\lambda)/(n\alpha/2) \tag{2.13}$$

with $n = \frac{2\pi}{\alpha}m + 1,\ m = 0, 1, 2, \cdots, N$, where α is the rotation angle of the magnetization

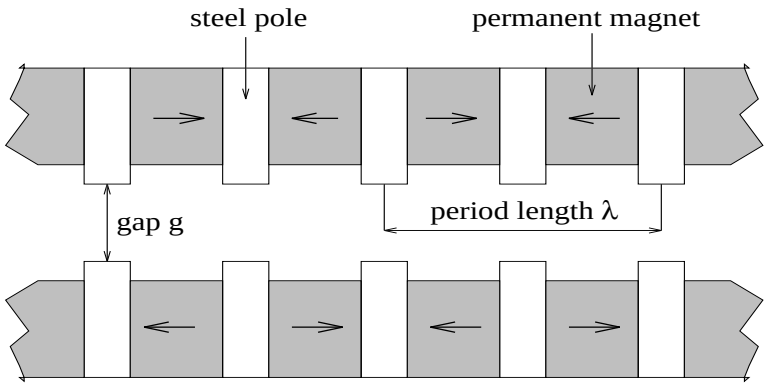

Figure 2.3: *Section of a hybrid wiggler with the field forming steel poles and the permanent magnets in between.*

vector between neighboring permanent magnet blocks (i.e. 90^o in figure 2.2) and B_r the remanent field, g the magnet gap, h the block height and l the block length, as defined in figure 2.2. N denotes the number of terms $\neq 0$ in the expansion. The order O of the expansion is then: $O = \frac{2\pi}{\alpha}N + 1$. As long as the magnet gap is small compared to the pole width, the above field amplitudes can also be used in the three-dimensional series expansion (2.11).

2.3.2 Hybrid Devices

Hybrid arrays combine field forming poles made of high permeability material (for example stainless steel) with field generating permanent magnet blocks (see figure 2.3). This gives the possibility of reaching high fields within smaller dimensions than when the magnetic fields are excited with coils. This can be seen by a simple scaling law: The same field in smaller dimensions is obtained by just scaling all components in the permanent magnet device, while the current density of an electromagnetic device increases inverse proportionally to the dimensions. The advantage over pure permanent magnet devices is a smaller sensitivity to permanent magnet magnetization errors and an easier possibility of forming the field by varying the pole geometry.

The field form and amplitude cannot be calculated analytically and must be computed with the help of two- or three-dimensional computer codes (such as PANDIRA [H$^+$] or MAFIA [B$^+$90]). Nevertheless, there exist empirical formulas to describe the dependence of the peak magnetic field [BHHW83] on the gap height:

$$B_{max} = k_1 \exp\left(-g(k_2 - k_3 g/\lambda)/\lambda\right) \tag{2.14}$$

with g the gap, λ the period length and k_{1-3} three empirical constants which vary due to the permanent magnet material and magnet design. These values are for example $k_1 = 3.33$, $k_2 = 5.47$, $k_3 = 1.8$ for a pure SmCo wiggler. Equation (2.14) is only valid for a certain range of g/λ, i.e $0.07 \leq g/\lambda \leq 0.7$ for the example above.

Hybrid arrays can be modeled with the current sheet method by assuming that the poles consist of permanent magnets with a very high remanent field ($B_r \geq 2$T), which is chosen to match the on-axis field. This method cannot be used for magnet design,

but it does allow an easy modeling of a hybrid wiggler, whereby parameters such as the pole width or magnet errors can be changed.

The fields in an area of $x \leq \pm$polewidth/2, $y \leq \pm$gap/1.2 around the wiggler axis can be described with the series expansion (2.11), with stronger higher order harmonics than in the permanent magnet array case.

2.3.3 Electromagnetic Devices

For completeness electromagnetic magnets are also mentioned. In conventional magnets the poles are excited by normalconducting current coils, or the field is generated by an appropriate current distribution in superconducting coils. Short period lengths and the demand of high magnetic fields lead to high current densities, which make it difficult to build such wigglers out of conventional electromagnetic magnets. High fields can be generated only in pulsed magnets of this type.

Superconducting coils can overcome this problem. They are commonly used for long period, high field devices (wave length shifter) or short period and small gap helical devices, proposed for example for linear collider schemes or single pass free electron lasers.

2.4 Comparison of the Series Expansion and the Current Sheet Method

The formulas (2.7) and (2.11) are used in the analytical treatment of wiggler effects on the beam dynamics. We will compare these formulas with the fields obtained from calculations by the current sheet method (see (2.12)).

The upper row of figure 2.4 shows the difference between the series expansion (2.11) and the current sheet model of a pure permanent magnet undulator, i.e. a wiggler with a short period length. The parameters are given in table 2.1. The series is truncated at the 9th harmonic, because the field amplitudes of the higher harmonics do not contribute significantly (see table 2.1). The ratio $(k_x/k_y)^2$ is fixed for all harmonics. The longitudinal behavior of the field as well as the dependence on the vertical position agree within an error of $\leq 0.01\%$, which is absolutely sufficient for the studies of beam dynamics. The horizontal field gradient is adequately described within approximately the half pole width.

The field of a hybrid wiggler is shown in the lower row of figure 2.4. The parameters are fitted to obtain a field comparable with the X-ray wiggler at DORIS (see appendix C). As can be seen in table 2.1, this wiggler has much stronger higher harmonics. The expansion up to the 9th harmonics gives a suitable description of the longitudinal and vertical behavior of the field. The field dependence on the horizontal position agrees again within approximately half of the pole width.

The poor agreement in the horizontal direction is due to the fixed ratio of $(k_x/k_y)^2$. We have overcome this problem by using the current sheet model instead of the expansion series for all investigations which are sensitive on the pole width.

Table 2.1: *Parameters and field amplitudes of the different harmonics of the pure permanent magnet undulator and the hybrid wiggler used for the field calculations*

	pure permanent magnet undulator	hybrid wiggler
λ [m]	0.03	0.14
gap [mm]	15	30
pole width [mm]	80	100
$(k_x/k_y)^2$	$-9.0 \cdot 10^{-4}$	-0.0625
B_1 [T]	0.4865	1.0723
B_3/B_1	0.0000	0.1035
B_5/B_1	$-3.7 \cdot 10^{-4}$	-0.0162
B_7/B_1	0.0000	-0.0030
B_9/B_1	0.0000	0.0006

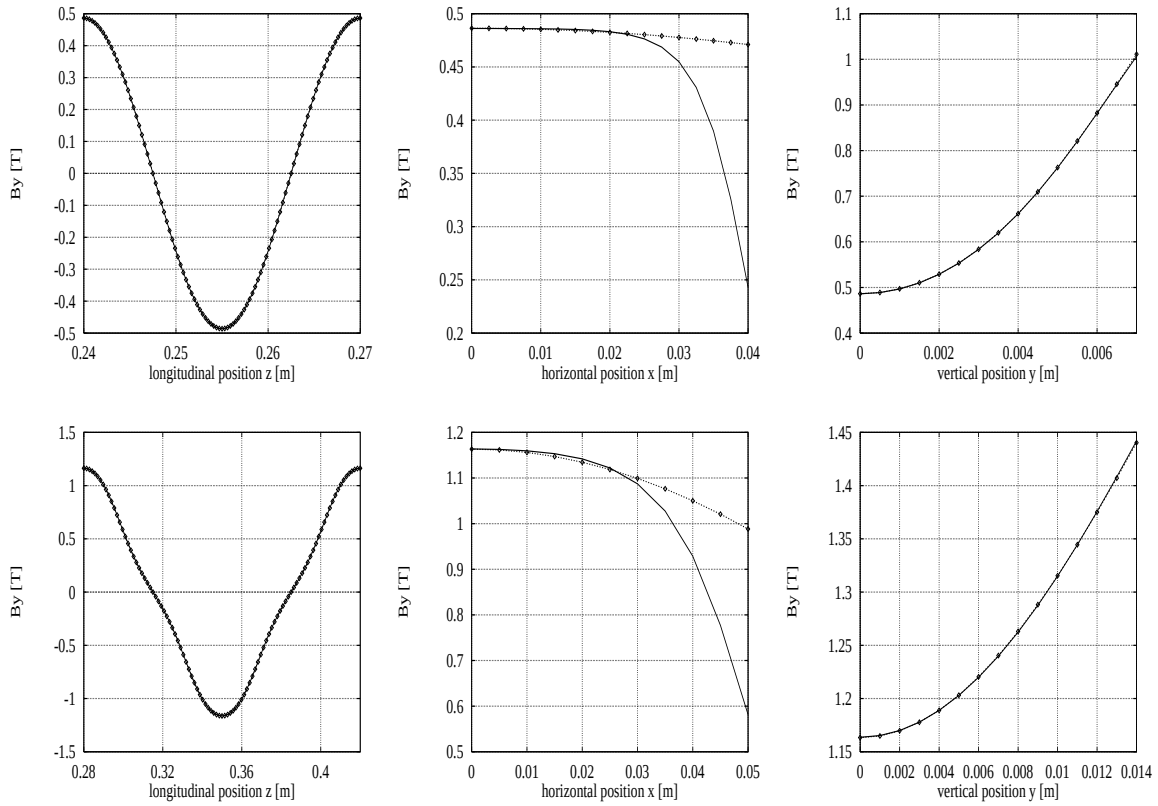

Figure 2.4: *Comparison of the vertical field computed by the current sheet model (solid line) and the series expansion (dashed line with diamonds) of the pure permanent magnet undulator (upper row) and the hybrid wiggler (lower row). The field is plotted versus the longitudinal (left), horizontal (middle) and vertical (right) position.*

2.5 Magnetic Field Errors in Wigglers and Undulators

Different sources of magnetic field errors exist in permanent magnet structures. They may be classified within the following groups:

- **Dimension errors** are those related to the geometrical dimensions of the permanent magnet blocks and the steel poles. An accuracy of better than 50μm is today achievable for overall dimensions of permanent magnet blocks of $\approx$ 10cm [ALS90]. Steel poles can be finished by grinding to better than 20μm.
  The pole shape of the steel pole has a strong influence on the magnetic field. Different pole shapes can be used to vary the characteristics of the wiggler fields.

- **Alignment errors** are due to the positioning of the different components of the device. The permanent magnet blocks and steel poles can be transversly or longitudinally shifted or rotated.

- **Magnetization errors** are caused by imperfections in the permanent magnet material. The direction of magnetization can be rotated with respect to the block surface or even vary within one block. Typical materials show variations of the magnetization axis of up to $\pm 2^{\circ}$ [SHH+90]. The field homogeneity of permanent magnet blocks can also be disturbed considerably. A sorting of permanent magnet blocks can minimize the effect on the magnetic field of the wiggler.

Numerical and analytical tools have been developed to treat these errors in the design phase of a wiggler. In the case of pure permanent magnet arrays one can include dimension and alignment errors in the current sheet model by distributing those errors over the magnet blocks. The analysis of hybrid devices is more complicated [SHH+90],[Hal86].

From our point of view, we are not really interested in the source of the magnetic field error but in its final effect. The resulting field errors may occur as a lack of periodicity, either by a longitudinal variation of position or dimension of the device components from one period to the other or in a variation of the peak fields. Another effect is the appearance of non-zero field integrals (see chapter 2.6), leading to a net steering of particles traveling through the wiggler. This steering can depend on the transversal positions of the particle entering the wiggler and on the gap of the device.

One aim of this work is to define limits for field errors. For this purpose one has to relate field measurements and quantities which define these limits to the field errors. One way to do this is to set limits on the multipole components of the field integrals. There are some difficulties related with this procedure: The overall field integral does not take into account large field errors at two positions in the device canceling each other over the whole length of the device. This can be overcome by measuring the evolution of the field integral over the device length. Field integrals are usually performed along straight lines through the wiggler fields. This does not take into account the undulating particle trajectory. We will treat this by modeling wigglers with the help of the current sheet model, whose overall field qualities are fitted to the measured values of the field integrals. In addition we use multipole expansions of the field integrals as a direct input in the beam dynamics analysis.

2.6 Multipole Expansion of Measured Field Integrals

One way to measure the overall effect of a longitudinally varying magnetic field is to evaluate the field integrals in the longitudinal direction:

$$\begin{aligned} \int_{-\infty}^{+\infty} B_x(x,y,z)\,\mathrm{d}z &= I_x(x,y) \\ \int_{-\infty}^{+\infty} B_y(x,y,z)\,\mathrm{d}z &= I_y(x,y) \\ \int_{-\infty}^{+\infty} B_z(x,y,z)\,\mathrm{d}z &= I_z(x,y) \quad . \end{aligned} \tag{2.15}$$

If the field integral $I_z(x,y) = 0$ for all values of x and y, the field properties of the three dimensional field are reduced to a two dimensional representation, which has to fulfill Maxwell's equations [EG54].

The two dimensional field integral may be expressed in a multipole series. This ensures the fulfillment of Maxwell's equations. The expansion is usually done in cylindrical coordinates, but for our purpose it is much more convenient to expand in cartesian coordinates. The general expansion may be written in the following form:

$$I_x - \mathrm{i}I_y = \sum_{n=0}^{\infty} (a_n + \mathrm{i}b_n)(x + \mathrm{i}y)^n \tag{2.16}$$

where the b_n refer to 'normal' multipoles and the a_n to 'skew' multipoles. From the theory of analytic functions it is known that this power series converges only in a certain radius r_0 around the origin of the expansion. For wigglers and undulators this radius is given by the shortest distance between the origin of the expansion and the magnet pole surface, as shown in figure 2.5. Magnetic fields outside the convergence radius but still inside the vacuum connected to it can be obtained by the method of analytic continuation; for this it is principally necessary to know the multipole coefficients up to infinite order.

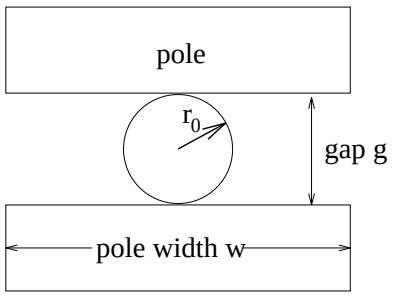

Figure 2.5: *Convergence radius of the multipole expansion inside a wiggler gap.*

From a pragmatic point of view one may neglect the non-convergence of the series in a region where the magnetic fields are of less importance such as inside the pole material, as long as the series describes the field inside the magnetic gap well enough within a certain transversal limit. This has to be proven empirically for each case, but it seems to work for simple geometries such as planar magnets.

The numerical derivation of multipole coefficients from field measurements is described in appendix A.

As an example the measured field integrals of the DORIS asymmetric wiggler (ASYH, see [Pfl92],[Pfl93a] and appendix C) are fitted with a multipole series. This wiggler was chosen due to the strong variation of its field integral with transversal offsets from the wiggler axis. The measured vertical field integral I_y is shown in figure 2.6. Because of the very large gradient in the outer regime, the analysis is restricted to an area of $x = \pm 25\text{mm}, y = \pm 12\text{mm}$.

The multipole series is truncated at the 4th order. Higher order multipole coefficients are smaller than the errors calculated below and do not increase the accuracy of the fit. In addition there exists a limit for the order of expansion n due to the number of measuring points N: $2n \leq N$. The multipole coefficients up to the 4th order are given in table 2.2.

The error of each coefficient is estimated by assuming that the contribution to the field integral due to every single multipole coefficient should exceed twice the rms[b]-error of the measurement $\chi_{meas.} = \pm 5 \cdot 10^{-5}\text{Tm}$. If only the vertical component of the field integral I_y has been measured, this gives for example for $n = 2$: $|I_y| = \text{Im}(a_2 + ib_2)(x + iy)^2 \geq 1.0 \cdot 10^{-4}\text{Tm}$. The error limits are calculated for the position $x = 20\text{mm}, y = 10\text{mm}$ and a_n respectively b_n is set to zero.

Table 2.2: *Multipole coefficients of the ASYH up to the 4th order*

order	skew component		normal component		
	a	error limit	b	error limit	
0	$1.42 \cdot 10^{-4}$	$1.0 \cdot 10^{-4}$	$-1.09 \cdot 10^{-5}$	$1.0 \cdot 10^{-4}$	Tm
1	$1.46 \cdot 10^{-2}$	$1.0 \cdot 10^{-2}$	$7.28 \cdot 10^{-3}$	$5.0 \cdot 10^{-3}$	T
2	$-4.60 \cdot 10^{-1}$	$2.5 \cdot 10^{-1}$	$-4.58 \cdot 10^{-1}$	$3.3 \cdot 10^{-1}$	T/m
3	$-1.06 \cdot 10^{1}$	$9.0 \cdot 10^{0}$	$3.92 \cdot 10^{0}$	$5.0 \cdot 10^{1}$	T/m^2
4	$9.28 \cdot 10^{2}$	$4.2 \cdot 10^{2}$	$5.43 \cdot 10^{3}$	$1.4 \cdot 10^{3}$	T/m^3

The resulting field integral is shown in figure 2.7 together with the transverse distribution of the absolute error of the fit with respect to the measuring points. The rms-error of the field description

$$\chi_{fit} = \sqrt{\frac{1}{N}\sum_{i=1}^{N}(I_{fit}(x_i, y_i) - I_{meas.}(x_i, y_i))^2}$$

is $\chi_{fit} = 3.08 \cdot 10^{-4}\text{Tm}$, if the whole rectangular area of $x = \pm 25\text{mm}$, $y = \pm 12\text{mm}$ is taken into account. This error reduces to $\chi_{fit} = 1.0 \cdot 10^{-4}\text{Tm}$ if only the points within a radius of 25mm are taken into account, i.e neglecting the corners of the rectangular area. The error has to be compared with the measurement error $\chi_{meas.} = 0.5 \cdot 10^{-4}\text{Tm}$. The chosen multipole representation fulfills Maxwell's equations by definition and the rms-error χ_{fit} is of the same order as $\chi_{meas.}$. Thus it is a sufficient description of the measured field integral within the radius indicated in the figures.

[b] rms = root mean square

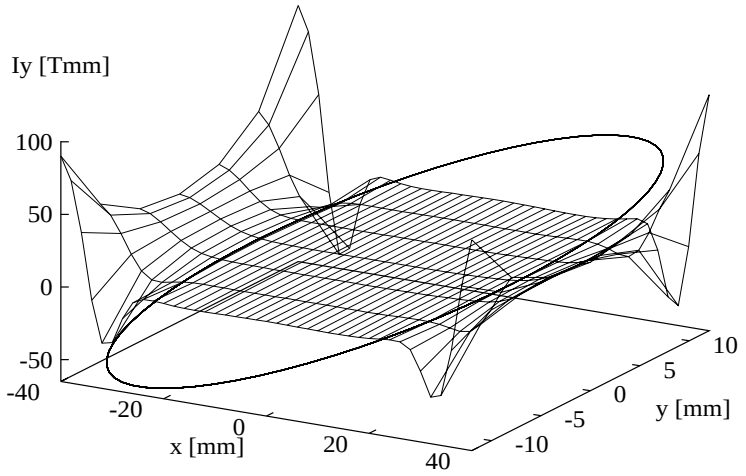

Figure 2.6: *Measured field integral I_y of the asymmetric wiggler ASYH versus the horizontal and vertical position with respect to the wiggler axis (data from [Pfla]). The circle denotes the chosen convergence radius r_0.*

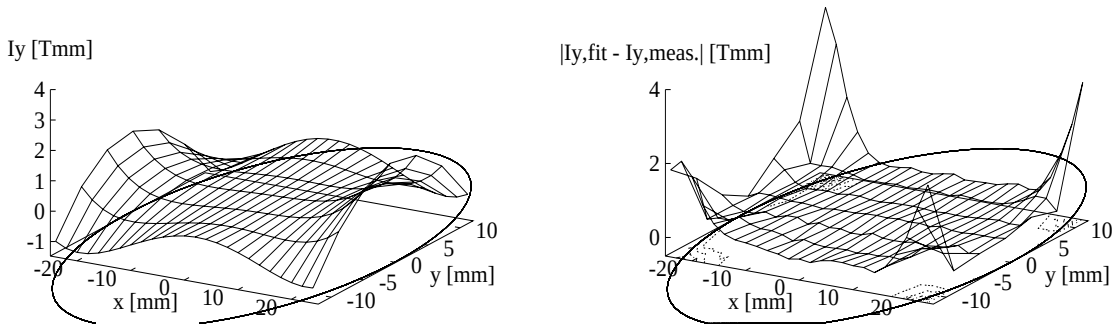

Figure 2.7: *Multipole fit of the field integral I_y of the asymmetric wiggler ASYH (left). The absolute error, i.e $|I_{y,fit} - I_{y,meas.}|$ is plotted in the right figure. Note the reduced horizontal scale with respect to figure 2.6.*

The field integral (2.15) is called the first field integral. In terms of particle motion the first field integral corresponds to a change in the direction of motion under the influence of the field. The so-called second field integral is a measure for a change of the transverse particle coordinate. The definition of the second field integral is:

$$\begin{aligned} \int_{-\infty}^{+\infty} I_x(x,y,z)\,\mathrm{d}z &= I_x^{(2)}(x,y) \\ \int_{-\infty}^{+\infty} I_y(x,y,z)\,\mathrm{d}z &= I_y^{(2)}(x,y) \\ \int_{-\infty}^{+\infty} I_z(x,y,z)\,\mathrm{d}z &= I_z^{(2)}(x,y) \end{aligned} \tag{2.17}$$

where $I(x,y,z) = \int_{-\infty}^{z} B(x,y,z')\,\mathrm{d}z'$.
It is possible to perform the same multipole analysis described above for the second field integral, if $I_z^{(2)}(x,y) = 0$ for all values of x and y.

2.7 Modeling of Field Errors with the Current Sheet Method

The field errors of wiggler magnets can be modeled by the current sheet method by assuming appropriate block dimensions and positions which lead to field integrals corresponding to the measured ones. The ASYH wiggler, which was introduced in the previous chapter is again used as an example. It is modeled by a series of permanent magnet blocks with alternating remanent fields and different field strengths and block dimensions. This describes both the asymmetry of the field amplitudes along the longitudinal axis as well as the multipole components of the field integral. Figure 2.8 shows the longitudinal behavior of the field of the asymmetric wiggler and the first field integral of the vertical field versus the horizontal position. The multipole components are $b_2 = 20\mathrm{T/m}$ and $b_4 = 18000\mathrm{T/m}^3$. This is approximately the field integral as it was measured before a correction with steel shims on the poles. The values derived after the correction are given in table 2.2. The influence of this wiggler on the beam dynamics of DORIS is discussed in chapters 4.3.3 and 5.7.

Another application of this method is the simulation of periodicity errors. These are produced by varying the remanent field strength of the individual blocks and their longitudinal positioning and dimensions. Figure 2.9 gives an example of a field obtained with this method. The field is compared with the perfect periodic one. The maximum field amplitude error is $\approx 15\%$, while the period length varies within a range of $\pm 4\%$ (defined by the distance between neighboring field maxima). These values are far above the accuracy obtainable nowadays, which is $< 1\%$ for the amplitude error and $< 0.1\%$ for the period length variation. This example should just illustrate the method.

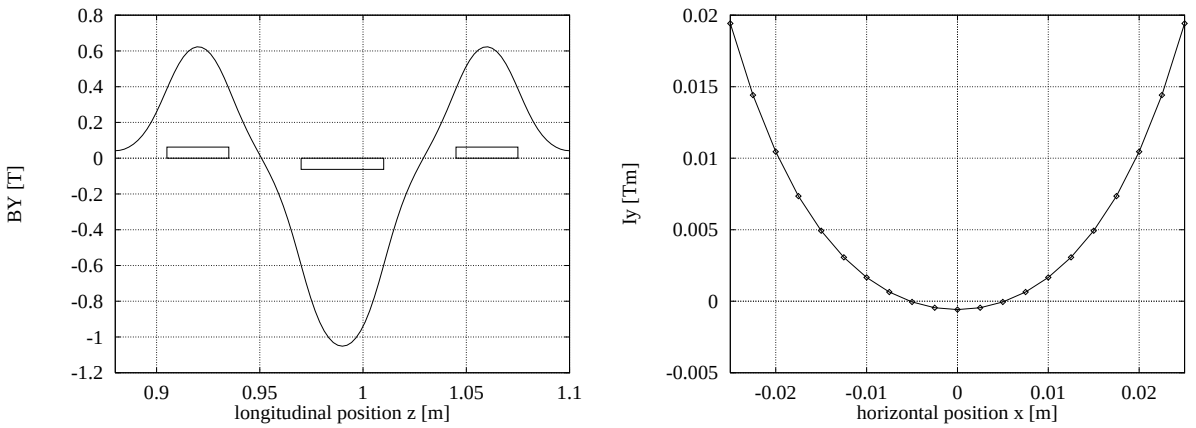

Figure 2.8: *Vertical magnetic field properties of the asymmetric wiggler model.*
Left: *Vertical field amplitude versus longitudinal position, showing one period of the wiggler.*
Right: *Vertical field integral* $I_y(x) = \int_{-\infty}^{+\infty} B_y(x)dz$ *versus horizontal position.*

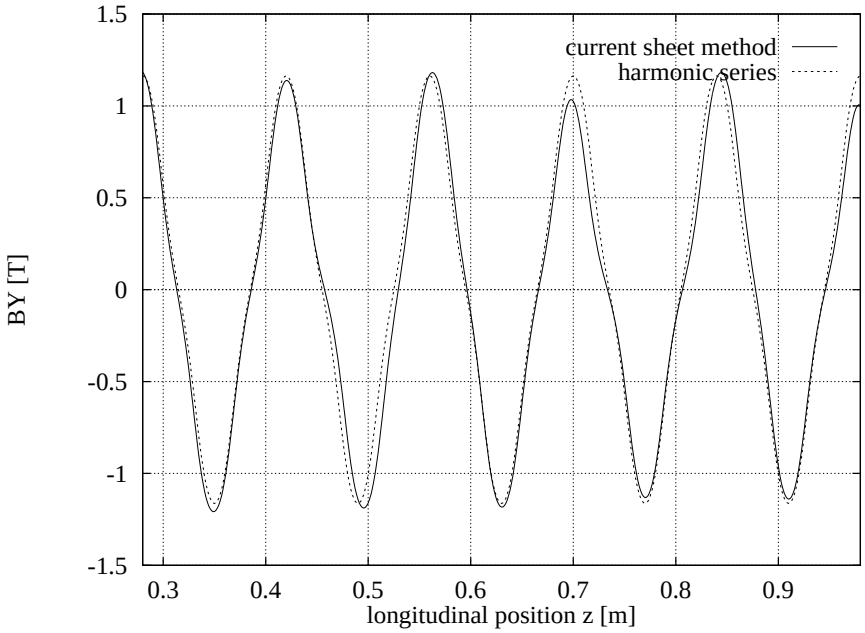

Figure 2.9: *Periodicity error produced by a variation of the longitudinal block dimensions, longitudinal block positions and different remanent fields of each block. Displayed is the vertical magnetic field of five wiggler periods calculated with the series expansion (dashed line) and the current sheet model including the errors described above (solid line).*

3 Single Particle Motion in a Storage Ring with Wigglers

The basic concepts to describe the motion of charged particles in storage rings will be reviewed in this chapter. A six dimensional Hamiltonian formalism and the results which can be obtained by perturbation theory are discussed. Introducing wiggler fields, the equations of motions for particles traveling through a wiggler are derived and treated within the perturbation theory. The numerical analysis of particle dynamics will be introduced and the different treatments of wiggler fields in tracking codes are explained and compared.

3.1 The Equations of Motion in a Storage Ring

The equations of motion will be derived using the Hamiltonian formalism. Given a Hamilton function $H(q_\mu, p_\mu, t)$ of the generalized coordinates q_μ[a], their canonical momenta p_μ and the independent variable t the equations of motion are:

$$\frac{dq_\mu}{dt} = \frac{\partial H}{\partial p_\mu} \qquad \frac{dp_\mu}{dt} = -\frac{\partial H}{\partial q_\mu} \quad . \tag{3.1}$$

The general form of the Hamiltonian for the motion of a particle with rest mass m_0 and charge e in electromagnetic fields described by their scalar and vector potentials ϕ and $\vec{A}$ is [Gol85]:

$$H(\vec{q}, \vec{p}, t) = e\phi(t) + \mathrm{c}\sqrt{(\vec{p} - \mathrm{e}\vec{A}(t))^2 + m_0^2 c^2} \quad . \tag{3.2}$$

By a series of canonical transformations (see for example [Bel87],[Rip85]) the coordinate system is changed into the 'natural' coordinate system [CS58] which describes the particle motion with respect to a design orbit through the accelerator components. The new variables are obtained through the generating function

$$F(p_x, p_y, p_z, \tilde{x}, \tilde{y}, s) = \vec{p}(\vec{r}_0(s) + \tilde{x}\vec{e}_{\tilde{x}} + \tilde{y}\vec{e}_{\tilde{y}}) \tag{3.3}$$

where r_0 is the design orbit and the tilde $\tilde{}$ marks the new variables. The accompanying coordinate system is derived from the design orbit via the Serret-Frenet formulae:

$$\vec{e}_x' = \frac{1}{\rho_x(s)}\vec{e}_s$$

[a] μ indicates the different degrees of freedom of the system, i.e. it stands for x, y, z in a cartesian coordinate system, for example.

$$\begin{aligned}
\vec{e}_y' &= \frac{1}{\rho_y(s)}\vec{e}_s \\
\vec{e}_s' &= -\frac{1}{\rho_x(s)}\vec{e}_x - \frac{1}{\rho_y(s)}\vec{e}_y \\
\vec{e}_s &= \vec{r}_0' \qquad (3.4)
\end{aligned}$$

where the prime $'$ means a differentiation with respect to s and $\rho_{x,y}$ is the local radius of curvature of the design orbit. The $\tilde{}$ has been dropped, this will be done in the following after each transformation.

This transformation changes from a global cartesian coordinates into an accompanying local coordinate system. This procedure will be helpful for determining the Hamiltonian for wiggler motion. The vector potential has to be given in the new coordinate system, this is done by exchanging $\vec{p}$ with $\vec{A}$ in (3.3) and solving the equations which define the transformation (see [CS58]).

Another canonical transformation changes the independent variable to s, the distance along the design path. To describe the longitudinal motion, two new, small variables are introduced:

$$\begin{aligned}
\sigma &= s - ct \quad \text{the longitudinal distance to a particle traveling with } c \\
p_\sigma &= \frac{p - p_0}{p_0} \quad \text{the relative impulse deviation of the particle}
\end{aligned}$$

where p is the particle impulse and p_0 the impulse of the reference particle. The new coordinate system is illustrated in figure 3.1.

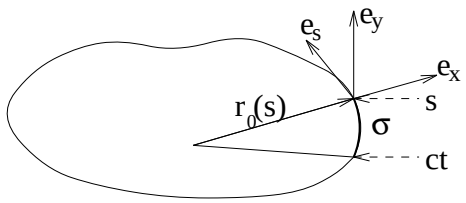

Figure 3.1: *Orthogonal coordinate system for the motion of a charged particle in a storage ring. The 'dreibein' accompanies the reference particle on the design orbit.*

The new Hamiltonian becomes [Rip85],[BHRW94]:

$$\begin{aligned}
H(\vec{q},\vec{p},s) = (1+p_\sigma)\left(1 - \left(1 + \frac{1}{\rho_x(s)}x + \frac{1}{\rho_y(s)}y\right)\right. \\
\left.\cdot\sqrt{1 - \frac{(p_x - \frac{e}{p_0}A_x(s))^2 + (p_y - \frac{e}{p_0}A_y(s))^2}{(1+p_\sigma)^2}}\right) - \left(1 + \frac{1}{\rho_x(s)}x + \frac{1}{\rho_y(s)}y\right)\frac{e}{p_0}A_s(s) \quad .
\end{aligned}$$

An expansion up to third order in the canonical variables yields:

$$\begin{aligned}
H(\vec{q},\vec{p},s) = -\left(\frac{1}{\rho_x(s)}x + \frac{1}{\rho_y(s)}y\right)p_\sigma + \frac{1}{2}\left(1 + \frac{1}{\rho_x(s)}x + \frac{1}{\rho_y(s)}y - p_\sigma\right) \\
\cdot\left(\left(p_x - \frac{e}{p_0}A_x(s)\right)^2 + \left(p_y - \frac{e}{p_0}A_y(s)\right)^2\right) - \left(1 + \frac{1}{\rho_x(s)}x + \frac{1}{\rho_y(s)}y\right)\frac{e}{p_0}A_s(s) \quad . \qquad (3.5)
\end{aligned}$$

A radiation term H_{rad} has to be added if one wants to take account for the average radiation loss of electrons in a magnetic guide field:

$$H_{rad} = C\left((\frac{1}{\rho_x})^2 + (\frac{1}{\rho_y})^2\right)\sigma \tag{3.6}$$

with $C = \frac{2}{3}r_e\gamma^3$ where r_e is the classical electron radius [San70].
This Hamiltonian describes the 6-dimensional motion of an electron in the electromagnetic fields of an accelerator. The physical meaning of the canonical variables is:

$$\begin{aligned} x = x \qquad & p_x = x' + \frac{e}{p_0}A_x \\ y = y \qquad & p_y = y' + \frac{e}{p_0}A_y \\ \sigma = s - ct \qquad & p_\sigma = \frac{p - p_0}{p_0} \quad . \end{aligned}$$

For off momentum particles ($p_\sigma \neq 0$) the transversal and longitudinal motions are coupled via:

$$H(\vec{q}, \vec{p}, s) = -(\frac{1}{\rho_x(s)}x + \frac{1}{\rho_y(s)}y)p_\sigma \quad .$$

This term can be canceled by introducing the dispersion function

$$\vec{D}(s) = (D_1(s), D_2(s), D_3(s), D_4(s))$$

which defines a new reference orbit for particles with $p_\sigma \neq 0$. The corresponding generating function is [BMRW86]:

$$\begin{aligned} F(x, y, \sigma, \tilde{p_x}, \tilde{p_y}, \tilde{p_\sigma}, s) \quad = \quad & \tilde{p_x}(x - \tilde{p_\sigma}D_1) + x\tilde{p_\sigma}D_2 + \tilde{p_y}(x - \tilde{p_\sigma}D_3) \\ & + y\tilde{p_\sigma}D_4 - \frac{1}{2}(D_1D_2 + D_3D_4)\tilde{p_\sigma}^2 + \tilde{p_\sigma}\sigma \quad . \end{aligned} \tag{3.7}$$

Thus the new coordinates are:

$$\begin{aligned} \tilde{x} &= x - D_1p_\sigma \\ \tilde{p_x} &= p_x - D_2p_\sigma \\ \tilde{y} &= y - D_3p_\sigma \\ \tilde{p_y} &= p_y - D_4p_\sigma \\ \tilde{\sigma} &= \sigma + \tilde{x}D_2 - \tilde{p_x}D_1 + \tilde{y}D_4 - \tilde{p_y}D_3 \\ \tilde{p_\sigma} &= p_\sigma \quad . \end{aligned} \tag{3.8}$$

The dispersion is defined by the periodic solution of the canonical equations of the new Hamiltonian with $x = p_x = y = p_y \equiv 0$.

We will now derive the Hamiltonian in the presence of the accelerator components quadrupoles, dipoles and cavities, which are responsible for the linear focusing forces. The magnetic vector potentials of these devices in the accelerator coordinate system (3.4) are:

quadrupole: $A_{x,y}(s) = 0, \quad \frac{e}{p_0} A_s(s) = \frac{1}{2} g(s)(y^2 - x^2)$
with $g = \frac{e}{p_0} \frac{\partial B_y}{\partial x}$

dipole: $A_{x,y}(s) = 0, \quad \frac{e}{p_0} A_s(s) = \frac{1}{\rho_x(s)} x + \frac{1}{\rho_y(s)} y$
with $\frac{1}{\rho_{x,y}} = \frac{e}{p_0} B_{y,x}$

cavity: $A_{x,y}(s) = 0, \quad \frac{e}{p_0} A_s(s) = \frac{L}{2\pi h} \frac{eV(s)}{E_0} \cos(\frac{2\pi h}{L}\sigma + \varphi)$
with L =circumference, h =harmonic number and
$V(s)$=amplitude of cavity voltage .

After changing to the dispersion coordinate system the Hamiltonian becomes [BHRW94]

$$\begin{aligned} H(\vec{q}, \vec{p}, s) &= \frac{1}{2}(p_x^2 + p_y^2) + \frac{1}{2}\left(\left((\frac{1}{\rho_x(s)})^2 + g(s)\right) x^2 + \left((\frac{1}{\rho_y(s)})^2 - g(s)\right) y^2\right) \\ &\quad - \frac{1}{2}\left(\frac{1}{\rho_x(s)} D_1 + \frac{1}{\rho_y(s)} D_3\right) p_\sigma^2 - \frac{2\pi h}{L} \frac{eV(s)}{E_0} \frac{1}{2} \sigma^2 \cos\varphi + \mathcal{O}(3) \end{aligned} \quad (3.9)$$

where we expanded the vector potential of the cavity and assumed that there is no dispersion in the cavity. A dispersion in the cavity would lead to coupling terms between the longitudinal and transversal motion, as described in [BMRW86],[BHRW94], [PW76]. Up to now we are only interested in the uncoupled motion and we will consider dispersion in nonlinear fields as a source of coupling later. The $\mathcal{O}(3)$ term in (3.9) contains higher order coupling terms which lead for example to the generation of chromaticity.

The equations of motion can then be written in the following form:

$$\frac{d}{ds} \begin{pmatrix} \mu \\ p_\mu \end{pmatrix} = \mathbf{A}_\mu \cdot \begin{pmatrix} \mu \\ p_\mu \end{pmatrix}^b \quad .$$

These equations are linear and homogeneous, thus it is possible to write the solution in a transfer matrix form

$$\vec{\mu}(s) = \mathbf{M}_\mu(s, s_0) \cdot \vec{\mu}(s_0)$$

where the matrix $\mathbf{M}$ can be represented by the 'Twiss' parameters α_μ, β_μ, γ_μ (see [WR88], [RS94],[CS58]). In the linear, uncoupled case the revolution matrix $\mathbf{M}$ becomes:

$$\mathbf{M}_\mu(s + L, s) = \begin{pmatrix} \cos(2\pi Q_\mu) + \alpha_\mu \sin(2\pi Q_\mu) & \beta_\mu \sin(2\pi Q_\mu) \\ -\gamma_\mu \sin(2\pi Q_\mu) & \cos(2\pi Q_\mu) + \alpha_\mu \sin(2\pi Q_\mu) \end{pmatrix} \quad (3.10)$$

where the tune Q_μ will be introduced later. Transfer matrices for the linear elements are given for example in [RS94].

It is now possible to establish action-angle variables I_μ, ϕ_μ via the general transformation [Gol85] defined by the generating function:

$$F_1 = -\frac{\mu^2}{2\beta}(\tan(\phi_\mu + \phi_{0,\mu}) - \frac{\beta'}{2})$$

[b] μ stands for the variables x, y and σ and will be used in the following if the corresponding equations are similar.

leading to the equations of motion

$$\begin{aligned} \mu(s) &= \sqrt{2\beta_\mu(s) I_\mu}\cos(\phi_\mu(s)+\phi_{0,\mu}) \\ p_\mu(s) &= \sqrt{\frac{2I_\mu}{\beta_\mu(s)}}\left(\sin(\phi_\mu(s)+\phi_{0,\mu})+\alpha_\mu(s)\cos(\phi_\mu(s)+\phi_{0,\mu})\right) \end{aligned} \tag{3.11}$$

and the corresponding Hamiltonian:

$$H = \frac{I_x}{\beta_x} + \frac{I_y}{\beta_y} + \frac{I_\sigma}{\beta_\sigma} \quad .$$

The physical meaning of the action-angle variables will be discussed briefly. The angle $\phi(s)$ represents the phase advance of the quasi harmonic oscillation described in (3.11), and thus the quantity:

$$Q_\mu = \nu_\mu/2\pi = \frac{1}{2\pi}(\phi(s+L)-\phi(s)) = \frac{1}{2\pi}\int_s^{s+L}\frac{1}{\beta_\mu}ds \tag{3.12}$$

is the tune, i.e. the number of oscillations per revolution.

At constant s, a particle describes from turn to turn a closed curve in phase space, where the phase advance is given by (3.12) and the area of the enclosed phase space is

$$\text{area} = 2\pi\, I = \pi\varepsilon \tag{3.13}$$

introducing the emittance ε.

We have derived the linear equations of motion in some detail to introduce important quantities such as the β-function, the tune and the emittance. The above treatment describes the motion in the 6-dimensional phase space within the same framework, i.e. the longitudinal motion can also be described with Twiss parameters etc.. This allows the investigation of the nonlinear 6-dimensional motion with the help of standard perturbation theory [Gui78],[BMRW86].

3.2 Perturbation Theory

In this chapter we will briefly discuss the modifications which have to be done if the Hamiltonian contains also a small, nonlinear perturbation part H_1, thus

$$H = H_0 + H_1 \quad .$$

It is often possible to write the perturbation part of the Hamiltonian as a power series in the canonical variables:

$$H_1(\vec{q},\vec{p},s) = \sum_{\nu_1,\nu_2,\nu_3,\nu_4,\nu_5,\nu_6} A_{\nu_1\nu_2\nu_3\nu_4\nu_5\nu_6}(s)\, x^{\nu_1}\, p_x^{\nu_2}\, y^{\nu_3}\, p_y^{\nu_4}\, \sigma^{\nu_5}\, p_\sigma^{\nu_6} \quad . \tag{3.14}$$

The Hamiltonian will now be transformed into the action-angle variables of the unperturbed problem (3.11). A solution of the equations of motion is found if I_μ, $\phi_{0,\mu}$ are allowed to vary with s (variation of constants [Hag57],[Sch57]).

After introducing action angle variables the Hamiltonian consists of a periodic and a non periodic part in s. The periodic part can be expanded in a Fourier series, and the perturbation Hamiltonian becomes:

$$\begin{aligned} H_1(\vec{I},\vec{\phi_0},s) = & \sum_{\nu_1,\nu_2,\nu_3,\nu_4,\nu_5,\nu_6,n} a_{\nu_1\nu_2\nu_3\nu_4\nu_5\nu_6 n}\, 2I_x^{(\nu_1+\nu_2)/2}\, 2I_y^{(\nu_3+\nu_4)/2}\, 2I_\sigma^{(\nu_5+\nu_6)/2} \\ & \cdot\cos\Big((\nu_1-\nu_2)\phi_{0,x} \pm (\nu_3-\nu_4)\phi_{0,y} \pm (\nu_5-\nu_6)\phi_{0,\sigma} \\ & + \Big((\nu_1-\nu_2)Q_x \pm (\nu_3-\nu_4)Q_y \pm (\nu_5-\nu_6)Q_s - n\Big)\, s\,\frac{2\pi}{L} + \alpha\Big) \end{aligned} \tag{3.15}$$

where the Fourier coefficients $a_{\nu_1\nu_2\nu_3\nu_4\nu_5\nu_6 n}$ are:

$$\begin{aligned} a_{\nu_1\nu_2\nu_3\nu_4\nu_5\nu_6 n} = & \frac{1}{L}\int_s^{s+L} ds A_{\nu_1\nu_2\nu_3\nu_4\nu_5\nu_6}(s)\, \beta_x^{(\nu_1-\nu_2)/2}\, \beta_y^{(\nu_3-\nu_4)/2}\, \beta_\sigma^{(\nu_5-\nu_6)/2} \\ & \cdot\cos\Big((\nu_1-\nu_2)\phi_x \pm (\nu_3-\nu_4)\phi_y \pm (\nu_5-\nu_6)\phi_\sigma \\ & - \Big((\nu_1-\nu_2)Q_x \pm (\nu_3-\nu_4)Q_y \pm (\nu_5-\nu_6)Q_s - n\Big) s\frac{2\pi}{L}\Big) \quad . \end{aligned} \tag{3.16}$$

The perturbed Hamiltonian has an explicit dependence on s. As long as the perturbations (the Fourier coefficients) are small, only terms which vary slowly in s can make a significant contribution to the change of the variables I, ϕ_0. Thus, only terms where the oscillation frequency $((\nu_1-\nu_2)Q_x \pm (\nu_3-\nu_4)Q_y \pm (\nu_5-\nu_6)Q_s - n)\, s\frac{2\pi}{L}$ is small contribute. This is the case if the tunes satisfy the resonance condition:

$$(\nu_1-\nu_2)Q_x \pm (\nu_3-\nu_4)Q_y \pm (\nu_5-\nu_6)Q_s = n$$

or

$$n_xQ_x + n_yQ_y + n_sQ_s = n \quad \text{with } n_x, n_y, n_s, n = \text{integer} \quad . \tag{3.17}$$

The amount of change of the variables of motion is given by the Fourier coefficients (3.16). They are called therefore excitation coefficients and give a measure for the strength of a resonance.

3.3 The Hamiltonian of a Wiggler

We will now derive the Hamiltonian for the motion of a particle through a wiggler field. The base of the calculation will be the vector potential $\vec{A}$ given in equation (2.10). We will stay in the cartesian coordinate system with the wiggler axis being the origin of the (x,y)-plane. The distance along the orbit s will be counted along the longitudinal axis z of the wiggler. This means, that up to now there will be no curvature of the orbit in our treatment, i.e. $\frac{1}{\rho_\mu} = 0$. Therefore the Hamiltonian simplifies to:

$$H = \frac{1}{2}\left((p_x - \frac{e}{p_0}A_x)^2 + (p_y - \frac{e}{p_0}A_y)^2\right) \tag{3.18}$$

which leads together with the canonical equations (3.1) to the equations of motion:

$$\begin{aligned} x'' &= -x'\frac{\partial A_x}{\partial x} - y'\frac{\partial A_y}{\partial x} - \frac{e}{p_0}\frac{\partial A_x}{\partial z} \\ y'' &= -x'\frac{\partial A_x}{\partial y} - y'\frac{\partial A_y}{\partial y} - \frac{e}{p_0}\frac{\partial A_y}{\partial z} \quad . \end{aligned} \tag{3.19}$$

The equations of motion describe a sinusoidal varying electron path within the wiggler and a kind of focusing, driven by the non-parallel passage of the electron through the longitudinal fields of the wiggler (edge focusing).

To get a more simple description of the electron motion within a wiggler, the Hamiltonian (3.18) is averaged over one wiggler period. This procedure is justified as long as the position and angle of the particle do not vary to strong within one period, which is fulfilled as long as $\beta/\lambda_0 \gg 1$. The averaged Hamiltonian becomes, after expanding the sinh, cosh-terms up to 4th order:

$$\begin{aligned} < H > &= \frac{1}{2}(p_x^2 + p_y^2) \\ &\quad + \frac{1}{\rho^2 k^2}\left(\frac{1}{4}k_x^2 x^2 + \frac{1}{4}k_y^2 y^2 + \frac{1}{12}k_x^4 x^4 + \frac{1}{12}k_y^4 y^4 + \frac{1}{4}k_x^2 k^2 x^2 y^2\right) \end{aligned} \tag{3.20}$$

with $\frac{1}{\rho} = \frac{eB_1}{p_0}$.
The averaged Hamiltonian $< H >$ has no z-dependence. It describes a linear focusing with a corresponding quadrupole strength

$$g_x = \frac{1}{2}\frac{k_x^2}{\rho^2 k^2} \qquad , \qquad g_y = \frac{1}{2}\frac{k_y^2}{\rho^2 k^2} \tag{3.21}$$

and includes 4th order nonlinear terms with a corresponding pseudo-octupole strength

$$o_x = \frac{1}{3}\frac{k_x^4}{\rho^2 k^2} \qquad , \qquad o_y = \frac{1}{3}\frac{k_y^4}{\rho^2 k^2} \; . \tag{3.22}$$

To obtain some more features of the wiggler motion, the sinusoidal trajectory of equation (3.19) is reinterpreted as the closed orbit x_e, y_e within the wiggler with respect to the initial transversal position x_i, y_i

$$\begin{aligned} x_e' &= -\frac{1}{\rho k}\cosh(k_x x_i)\cosh(k_y y_i)\sin(kz) \\ y_e' &= \frac{k_x}{k_y \rho k}\sinh(k_x x_i)\sinh(k_y y_i)\sin(kz) \end{aligned} \tag{3.23}$$

$$\begin{aligned} x_e &= \frac{1}{\rho k^2}\cosh(k_x x_i)\cosh(k_y y_i)\cos(kz) \\ y_e &= -\frac{k_x}{k_y \rho k^2}\sinh(k_x x_i)\sinh(k_y y_i)\cos(kz) \end{aligned} \tag{3.24}$$

which gives the local radius of curvature of the orbit:

$$\frac{1}{\rho_x(z)} = k^2 x_e \qquad , \qquad \frac{1}{\rho_y(z)} = k^2 y_e \; . \tag{3.25}$$

These definitions allow to calculate the average energy loss within a wiggler from the H_{rad} term:

$$\frac{dp_\sigma}{ds} = -\frac{\partial H_{rad}}{\partial \sigma} = -C\left(\left(\frac{1}{\rho_x}\right)^2 + \left(\frac{1}{\rho_y}\right)^2\right)$$

which becomes by inserting equation (3.25), averaging over one period and expanding the hyperbolic functions:

$$\frac{dp_\sigma}{ds} = -C\frac{1}{2\rho^2}\left(1 + k_x^2x^2 + k_y^2y^2 + \frac{1}{3}(k_x^4x^4 + k_y^4y^4) + k_x^2k^2x^2y^2\right) \quad . \tag{3.26}$$

The dispersion generated by a wiggler is also derived. The local radius of curvature (3.25) and the defining equations of the dispersion lead to the dispersion generated by a wiggler:

$$\begin{aligned} D_1(s) &= \int D_2(s)ds = x_e \\ D_2(s) &= \int \frac{1}{\rho_x(s)}ds = x_e' \\ D_3(s) &= \int D_4(s)ds = y_e \\ D_4(s) &= \int \frac{1}{\rho_y(s)}ds = y_e' \quad . \end{aligned} \tag{3.27}$$

The dispersion vanishes within one period.

It should be mentioned, that one can derive a Hamiltonian description also by transforming into a coordinate system following the closed orbit within a wiggler. This was done originally by [Smi86]. The obtained Hamiltonian contains an additional term oscillating with the wiggler period:

$$H_{osc.} = -\frac{1}{2k\rho}\sin(ks)\left(p_x(k_x^2x^2 + k_y^2y^2) - 2p_yk_x^2xy\right) \tag{3.28}$$

which is kept during the averaging procedure because of the third-order terms which will drive third-order resonances. We averaged this term, because it is of minor influence on the motion and the explicit s-dependence makes the following analysis more complicated. The different equations of motion will be compared numerically in chapter 3.6.

The Hamiltonian (3.20) will now be analyzed by perturbation theory. To do this, we split the Hamiltonian into a linear and a non-linear part and assume, that the linear terms (i.e. focusing) are treated within the unperturbed Hamiltonian. After introducing dispersion coordinates (3.8) in the Hamiltonian, it can be written as a power series in these new coordinates with the corresponding coefficients displayed in table 3.1 together with the excited resonances (see (3.14)).

A wiggler excites therefore 4th-order synchro-betatron resonances. In most of the realistic cases k_x is small and there is only spurious dispersion in the straight sections which contain wigglers. So most of the synchro-betatron resonances should not play an important role for the particle dynamics. Nevertheless, we observed the excitation of synchro-betatron resonances by wigglers in DORIS (see chapter 5 and [Dec94a]).

Table 3.1: *Coefficients of the power series of the Hamiltonian (3.20) together with the excited resonances*

ν_1	ν_2	ν_3	ν_4	ν_5	ν_6	$A_{\nu_1\nu_2\nu_3\nu_4\nu_5\nu_6}$	excited resonance $n_xQ_x + n_yQ_y + n_sQ_s$		
							n_x	n_y	n_s
4	0	0	0	0	0	k_x^4	4	0	0
0	0	4	0	0	0	k_y^4	0	4	0
2	0	± 2	0	0	0	$k_x^2k^2$	2	± 2	0
3	0	0	0	0	± 1	$\frac{4}{3}k_x^4D_1$	3	0	± 1
2	0	0	0	0	± 2	$2k_x^4D_1^2$	2	0	± 2
2	0	0	0	0	± 2	$k^2k_x^2D_3^2$	2	0	± 2
1	0	0	0	0	± 3	$\frac{4}{3}k_x^4D_1^3$	1	0	± 3
1	0	0	0	0	± 3	$2k^2k_x^2D_1D_3^2$	1	0	± 3
0	0	3	0	0	± 1	$\frac{4}{3}k_y^4D_3$	0	3	± 1
0	0	2	0	0	± 2	$2k_y^4D_3^2$	0	2	± 2
0	0	2	0	0	± 2	$k^2k_x^2D_1^2$	0	2	± 2
0	0	1	0	0	± 3	$\frac{4}{3}k_y^4D_3^3$	0	1	± 3
0	0	1	0	0	± 3	$2k^2k_x^2D_1^2D_3$	0	1	± 3
2	0	± 1	0	0	± 1	$2k^2k_x^2D_3$	2	± 1	± 1
1	0	± 2	0	0	± 1	$2k^2k_x^2D_1$	1	± 2	± 1
1	0	± 1	0	0	± 2	$4k^2k_x^2D_1D_3$	1	± 1	± 2

3.4 Numerical Analysis of Particle Dynamics

Due to the fact that the nonlinear systems, which have to be investigated during the analysis of particle dynamics in accelerators is very complicated, a numerical treatment is necessary. We have derived the base for such a treatment in the previous chapters. The concept will be to integrate the equations of motion piecewise through the accelerator components. The transformation matrix $\mathbf{M}$ for the canonical variables μ, p_μ [c] from a point s_1 to s_2 through the uncoupled, linear part of the accelerator is for one plane:

$$\begin{pmatrix} \sqrt{\frac{\beta_2}{\beta_1}}(\cos(\Delta\phi)+\alpha_1\sin(\Delta\phi)) & \sqrt{\beta_2\beta_1}\sin(\Delta\phi) \\ \frac{1}{\sqrt{\beta_2\beta_1}}((\alpha_1-\alpha_2)\cos(\Delta\phi)-(1+\alpha_1\alpha_2)\sin(\Delta\phi)) & \sqrt{\frac{\beta_1}{\beta_2}}(\cos(\Delta\phi)-\alpha_2\sin(\Delta\phi)) \end{pmatrix} \tag{3.29}$$

where $\Delta\phi = \phi_2 - \phi_1$ is the phase advance between the two points. The change due to nonlinear fields can be approximated through a nonlinear kick acting only on the canonical momenta. This kick is derived by integrating the equation of motion over the length of the considered element. The approximation is valid as long as the nonlinear field and the coordinates do not change over the integration step size. The transfer function for one wiggler period described by (3.20) becomes:

$$\begin{pmatrix} x \\ p_x \\ y \\ p_y \end{pmatrix}_{s+\lambda} = \begin{pmatrix} x \\ p_x \\ y \\ p_y \end{pmatrix}_s + \frac{1}{4\rho^2k^2} \begin{pmatrix} 0 \\ -(\frac{4}{3}k_x^4x^3+2k_x^2k^2xy^2)\lambda \\ 0 \\ -(\frac{4}{3}k_y^4y^3+2k_x^2k^2x^2y)\lambda \end{pmatrix}_s \tag{3.30}$$

It is of course possible to include every other description of the motion within a wiggler in (3.30). Eventually the equations of motion have to be integrated by an appropriate integrator.

For completeness the transfer function for a sextupole with $\frac{e}{p_0}A_s = \frac{n}{6}(x^3-3xz^2)$ is:

$$\begin{pmatrix} x \\ p_x \\ y \\ p_y \end{pmatrix}_{s+L_{sext}} = \begin{pmatrix} x \\ p_x \\ y \\ p_y \end{pmatrix}_s + \begin{pmatrix} 0 \\ -\frac{n}{2}(x^2-y^2)L_{sext} \\ 0 \\ nxyL_{sext} \end{pmatrix}_s \tag{3.31}$$

where n is the sextupole gradient and L_{sext} the length of the sextupole. Sextupoles drive third-order synchro-betatron resonances [Piw93].

If we now introduce the coupling between the transversal and longitudinal motion by substituting the transversal coordinates x, y by the dispersion coordinates (3.8) at each passage through the nonlinear elements and describe the linear motion by (3.29), we are able to simulate the 6-dimensional dynamics numerically.

The treatment of nonlinear elements in the kick approximation is widely used in particle tracking programs. The principle of these programs is described above. Modern tracking programs offer of course much more features such as linear optics calculations, closed orbit treatment and so on. The tracking code SIXTRACK [Wru84], [Sch91], [Wru88] will be used extensively in this work.

[c] Where μ represents again x, y or σ.

The resonance behavior of the Hamiltonian (3.20) will be numerically simulated in an artificial storage ring consisting out of a wiggler and a linear part with adjustable phase advance. Therefore the transfer matrix (3.29) and the nonlinear kick (3.30) are combined and particles tracked through this nonlinear system. The wiggler map is based on a wiggler with the parameters given in table 3.2, corresponding to a X-ray wiggler at DORIS III. The horizontal field gradient $\partial B_y/\partial x$ is increased to pronounce the resonances which are proportional to k_x. The starting amplitudes are 1cm in the horizontal and vertical plane. For simplicity the β-function is 1m everywhere. The chosen starting amplitudes ensure that the tracked particles will pass areas away from the wiggler axis. The initial longitudinal coordinates are $\sigma = 0\text{m},\ p_\sigma = 0.01$. The longitudinal tune is fixed, while the horizontal and vertical tunes are varied between 0.1 and 0.4 in steps of $\Delta Q = 0.003$. The parameters are summarized in table 3.2.

Table 3.2: *Parameters of the model storage ring with wiggler*

$\varepsilon_{x,initial}$	$1.0 \cdot 10^{-4}$ rad m
$\varepsilon_{y,initial}$	$1.0 \cdot 10^{-4}$ rad m
$\varepsilon_{\sigma,initial}$	$1.0 \cdot 10^{-4}$ MeV m
Q_x	0.1–0.4
Q_y	0.1–0.4
Q_s	0.06
k_x	25.9 m^{-1}
k_y	51.8 m^{-1}
$\frac{1}{4\rho^2 k^2}\lambda$	$7.643 \cdot 10^{-8}$ m

The resonant behavior at each pair of horizontal and vertical tunes is documented by calculating the maximum reached amplitude during 512 passages through the system. This value divided by the initial amplitudes is plotted against the horizontal and vertical tunes. To demonstrate the effect of dispersion in the wiggler, three different cases have been simulated:

- $D_1 = D_3 \equiv 0\text{m}$ in the wiggler
- $D_1 = 1\text{m},\ D_3 = 0\text{m}$ in the wiggler
- $D_1 = D_3 = 1\text{m}$ in the wiggler .

One can clearly see the influence of the wiggler on the resonance structure. Fig. 3.2a shows that without dispersion only the transversal resonances $(0, 4, 0)$ and $(2, \pm 2, 0)$ are present. Including horizontal dispersion in the wiggler, additional synchro-betatron resonances are driven, i.e the $(1, \pm 2, \pm 1)$. Fig. 3.2c presents the results with both horizontal and vertical dispersion in the wiggler. In addition to the resonances mentioned above, the $(2, \pm 1, \pm 1)$, $(0, 3, \pm 1)$, $(0, 1, -3)$ and $(1, -1, \pm 1)$ are excited, as predicted by the Hamiltonian (3.20). This proofs the correctness of the perturbation analysis. The simulation shows also, that the perturbation of the linear motion due to the wiggler is small. The maximum increase of amplitudes is only $\approx 20\%$, while the particles are passing the wiggler in its outer, i.e. nonlinear regions.

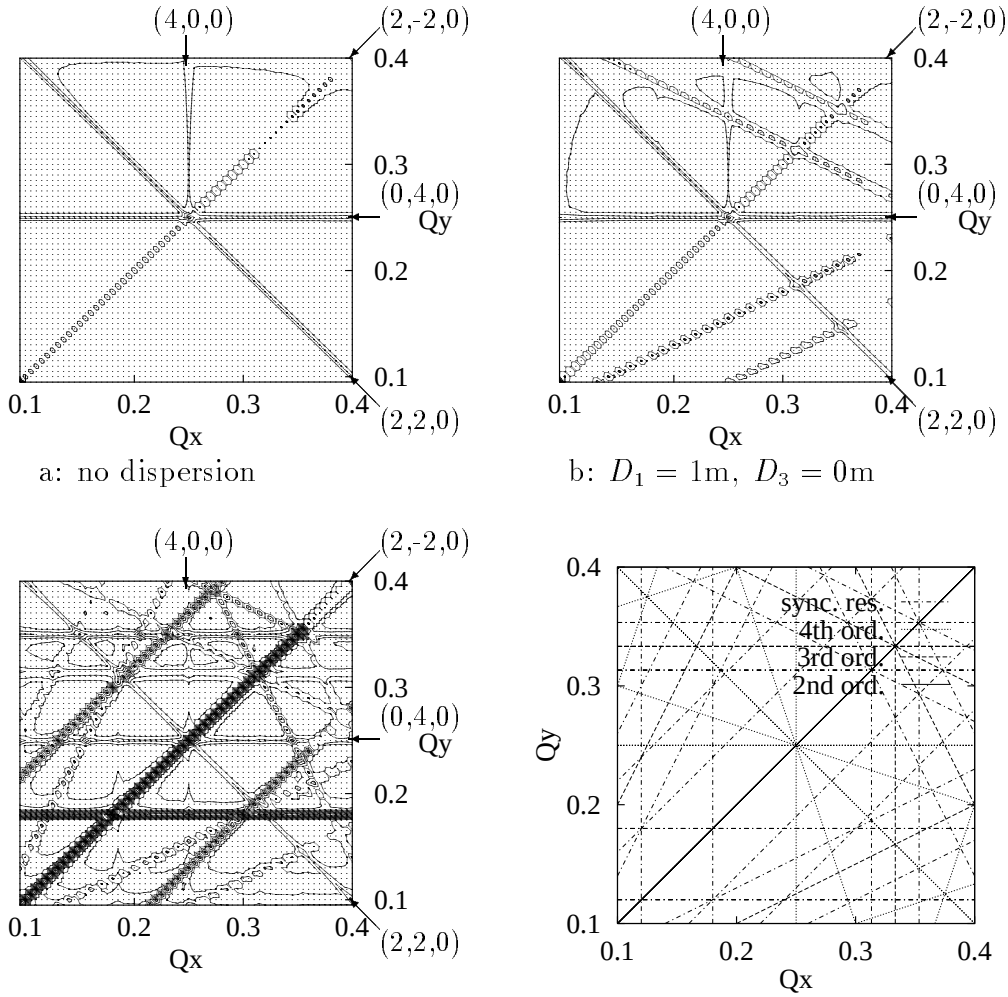

a: no dispersion

b: $D_1 = 1\text{m},\ D_3 = 0\text{m}$

c: $D_1 = 1\text{m},\ D_3 = 1\text{m}$

d: Tune diagram

Figure 3.2: *Sum of the maximum reached vertical and horizontal amplitudes during 512 turns through a nonlinear system made out of a linear transfer matrix and a wiggler kick versus the horizontal and vertical tune. Dark lines indicate larger amplitudes, the thickness of the lines is a measure of the amount of amplitude increase. The maximum amplitude increase is* $\approx 20\%$*. The dispersion has been varied between the different plots* $a - c$*, which leads to an additional excitation of synchro-betatron resonances. Plot d displays a tune diagram with synchro-betatron resonances up to 4th order.*

3.5 Transfer Maps for Arbitrary Magnetic Fields

The equations of motion have been derived for a sinusoidal wiggler with a field shape assumed to be of the 'Halbach' form (2.7). As stated in chapter 2.4, this field description is not sufficient in the outer parts of a wiggler. One may overcome this problem partly by including more and more higher harmonics, but then the analytical description becomes very complicated. A numerical method, worked out by Wüstefeld, Bahrdt, Scheer [Sch92],[BW92],[BW90],[WB91], which determines the transfer map through arbitrary magnetic fields helps to overcome this problem.

Given an initial set of canonical variables $\vec{v}_i = x_i, p_{x,i}, y_i, p_{y,i}, \sigma_i, p_{\sigma,i}$ the transfor-

mation into final variables $\vec{v}_f = x_f, p_{x,f}, y_f, p_{y,f}, \sigma_f, p_{\sigma,f}$ can be expanded into a Taylor series for each final variable up to the order O in the initial coordinates:

$$\begin{aligned} \mu_f &= \sum_{\nu_1+\nu_2+\nu_3+\nu_4+\nu_5+\nu_6=0}^{O} a^{(\mu)}_{\nu_1\nu_2\nu_3\nu_4\nu_5\nu_6}\, x_i^{\nu_1}\, p_{x,i}^{\nu_2}\, y_i^{\nu_3}\, p_{y,i}^{\nu_4}\, \sigma_i^{\nu_5}\, p_{\sigma,i}^{\nu_6} \\ p_{\mu,f} &= \sum_{\nu_1+\nu_2+\nu_3+\nu_4+\nu_5+\nu_6=0}^{O} a^{(p_\mu)}_{\nu_1\nu_2\nu_3\nu_4\nu_5\nu_6}\, x_i^{\nu_1}\, p_{x,i}^{\nu_2}\, y_i^{\nu_3}\, p_{y,i}^{\nu_4}\, \sigma_i^{\nu_5}\, p_{\sigma,i}^{\nu_6} \end{aligned} \tag{3.32}$$

where $a^{(\mu)}_{\nu_1\nu_2\nu_3\nu_4\nu_5\nu_6}$, $a^{(p_\mu)}_{\nu_1\nu_2\nu_3\nu_4\nu_5\nu_6}$ are the expansion coefficients. Equation (3.32) reads in matrix notation:

$$\vec{v}_f = \mathbf{A}\vec{b}_i \tag{3.33}$$

with $\mathbf{A}$ and $\vec{b}_i$ defined above. The coefficients $a^{(q)}_{\nu_1\nu_2\nu_3\nu_4\nu_5\nu_6}$, $a^{(p_\mu)}_{\nu_1\nu_2\nu_3\nu_4\nu_5\nu_6}$ can be derived numerically. With a number of N different sets of canonical variables $\vec{v}_{i,1\cdots N}$, $\vec{v}_{f,1\cdots N}$ one can set up a system of equations of the form:

$$\begin{pmatrix} \mu_{f,1} \\ \vdots \\ \mu_{f,N} \end{pmatrix} = \vec{A}_\mu \cdot \begin{pmatrix} \vec{b}_{i,1} \\ \vdots \\ \vec{b}_{i,N} \end{pmatrix}$$

for all variables μ, p_μ. By applying the Gaussian principle (see appendix A) we derive another system of equations which is overdetermined and can be solved by the method of Householder [EMR88].

Thus, one only has to track a number of particles distributed randomly in the six-dimensional phase space through a magnetic field and plug the initial and final coordinates into the equations above and obtains a Taylor map which defines the transfer through the considered device. We will call the obtained set of Taylor coefficients a numerical Taylor map of the wiggler. The number of particles needed is given by the order of the expansion and the required accuracy. The accuracy is measured by the relative error of the map, which is defined as the rms-value of the difference between the final coordinates $\vec{v}_f$ and the coordinates derived by the Taylor map $\vec{V}_f = X_f, P_{X,f}, Y_f, P_{Y,f}, \Sigma_f, P_{\Sigma,f}$, divided by the mean value of the root of the squared sum of the final coordinates [Sch92]:

$$\begin{aligned} \chi^2 &= \sum_{n=1}^{N} \Big((X_f - x_f)^2 + (P_{X,f} - p_{x,f})^2 + \\ &\quad (Y_f - y_f)^2 + (P_{Y,f} - p_{y,f})^2 + (\Sigma_f - \sigma_f)^2 + (P_{\Sigma,f} - p_{\sigma,f})^2 \Big) \end{aligned} \tag{3.34}$$

$$\bar{\chi} = \frac{\sqrt{\frac{\chi^2}{N}}}{\frac{1}{N}\sum_{n=1}^{N}\sqrt{x_f^2 + p_{x,f}^2 + y_f^2 + p_{y,f}^2 + \sigma_f^2 + p_{\sigma,f}^2}} \tag{3.35}$$

If we neglect radiation and orbit lengthening effects, the transfer map simplifies. Considering only fields which are constant in time, the arrival time σ does not have any influence, so we have to deal with the coefficients $a_{\nu_1\nu_2\nu_3\nu_4\nu_6}$ only. In the following we will only consider particles with no energy deviation. Thus the number of coefficients reduces again to $a_{\nu_1\nu_2\nu_3\nu_4}$. A map of 4th order has 69 coefficients, 6th order gives 209

coefficients per variable, which is the minimum number of particles to be tracked. In general, we have tracked a slightly larger number of particles, i.e. 100 at 4th order and 300 at 6th order which gives a sufficient accuracy (see below).

An expansion up to first order yields the linear transfer matrices. $\bar{\chi}$ will then be a measure of the nonlinear content of the considered magnetic field. This is an elegant way to proof the validity of the expansion. Tracking through a quadrupole with a theoretical transfer matrix [RS94]:

$$\mathbf{M_x} = \begin{pmatrix} 1.010017 & 0.10033367 \\ 0.20067 & 1.010017 \end{pmatrix}, \mathbf{M_y} = \begin{pmatrix} 0.990018 & 0.0996670 \\ -0.19933 & 0.990018 \end{pmatrix}$$

yields a Taylor expanded transfer map of:

$$\mathbf{M_x} = \begin{pmatrix} 1.010012 & 0.10033369 \\ 0.20068 & 1.010026 \end{pmatrix}, \mathbf{M_y} = \begin{pmatrix} 0.990021 & 0.0996675 \\ -0.19935 & 0.990024 \end{pmatrix}.$$

The average relative error becomes $\bar{\chi} \approx 1.0 \cdot 10^{-5}$. The coupling coefficients of the map are in the order of 10^{-6} or smaller. The re-calculated quadrupole strength differs from the original one by $\approx 5.0 \cdot 10^{-5}$, which is far below the accuracy reached in practice.

The expansion used above is not symplectic, which means that the phase space area is not conserved under the transformation defined above. Using the concept of generating functions [Gol85] overcomes this problem. A canonical transformation defined by an appropriate generating function $F(x_i, p_{x,f}, y_i, p_{y,f})$ maps the canonical variables $x_i, p_{x,f}, y_i, p_{y,f}$ into $x_f, p_{x,i}, y_f, p_{y,i}$:

$$\begin{aligned} x_f &= \frac{\partial F}{\partial p_{x,f}} \\ y_f &= \frac{\partial F}{\partial p_{y,f}} \\ p_{x,i} &= \frac{\partial F}{\partial x_i} \\ p_{y,i} &= \frac{\partial F}{\partial y_i} \end{aligned} \tag{3.36}$$

By expanding F into a Taylor series such as (3.32) from $\nu_1 + \nu_2 + \nu_3 + \nu_4 = 1 \ldots O$, one gets together with the defining equations of the generating function a system of equations which allows to determine the coefficients $a_{\nu_1\nu_2\nu_3\nu_4}$ of the series [Sch92]. This set of coefficients will be called the numerical generating function of a wiggler.

If we want to use the numerical generating function in a tracking code, we have to map of course the initial into the final coordinates. The implicit dependence (3.36) of the final on the initial coordinates is solved via a Newton search [BS89], where one has to estimate the final coordinates. This can be done by using the numerical Taylor map or by any analytical estimation of the particle transfer through the magnetic field.

Despite this it is possible to extract the linear, coupled transfer map out of the numerical generating function. Thus we can proof the map in the same way as above.

We will now analyze the wiggler used in chapter 3.4 with the maps discussed above. The linear transfer matrices become for one period of the wiggler:

$$\mathbf{M_{theo}} = \begin{pmatrix} 1.000007 & 0.1400003 & 0.0 & 0.0 \\ 1.0267 \cdot 10^{-4} & 1.000007 & 0.0 & 0.0 \\ 0.0 & 0.0 & 0.9999713 & 0.1399987 \\ 0.0 & 0.0 & -4.1068 \cdot 10^{-4} & 0.9999713 \end{pmatrix}$$

$$\mathbf{M_{tay}} = \begin{pmatrix} 1.000007 & 0.1400008 & 7.7 \cdot 10^{-9} & -2.1 \cdot 10^{-8} \\ 1.0246 \cdot 10^{-4} & 1.000007 & -2.7 \cdot 10^{-7} & -1.1 \cdot 10^{-7} \\ 9.9 \cdot 10^{-8} & -1.8 \cdot 10^{-7} & .9999716 & .1399985 \\ 4.8 \cdot 10^{-7} & -1.3 \cdot 10^{-5} & -4.1086 \cdot 10^{-4} & .9999713 \end{pmatrix}$$

$$\mathbf{M_{gen}} = \begin{pmatrix} 1.000008 & 0.1400016 & -1.7 \cdot 10^{-6} & -4.0 \cdot 10^{-6} \\ 1.0356 \cdot 10^{-4} & 1.000006 & 5.9 \cdot 10^{-7} & -1.3 \cdot 10^{-6} \\ 1.4 \cdot 10^{-6} & -3.6 \cdot 10^{-6} & 0.9999678 & 0.1399976 \\ 5.9 \cdot 10^{-7} & 1.8 \cdot 10^{-6} & -4.0863 \cdot 10^{-4} & 0.9999750 \end{pmatrix}.$$

The expansion is performed up to fourth order. $\mathbf{M_{theo}}$ denotes the linear transfer matrix obtained by using the focusing strength of (3.21), while $\mathbf{M_{tay}}$ is the transfer matrix of the numerical Taylor map and $\mathbf{M_{gen}}$ is the one calculated from the numerical generating function. The $\bar{\chi}$ of the expansions is in the order of 10^{-6}. The differences in the linear transfer matrices are due to the numerical errors of the computer routines. These small differences could be reduced further by increasing the accuracy of the numerical methods.

With the coefficients of the numerical Taylor map it is possible to proof the non-linear content of the Hamiltonian (3.20). The corresponding coefficients become:

coefficient	Taylor map	Hamiltonian
$a^{(p_x)}_{3000}$	$-4.26 \cdot 10^{-2}$	$-4.59 \cdot 10^{-2}$
$a^{(p_y)}_{0030}$	-0.74	-0.73
$a^{(p_x)}_{1020}$	0.183	0.207
$a^{(p_y)}_{2010}$	0.194	0.207

The considered coefficients are the leading terms of the expansion. The difference between the nonlinear terms is in the order of 10% only. Thus the Hamiltonian (3.20) is sufficient to estimate the nonlinear beam dynamics effects due to a wiggler. A detailed analysis has to be done with more accurate methods, such as the transfer maps described above.

The effect of the 'symplectification' is illustrated in the following. Particles with different initial vertical amplitudes have been tracked through a model storage ring, consisting of a nonlinear kick due to the numerical Taylor map or numerical generating function of the wiggler and a linear transfer map, which adjusted the tune to be in the vicinity of the (0,4,0) resonance. The left figure 3.3 is generated with the numerical Taylor map. One clearly sees a blow up of the phase space at large amplitudes. The right figure 3.3 is obtained with the numerical generating function. The smear of the phase space trajectories at large amplitudes vanishes. To illustrate the effect of the wiggler on the phase space, a phase space plot without any nonlinear element is shown in figure 3.4. The phase space is not perturbed at all. It should be remarked here, that a

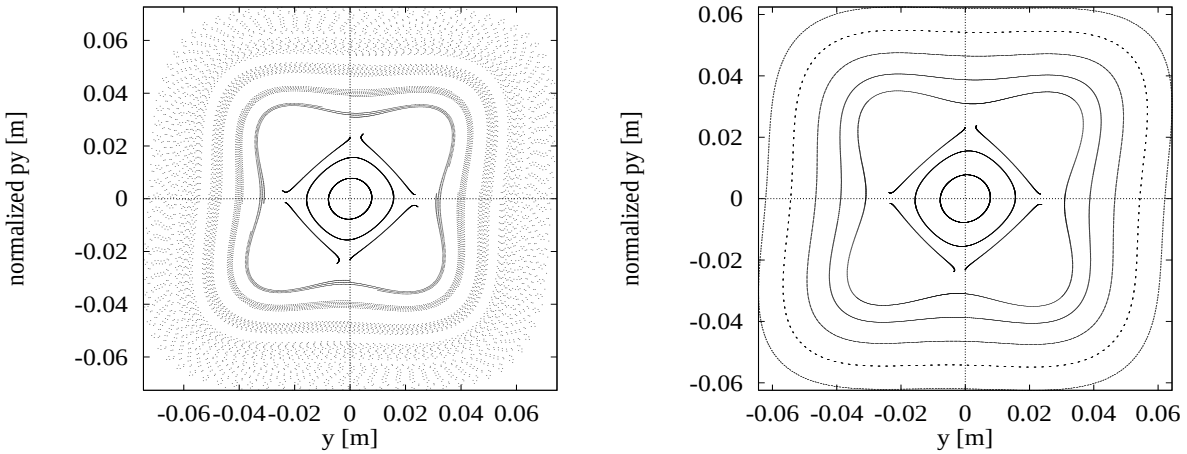

Figure 3.3: *Normalized vertical phase space with an unperturbed Q-value of* $Q_y = .238$ *in the presence of a wiggler*
Left: *generated by the numerical Taylor map of the wiggler*
Right: *generated by the numerical generating function of the wiggler*

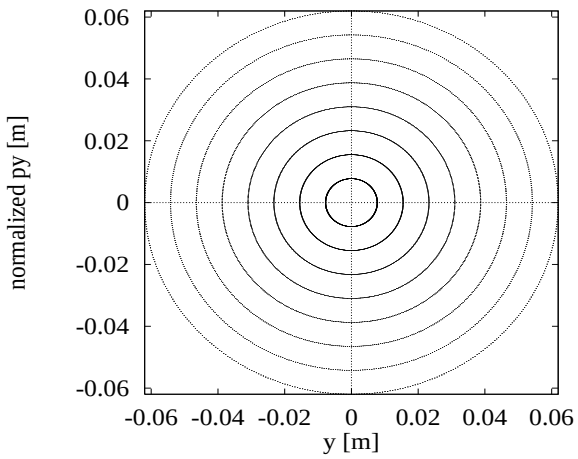

Figure 3.4: *Normalized vertical phase space with a Q-value of* $Q_y = .238$ *and no additional nonlinear elements*

significant perturbation of the phase space occurs at amplitudes of $\approx$ 2cm, which would be outside the wiggler vacuum chamber.

The method of generating functions together with the analytical field descriptions was used in [BW92],[BW90],[WB91] to create an analytical Taylor expansion of the generating function and thus a canonical transfer map up to a certain order. We will compare the second order generating function given in [BW90] with the other tracking methods in the following chapter.

3.6 Comparison of the Different Transfer Maps for Wigglers

Two different wigglers will be used to compare the transfer maps which have been derived in the previous chapters or are given elsewhere [BW90], [Smi86]. The parameters of the considered wigglers are summarized in table 3.3, they are similar to the devices presented in chapter 2.4 but only the first harmonic is used. The short-period wiggler, named undulator for better distinction, will be analyzed with a particle energy of 1.5GeV and the wiggler #2 with a particle energy of 4.5GeV.

Table 3.3: *Parameters of the undulator and wiggler used for the comparison of transfer maps*

	#1 undulator	#2 wiggler
# of periods	100	28
λ [m]	0.03	0.14
gap [mm]	15	30
pole width [mm]	80	100
$(k_x/k_y)^2$	$-9.0 \cdot 10^{-4}$	-0.0625
energy [GeV]	1.5	4.5
B_1 [T]	0.4865	1.0723

The resulting kicks for different initial conditions will be compared for the following transfer maps:

1. A Runge-Kutta integration of the equations of motion with the magnetic fields given in (2.7). The step size is fixed to 200 steps per period .
2. The equations of motion derived from the Hamiltonian (3.28) solved by a Runge-Kutta integrator with a fixed step size of 100 steps per period.
3. The equations of motion derived from the Hamiltonian (3.20) in the kick approximation (i.e. transfer function (3.30)).
4. The analytic generating function given in [BW90].
   (a) With a step size of 28 periods for the wiggler (#2) and 100 periods for the undulator (#1), i.e. one step over the whole length of the device.
   (b) With a step size of 10 periods for the undulator and 7 periods for the wiggler, i.e. 10 respectively 4 steps for the whole device.
   (c) With a step size of 1 period in both cases.
5. The numerical Taylor map (3.32).
   (a) Expanded up to 6th order.
      i. Derived for 1 period.

ii. Derived for all periods.

(b) Expanded up to 4th order.

i. Derived for 1 period.

ii. Derived for all periods.

6. The numerical generating function.

(a) Expanded up to 6th order.

i. Derived for 1 period.

ii. Derived for all periods.

(b) Expanded up to 4th order.

i. Derived for 1 period.

ii. Derived for all periods.

The kick resulting from the linear focusing term is also evaluated. The different maps are compared by evaluating the absolute error with respect to the Runge-Kutta integration (1.):

$$\chi_{abs} = |(\Delta\mu')_{ruku} - (\Delta\mu')_{map}|$$

Figures 3.5 – 3.7 show the results obtained for the wiggler. The labels in brackets refer to the different maps as listed above.

In figure 3.5 the resulting linear and nonlinear kick obtained from the Runge-Kutta integration (1.) are plotted for purely horizontal (left) or vertical (right) initial positions. Due to the symmetry of the fields there is no effect in the other plane if the particles do not deviate from the origin of the other plane. The weak defocusing in the horizontal direction and the focusing effect in the vertical direction are clearly seen. Figure 3.6 gives the absolute error χ_{abs} for the analytical maps. The absolute error is smaller than $\approx 4 \cdot 10^{-7}$rad in the horizontal and $\approx 4 \cdot 10^{-6}$rad in the vertical, leading to a relative

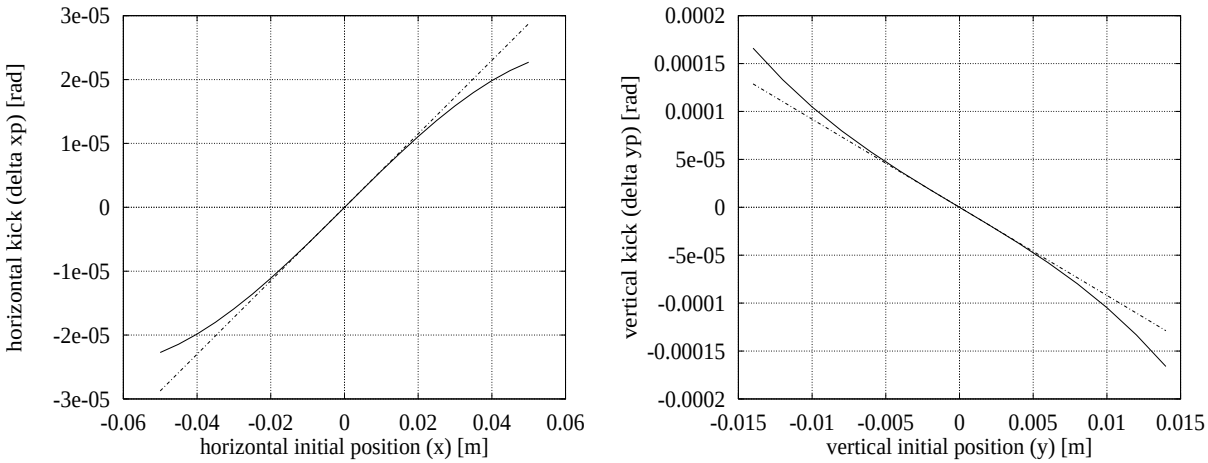

Figure 3.5: *Resulting horizontal/vertical kicks at different initial horizontal (left) or vertical (right) coordinates for the wiggler derived by the Runge-Kutta integration (1.) (solid line) and due to the linear focusing term (dashed-dotted line).*

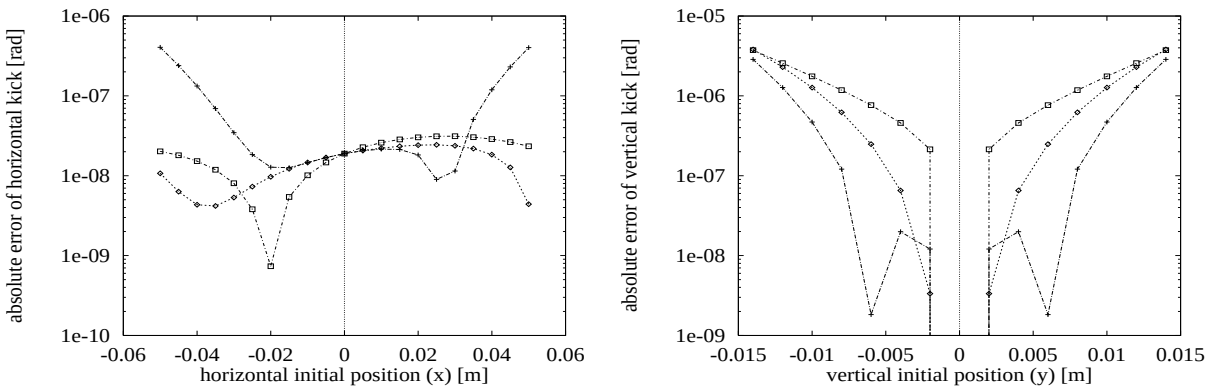

Figure 3.6: *Absolute error of resulting horizontal/ vertical kicks due to varying horizontal (left) and vertical (right) coordinates, derived by the difference between the Runge-Kutta integration (1.) and the different analytical transfer maps for the wiggler:*
$\diamond$*: Smith Hamiltonian (2.)* $+$*: Hamiltonian (3.)*
$\square$ *: analytical generating function (4.(a))*

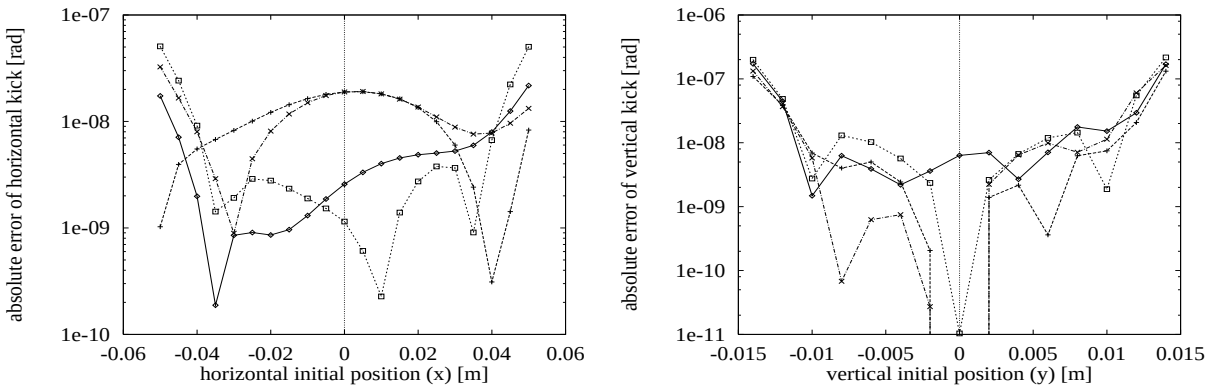

Figure 3.7: *Absolute error of resulting horizontal/ vertical kicks due to varying horizontal (left) and vertical (right) coordinates, derived by the difference between the Runge-Kutta integration 1. and the different numerical transfer maps for the wiggler:*
$\diamond$*: numerical Taylor map for 1 period of the wiggler (5.(a)i)*
$+$*: numerical generating function for 1 period (6.(a).i)*
$\square$*: numerical Taylor map for 28 periods (5.(a)ii)*
$\times$*: numerical generating function for 28 periods (6.(a).ii)*

error of $\approx 1-2\%$ for the resulting kick after the passage with large horizontal or vertical amplitudes through the whole wiggler. The errors of the numerically obtained maps are displayed in figure 3.7. The absolute errors are smaller by a factor of 10. There is no significant difference between the maps obtained for one period, which has to be passed 28 times or the maps for the whole wiggler, i.e. the passage through all 28 periods integrated in one map.

The undulator is analyzed only for different vertical coordinates because the dependence of the field on the horizontal coordinates is very small ($kx/ky = 0.03$). Figure 3.8 shows the resulting kick obtained from the Runge-Kutta integration (1.) and the linear focusing. The linear focusing is comparable to the one previously discussed, while

the undulator shows a much stronger non-linear behavior, which can be seen also from (3.20) and (3.22). The pseudo-octupole term is proportional to $1/\lambda^2$.

The resulting absolute error is $\approx 1.0 \cdot 10^{-5}$rad for the analytical maps. This leads to a large relative error of $\approx 10\%$. Note that if the step-length of the analytical generating function is decreased from 1 step per undulator to 10 steps per undulator the error decrease by two orders of magnitude, leading to a satisfying relative error of $\approx 0.1\%$. The error of the numerical maps is in the order of 10^{-6}rad, or $\approx 1\%$ relative error.

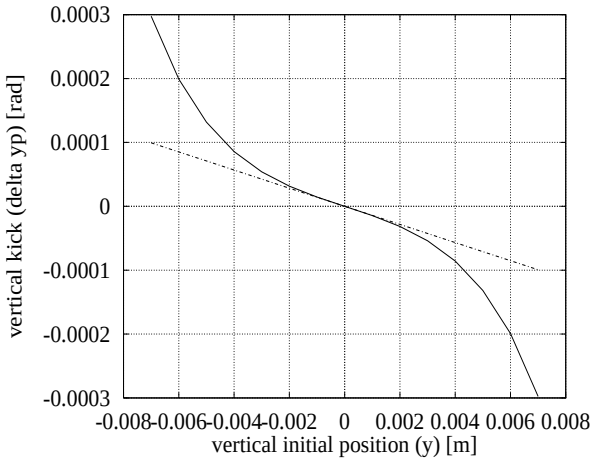

Figure 3.8: *Resulting vertical kicks at different initial vertical coordinates for the undulator derived by the Runge-Kutta integration (1.) (solid line) and due to the linear focusing term (dashed-dotted line).*

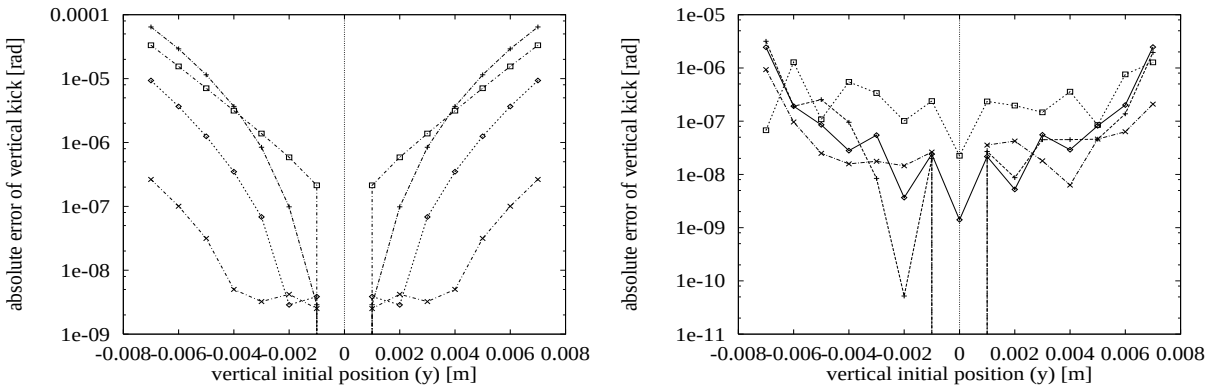

Figure 3.9: *Absolute error of resulting vertical kicks due to varying vertical coordinates, derived by the difference between the Runge-Kutta integration (1.) and the different analytical (left) or numerical (right) transfer maps for the undulator:*
Left: $\diamond$*: Smith Hamiltonian (2.)* $+$*: Hamiltonian (3.)*
$\square$ *: analytical generating function (4.(a)) with 1 step per undulator*
$\times$ *: analytical generating function (4.(b)) with 10 steps*
Right: $\diamond$*: numerical Taylor map for 1 period (5.(a).i)*
$+$*: numerical generating function for 1 period (6.(a).i)*
$\square$*: numerical Taylor map for 100 periods (5.(a).ii)*
$\times$*: numerical generating function for 100 periods (6.(a).ii)*

Up to now, we have only compared the behavior of the different maps by varying one of the initial transversal coordinates x or y, leaving all others zero. This illustrates the different nonlinear behavior of a short and a long period device and it shows the enlargement of the absolute errors with increasing transversal amplitudes, but it does not take into account a coupling of the motion from one transversal plane to the other. Therefore we will compare the different transfer maps for arbitrary sets of initial coordinates distributed in the 4-dimensional phase space. The comparison will be done by computing the average relative error given in (3.35). The results for a set of 20 randomly distributed initial coordinates are summarized in table 3.4. The 'number of map' corresponds to the list given at the beginning of this chapter.

Table 3.4: *Relative average error due to different wiggler transfer maps and elapsed CPU-time for one passage through the maps*

	$\bar{\chi}$		CPU-time
number of map	#1 undulator	#2 wiggler	arbitrary units
1.	0.0	0.0	2664
2.	$3.1 \cdot 10^{-4}$	$1.3 \cdot 10^{-4}$	698
3.	$2.3 \cdot 10^{-3}$	$3.5 \cdot 10^{-4}$	1
4.(a)	$6.6 \cdot 10^{-3}$	$2.5 \cdot 10^{-3}$	1
4.(b)	$6.0 \cdot 10^{-5}$	$1.5 \cdot 10^{-4}$	2
4.(c)	$4.9 \cdot 10^{-5}$	$4.0 \cdot 10^{-6}$	5
5.(a)i.	$1.4 \cdot 10^{-5}$	$2.9 \cdot 10^{-6}$	868
5.(a)ii.	$9.8 \cdot 10^{-5}$	$3.1 \cdot 10^{-6}$	30
5.(b)i.	$6.0 \cdot 10^{-4}$	$6.9 \cdot 10^{-5}$	416
5.(b)ii.	$5.7 \cdot 10^{-4}$	$5.8 \cdot 10^{-5}$	14
6.(a)i.	$7.1 \cdot 10^{-5}$	$2.0 \cdot 10^{-6}$	4264
6.(a)ii.	$8.6 \cdot 10^{-5}$	$1.1 \cdot 10^{-6}$	158
6.(b)i.	$6.8 \cdot 10^{-4}$	$6.0 \cdot 10^{-5}$	2639
6.(b)ii.	$7.4 \cdot 10^{-4}$	$2.7 \cdot 10^{-5}$	95

It turns out, that due to the stronger nonlinearities of the undulator the error is about a factor of 10 larger than for the wiggler. In both cases the accuracy of the analytic generating function as well as the numerically derived maps are high enough for tracking purposes. The Hamiltonian (3.20), which was used for the analysis of resonance driving terms, produces the biggest error, but it still represents the nonlinearities well enough to get an easy and quick estimate of the wiggler or undulator effects on the beam dynamics.

For tracking purposes a comparison of CPU-time is interesting, because the transfer maps have to be passed many times. The elapsed CPU-time for one passage through the wiggler is also given in table 3.4. The two analytic maps (3.) and (4.) are the fastest. We will use them for the analysis of effects due to an ideal wiggler. The advantage of the numerically computed maps is the possibility of treating magnetic fields which are not given in a closed analytic form, respectively in a very complicated one. Thus they will be used for the investigation of more detailed field descriptions.

4 Numerical Investigation of Wiggler Effects

After we have introduced the various treatments of wigglers and undulators in tracking codes, a detailed numerical investigation of the wiggler effects on beam dynamics follows. First some general remarks on the tracking philosophy will be given. The tracking calculations have been performed for the DORIS III storage ring. Thus a short summary of DORIS III follows. The effects of errors and other properties of the wiggler fields are analyzed, and after all the resonance pattern as well as the dynamic acceptance of DORIS with wigglers and undulators will be derived.

4.1 General Remarks

The basic philosophy of single particle tracking is the observation of a particle started with certain initial parameters during its multi-turn voyage through the given magnet structure. One can then analyze the turn by turn data and obtain for example the particle tune or the enclosed phase space area. By varying the initial parameters it is possible to get tune shift with amplitude, the number of stable turns or even a qualitative information about the beam sizes in dependence on the initial parameters.

To investigate the beam dynamics of a real storage ring, it is necessary to get an exact model of the ring. This includes the magnet lattice which determines the linear optical functions, as well as the magnet errors which are present in the accelerator magnets. Because DORIS suffers mainly from synchrotron resonances, it is also worthwhile to include the longitudinal particle dynamics in the model. A tracking code such as SIXTRACK [Sch91],[Rip85],[Wru84] can handle all these requirements. It allows tracking through any kind of accelerator optics under the thin lens approximation for nonlinear elements. As a part of this work, the transfer maps for wigglers which have been introduced in chapter 3 have been included in SIXTRACK.

For electron storage rings, it is usually sufficient to track the particle for a number of turns corresponding to the damping times of the betatron and synchrotron oscillations. We have neglected the influence of energy loss due to synchrotron radiation in the tracking calculations. Synchrotron oscillations are excited by starting particles with initial relative energy deviations of $\approx 1\%$ in the tracking. The average energy loss per turn is $< 0.1\%$, thus one order of magnitude smaller than the investigated off energy particles. Nonlinear effects due to dispersion trajectories are thus covered by the investigations. Neglecting synchrotron radiation means also that the radiation damping is not taken into account. This is the reason for the small number of tracked turns.

We will focus our analysis on two problems: the onset of resonances and the dynamic acceptance.

The onset of resonances is determined in the following way: A particle with a certain start amplitude in the 6-dimensional phase space is tracked for a number of turns. The particle may get lost due to an enlargement of its amplitude at geometrical aperture limits which are introduced corresponding to the ones in the real machine. The initial amplitudes are chosen to correspond to that aperture, which guarantees a lifetime of 1 hour in the real machine (see appendix B for a discussion of the dependency of lifetime on aperture). A particle which survives a certain number of turns corresponds to a lifetime better than 1 hour, or less than 1 hour in the other case.

The tracking is done at different tune values. The tune change is performed through an artificial tune shift element, which keeps all other optical functions unchanged. This allows to distinguish between nonlinear effects and those which are due to a change in the linear optics [Wil90]. Such an element of the kind:

$$\begin{pmatrix} \cos(2\pi\Delta Q_\mu) + \alpha_\mu \sin(2\pi\Delta Q_\mu) & \beta_\mu \sin(2\pi\Delta Q_\mu) \\ -\gamma_\mu \sin(2\pi\Delta Q_\mu) & \cos(2\pi\Delta Q_\mu) - \alpha_\mu \sin(2\pi\Delta Q_\mu) \end{pmatrix} \tag{4.1}$$

changes the tune by ΔQ_μ in the particular plane. The optical functions α_μ, β_μ, γ_μ have to be taken at the position of the element. This artificial element has also been introduced in SIXTRACK.

The dynamic acceptance or aperture is the largest stable transversal or longitudinal phase space area. The phase space area can be calculated from the turn by turn particle coordinates. The maximum stable area is derived by increasing successively the initial particle coordinates until the particle gets lost within a certain number of turns. A comparison of the dynamic acceptance under different machine parameter settings can be done by just comparing the maximum stable initial amplitudes.

In order to investigate the real machine, we have usually introduced the realistic geometric aperture limitation in the tracking runs. Thus effects on the dynamic acceptance which occur for particles outside the vacuum chamber are not taken into account. On the other hand, we derive the realistic dynamic acceptance of the machine, considering also amplitude increases on resonance islands which overlap the geometric aperture. The influence of a decrease of the geometric aperture, for example due to smaller vacuum chambers at the wiggler locations, could also be investigated.

4.2 The Synchrotron Radiation Source DORIS III

DORIS III is a state of the art so-called first generation[a] synchrotron light source [N+92],[BNR88]. Originally designed as a high energy physics $e^+ - e^-$ collider for energies of up to 5.6 GeV, it was used since 1982 parasitically for synchrotron radiation experiments. To increase the number of high quality beam lines by providing more space for insertion devices, the so-called 'Bypass' was constructed in one of the two straight sections of the racetrack shaped ring. This was completed in 1991 and after two more years of partly dedicated synchrotron radiation operation, DORIS III serves since 1993

[a] The various light source generations are defined in chapter 1.

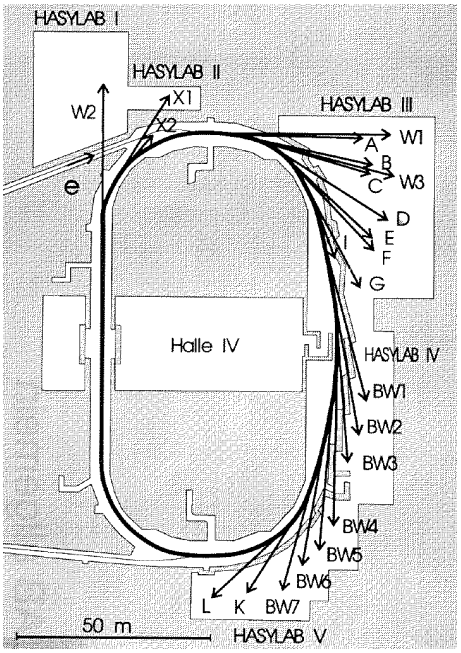

Figure 4.1: *Schematic view of DORIS III with synchrotron radiation beam lines. The so-called Bypass is the bump in the right (former straight) section of the ring. Wiggler beam lines are denoted with BW1-7 in the Bypass and W1-3 in the rest of the ring. The others are bending magnet beam lines. (from [HAS94])*

as a dedicated synchrotron light source. The nominal beam energy is 4.5 GeV, thus the radiation spectrum has its maxima in the X-ray region (see figure 2.1), but due to the long tradition of synchrotron radiation research at DESY [DES94], experiments with all parts of the synchrotron radiation spectrum are performed [HAS94].

The ring consists out of two straight sections and two nearly 180° arcs. One of the straight sections contains the 'Bypass', a slight bump which allows to install seven wigglers with a length of 4m. The other straight section contains the rf-cavities and the former high energy physics experimental area, which includes a vertical bump as an artifact of the synchrotron radiation shielding system of the high energy physics detector ARGUS. This bump is responsible for the vertical dispersion in the ring. It will be removed until the beginning of 1996. Three more wigglers are distributed in free spaces around the ring, yielding a total number of 10 wigglers which cover $\approx 10\%$ of the ring circumference. Figure 4.1 shows an overview of the storage ring with the synchrotron radiation beam lines.

The lattice consists out of quadrupole triplets in the arcs and doublets in the straight sections. The optical functions are plotted in figure 4.2 for one half of the ring. The optical functions of the other half are mirror symmetric. Figure 4.3 shows the 'Bypass' section which contains most of the insertion devices. Note the horizontal and vertical dispersion, which does not vanish in the wiggler straight section. The straight sections in the bypass are named BW1 – BW7, while the three wiggler positions in the rest of the ring are named W1 – W3. The optical functions at the wiggler positions are listed in appendix C.

During the measurement periods the optic was modified several times. In the be-

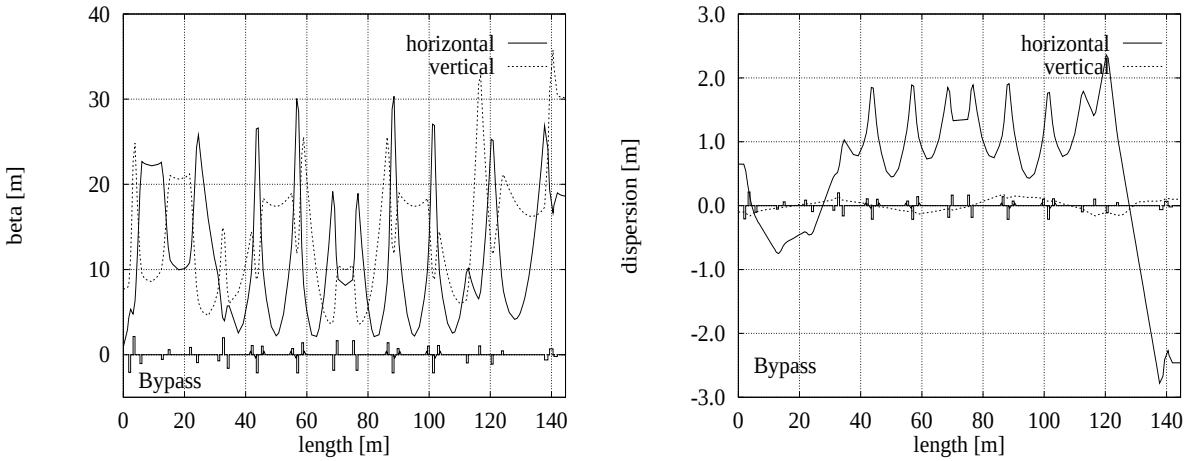

Figure 4.2: *Optical functions of one half of DORIS (mid of one straight section to mid of the other straight section). The boxes at the zero line symbolize the quadrupoles with their relative strength and sign.*[a]
Left: *β-function* Right: *Dispersion*

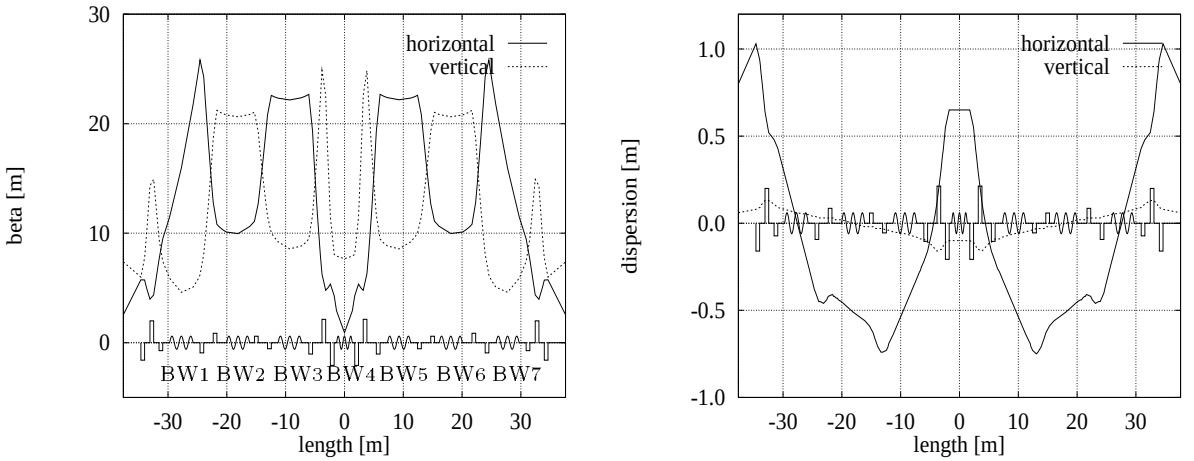

Figure 4.3: *Optical functions at the 'Bypass'. The boxes at the zero line symbolize the quadrupoles, the wiggles denote the wiggler or undulator positions.*[a]
Left: *β-function* Right: *Dispersion*

[a]The plotted optics version is the optic 'BTH1', which was used in 1994 and 1995.

ginning we had to handle two optics, for luminosity or synchrotron radiation runs respectively. After the close down of the high energy physics experiment, the mini-beta insertion was omitted in one of the straight sections. This shifted the vertical tune from below an integer to a value above an integer. The optical functions at the wiggler locations remained nearly unchanged.

The chromaticity is corrected by two sextupole families, with the sextupoles located near the corresponding quadrupoles in the two arcs of the ring. Additional sextupoles are built in in the straight sections. They are not in use because tracking calculations showed that they do not have a positive influence on the dynamic acceptance. The

tracking calculations in this work are usually performed with the two sextupole families tuned to give a slight positive chromaticity of ≈ 1.

Appendix C summarizes some of the main storage ring parameters.

4.2.1 Wigglers and Undulators at DORIS III

As stated above, DORIS is equipped with 10 different wigglers and undulators. All of them are built in permanent magnet technology. The devices cover a range from a 3.14cm period undulator to a 2T high field wiggler, optimized for different experimental requirements. A key role plays the 14cm period wiggler for X-ray radiation, which is mounted at 4 different positions. The somehow classical wigglers and undulators are accompanied by the so-called asymmetric wiggler (see chapter 2.7) which produces circularly polarized synchrotron radiation [Pfl92],[Pfl93b]. The construction of the wiggler supports allows the mounting of every wiggler at any position in the Bypass.

Most of the straight sections containing wigglers allow a minimum magnet gap of 30 mm, yielding a geometric aperture of $\approx$ 24mm. The X-ray undulator and the X-ray wiggler 'HARWI' are equipped with a variable vacuum chamber, the former allows a variation of the gap down to 14mm.

Table 4.1 summarizes some properties of all DORIS wigglers and undulators. Besides the characterizing parameters period length λ, gap and peak on-axis field B_{max}, the corresponding inverse vertical focal length $1/f$ and pseudo-octupole strength o (integrated over the wiggler length) have been calculated from (3.21) and (3.22). For completeness, the bending magnet is also mentioned. The lower 3 devices are distributed around the ring, while the others are located in the 'Bypass'. The short name will be used in the following text to characterize a specific device. Appendix C gives a table with more details on the wigglers and undulators and summarizes the optical functions at the locations of the devices.

Table 4.1: *List of DORIS III wiggler and undulator parameters*

name of wiggler	short name	λ cm	number of periods	B_{max} T	gap cm	$1/f$ m^{-1}	o m^{-3}
X-Ray Wiggler	X-WIG	14.0	28	1.17	3.0	.012	16.0
Hard X-Ray Wiggler	*HARWI2*	*22.6*	*17*	*2.0*	*2.0*	*.036*	*18.6*
Asymmetric Wiggler	ASYH	22.0	18	1.17	3.0	.005	2.7
Triple XUV Undulator	*XUV I-III*	*9.–18.6*	*44–21*	*$\approx$ 0.6*	*3.0*	*.003*	*3–9*
X-Ray Undulator	XU	3.14	127	0.8	1.4	.006	160
X-Ray Wiggler	HARWI	24.	10	1.25	3.0	.008	3.7
Wiggler-Undulator	*W1*	*13.2*	*16*	*0.6*	*3.4*	*.002*	*3.0*
Mini-Wiggler	W3	12.	4	0.3	5.8		
Bending Magnet				1.25			

4.3 Effects of Field Errors

4.3.1 Periodicity Error

Periodicity errors have an influence on the beam dynamics because the nonlinear fields of the wiggler do not average out within one period. We have performed detailed investigations of the effects of periodicity errors with the help of the current sheet model and the numerically evaluated generating functions. Several generating functions up to 6th order have been generated for different periodicity errors of the undulator and wiggler which are described in chapter 2.4. The error can be parameterized by the difference in the peak on-axis fields:

$$(\Delta B)_{rms} = \left(\frac{B_{y,max} - < B_{y,max} >}{< B_{y,max} >} \right)_{rms}$$

where $< B_{y,max} >$ is the mean peak field and the variance of the period length:

$$(\Delta \lambda)_{rms} = \left(\frac{L_{peak-peak} - \lambda}{\lambda} \right)_{rms}$$

where λ is the unperturbed period length and $L_{peak-peak}$ is the distance from peak to peak of the vertical on-axis field. The error sets have been chosen in a way to ensure an overall first field integral which is smaller than the commonly measured one. The field integrals of one period are allowed to exceed these values. The dynamic acceptance was calculated for DORIS with the different generating functions included in the tracking. The results are summarized in the following:

$(\Delta B)_{rms}$ %	$(\Delta \lambda)_{rms}$ %	acceptance in arbitrary units	
		horizontal	vertical
0.0	0.0	1.0	1.0
6.0	2.0	1.0	1.0
15.0	3.0	0.85	0.85
3.0	6.0	0.85	0.7
42.0	6.0	0.0	0.0

It turns out that an amplitude error of 6.0% does not have any influence on the dynamic acceptance. An error in the periodicity bigger than 2.0% reduces the dynamic acceptance in both planes. Much stronger requirements on these quantities are set due to the quality of the synchrotron radiation and are obtained in existing wigglers. The rms peak field variation for the DORIS wigglers is below 1%, as is the period length deviation [Pflb]. Thus one would not expect any influence on the beam dynamics due to periodicity errors.

4.3.2 Pole Width

A critical parameter in the design of a wiggler is the width of the magnet pole. The choice of a certain width is deducted by the field strength to be obtained and by the beam dynamics. A rule of thumb in storage ring dipole design is that the field variance

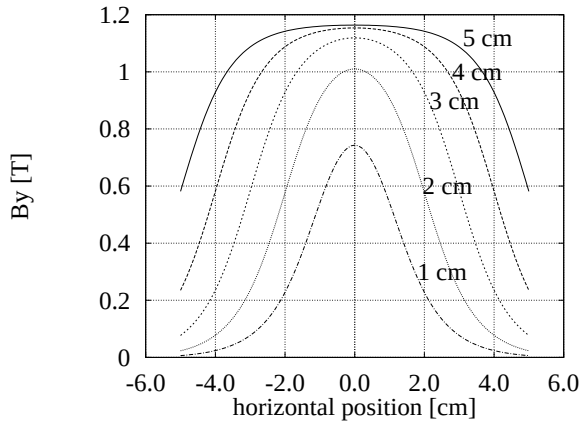

Figure 4.4: *Field profile of the vertical field of one wiggler pole with the half pole width varying from 5cm to 1cm (corresponding to 24 – 5 σ_{beam})*

in the 'good field' region should not be bigger then $1.0 \cdot 10^{-4} \cdot B_{dipole}$, i.e 0.01% of the main field. This does not hold for wiggler magnets, because the periodicity of the field will cancel most of the disturbing effects of a horizontal field gradient within one period. To investigate how small the pole width may be, numerical generating functions for the model wiggler described in chapter 2.4 have been calculated for different pole width. The field is characterized by the peak on-axis field B_{max} and the relative field decrease $\frac{\Delta B_y}{B_{y,max.}}$ at a horizontal position corresponding to $10\,\sigma$ of the beam at the investigated position in DORIS. The field profile of one pole is plotted in figure 4.4 for the different pole width used. The horizontal and vertical acceptances have been calculated in arbitrary units, the results are shown in table 4.2. A first decrease of the acceptance is seen for a half

Table 4.2: *Acceptance for DORIS with a wiggler with different pole width inserted*

half pole width	$B_{y,max.}$	$\frac{\Delta B_y}{B_{y,max.}}$ at 10 σ	acceptance in arbitrary units	
$[\sigma]$	[T]	%	horizontal	vertical
24	1.16	1.7	1.0	1.0
19	1.15	6.1	1.0	1.0
14	1.12	19.6	0.85	0.88
9.5	1.01	46.5	0.71	0.88
5	0.75	72.0	0.71	0.88

pole width between 14 and 19 σ_{beam}, but even a half pole width of 5 σ_{beam}, corresponding to a $\frac{\Delta B_y}{B_{y,max.}}$ of 72%, leads only to a 30% reduction of the horizontal acceptance.

The effect of the finite pole width becomes smaller if the wiggler period becomes shorter or the phase advance per pole becomes smaller. A decreasing gap leads to a shifting of the horizontal field decrease to the outer regions of the wiggler (see figure 2.4). Thus the needed pole width scales as:

$$\text{polewidth} \sim \frac{\lambda}{\beta} \cdot \text{gap}$$

whereby the functional dependence on the gap and period length can be more complicated due to constructional details of the wiggler.

This investigation was done for a wiggler with a rather large period (14cm) and a large phase advance per period. A half pole width of $20\,\sigma_{beam}$ ensures that there is no influence on the beam due to the finite width of the poles in this case. No closed orbit errors have been included because they are only in the order of $1\,\sigma_{beam}$, thus not having a big effect for a pole width of around $20\,\sigma_{beam}$.

4.3.3 Multipole Errors

As stated in chapter 2.6, the multipole representation of the measured field integrals is an easy way to parameterize the magnetic field errors of a wiggler. We will investigate in the following, if the multipole representation is a sufficient description of the field errors from the beam dynamics point of view. The problem is clear: the field integrals are measured along straight lines while the overall effect on an electron passing through a wiggler consists out of all the magnetic fields along the wiggled electron path. The current sheet method gives the possibility to model fields which produce the measured field integrals, but in addition with all the information about the three dimensional fields which are seen by the electron.

The asymmetric wiggler with its large measured multipole error (see chapter 2.6) serves as an example again. The maximum stable amplitudes as well as the tune shift with amplitude have been calculated for three different models of the ASYH with varying multipole contents of the first field integral:

number of model	name of wiggler model	b_2 [T/m]	b_4 [T/m^3]	name of corresponding multipole lens
0	ASYH-0	≈ 0.0	≈ 0.0	
1	ASYH-1	4.6	4000	multipole-1
2	ASYH-2	20	18000	multipole-2

The calculations are performed with:

- The numerical generating function for the different models ASYH-0, ASYH-1 and ASYH-2 of the asymmetric wiggler.
- The numerical generating function for the ASYH-0 and a thin lens multipole kick of the same strength as the multipoles derived from the first field integrals.

The tune shift with horizontal closed orbit amplitude in the wiggler is shown in figure 4.5 for the ASYH-1 and the ASYH-0 plus multipole-1. The tune shifts are in perfect agreement in the inner parts of the wiggler. They start to differ at amplitudes of $\approx$ 25mm. The good field region for the ASYH has been limited to 25mm in the model as well as in reality. Thus it is not surprising that the descriptions differ beyond this limit.

The area of stable amplitudes is shown in figure 4.6. The stable areas are similar for the cases ASYH-0 plus multipole lenses and the generating functions derived from the ASYH-1, respectively ASYH-2 model. The maximum stable horizontal amplitude is decreased down to 3.5mm for case ASYH-2, which would be less than the needed

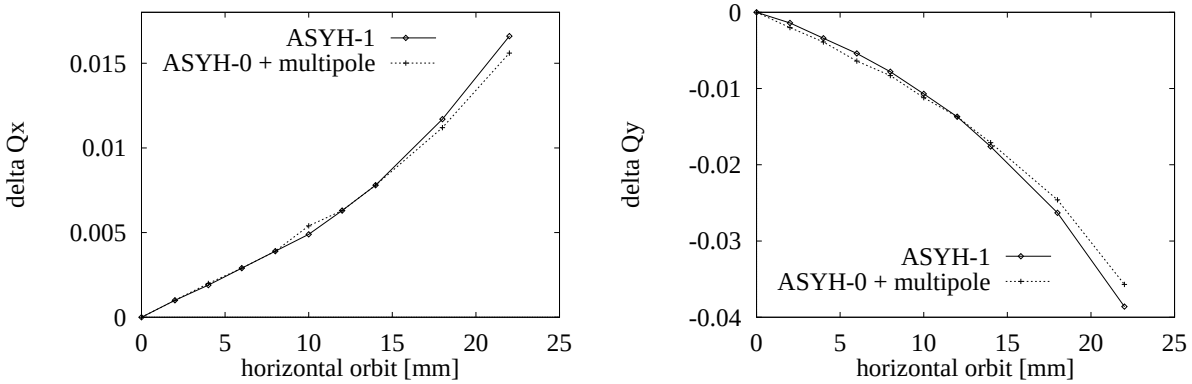

Figure 4.5: *Horizontal (left) and vertical (right) tune shift versus horizontal closed orbit amplitude within the wiggler.*
dashed line: model of the asymmetric wiggler with no multipole content of the first field integral and a multipole lens with the multipole strength $b_2 = 4.6T/m$, $b_4 = 4000T/m^3$, *i.e ASYH-0 and multipole-1*
solid line: model of the asymmetric wiggler with the multipole content $b_2 = 4.6T/m$, $b_4 = 4000T/m^3$ *of the first field integral, i.e. ASYH-1*

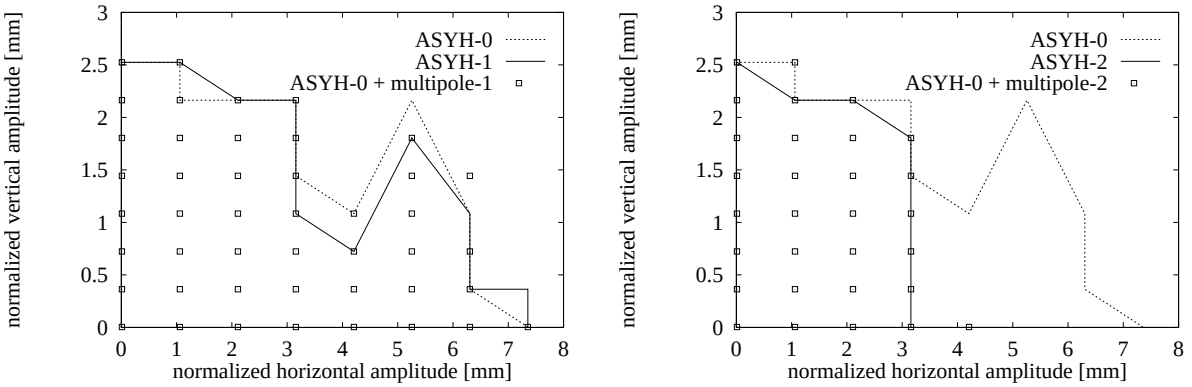

Figure 4.6: *Normalized stable amplitudes for model 1 (left) and model 2 (right). The envelope of the stable area for the ASYH-0 is plotted as dashed line, the envelope of the stable area for the ASYH-1 respectively ASYH-2 as solid line while the stable amplitudes for the ASYH-0 and appropriate multipole lenses (multipole-1 respectively multipole-2) are plotted as squares.*

acceptance of DORIS. ASYH-1 does not reduce the dynamic acceptance and would have been accepted from the storage ring.

From these investigations it follows, that the multipole expansion within the good field region is a sufficient tool to describe the tolerable magnetic field errors of the ASYH.

This investigation does not take into account a longitudinal variation of the field error, i.e. a first field integral which is zero or small at the end of the wiggler but has large values somewhere before. The field errors of the asymmetric wiggler are distributed uniformly along the longitudinal axis, which means that every single wiggler period contributes equally to the first field integral. A criteria for the longitudinal evolution of the first field integral may be the requirement that the field integral of one wiggler

period should not be larger than the acceptable value for the whole wiggler divided by the number of periods. This may set too rigorous bounds for the one period field integrals, because the cancelation of field errors from one period to the other is not taken into account.

Considering now the case of a field error at the beginning and end of the device with same strength but opposite sign. This will give a zero first field integral but can have a significant effect on the beam dynamics. A good criteria for this is the second field integral (2.17). It can be simulated by applying two multipole kicks I_1 and I_2 at the beginning and end of the wiggler, which have to fulfill the condition:

$$I_1 = I^{(2)}/L \qquad I_2 = -I^{(2)}/L \tag{4.2}$$

where $I^{(2)}$ is the second field integral and L the wiggler length. More complicated longitudinal distributions of field errors can be handled by demanding that the second field integral after at least one wiggler period should not be bigger than the values obtained by investigations with the kicks (4.2).

Limits for field errors of the DORIS wigglers have been calculated for the multipole contents of the first field integrals. They are given in table 4.3. The criteria for the b_2, b_4 components have been obtained by tracking calculations with the demand for no reduction in dynamic acceptance. The criteria for the dipole and quadrupole field errors are set by tolerances for closed orbit shifts and additional focusing or coupling. The b_3 component was set to be smaller than the pseudo-octupole of a DORIS X-WIG. It could also be determined by tracking calculations.

The DORIS wigglers and undulators fulfill most of the criteria given above. The first field integrals of one wiggler period are below the values given in table 4.3 divided by the number of periods, thus ensuring that there are no localized field errors bigger than the limits set by the multipole contents of the overall first field integrals.

Exceptions from these limits are discussed in chapter 5. These exceptions are for instance the dipole components of the HARWI2 and ASYH and the multipole components of the ASYH, as introduced already in this chapter.

Table 4.3: *Upper limits of the field error multipoles of the DORIS wigglers and undulators*

Multipole coefficient	Value	Criteria
b_0	$2.0 \cdot 10^{-4}$ Tm	Δclosed orbit $< 1/10\sigma_x$
a_0	$5.0 \cdot 10^{-5}$ Tm	Δclosed orbit $< 1/10\sigma_y$
b_1	$4.0 \cdot 10^{-2}$ T	$\Delta Q < \Delta Q_{intrinsic}$
a_1	$3.0 \cdot 10^{-3}$ T	additional coupling $< .1\%$
b_2	2.0T/m	dynamic acceptance
b_3	$300\mathrm{T/m}^2$	$<$ pseudo octupole
b_4	$7500\mathrm{T/m}^3$	dynamic acceptance

4.4 Tracking Studies for DORIS III

4.4.1 Resonances

The upper figure 4.7 shows a tune scan without (left) and with[b] (right) wigglers. Plotted is the number of stable turns versus the horizontal and vertical tune. The maximum number of turns is 512. The initial amplitudes are chosen in the way described in chapter 4.1, i.e corresponding to that aperture which gives a lifetime of 1 hour. The wigglers are simulated with the analytic generating function from [BW90] which takes into account all intrinsic nonlinear effects but no field errors. The influence of the longitudinal motion is modeled by synchrotron oscillations with a tune of $Q_s = 0.05$ and a starting amplitude of $\frac{\Delta p}{p} = 0.005$ which is equivalent to ≈ 5 longitudinal standard deviations. The sextupoles have been set to their usual values, i.e. the two families in the arcs are tuned to give a chromaticity of ≈ 1. Closed orbit and magnet positioning errors have been simulated by displacing the nonlinear elements randomly with a rms-deviation from the ideal position of 2mm in the horizontal and 1mm in the vertical plane. This corresponds to typical closed orbit values in the real machine. The resonances are named by the coefficients (n_x, n_y, n_s) of the resonance condition $n_x Q_x + n_y Q_y + n_s Q_s = n$.

The dominance of the (1,-1,0) resonance and its first satellite (1,-1,1) is clearly visible. Furthermore are excited the (2,2,0), the second satellite to the integer (1,0,-2) and a third order resonance (1,2,0). The wigglers have only a minor influence on the resonances. The resonances seem to be slightly broadened, but no new resonances occur when wigglers are introduced. This situation changes when errors are introduced as thin multipole lenses together with the wigglers. The multipole strengths are Gaussian distributed with one standard deviation corresponding to the values given in table 4.3. A tune scan with these parameters is plotted in the lower left figure 4.7. The free tune area decreases considerably. A proper choice of the working point becomes very difficult. The sole free area is around $Q_x = 7.17$, $Q_y = 4.28$, this is close to the operating working point of DORIS. To show the influence of the synchro-betatron resonances, the results of a tune scan with the same parameters but no synchrotron oscillations are shown in the right figure 4.7. Most of the resonances which are observable in the presence of synchrotron oscillations vanish. Some higher order betatron resonances are present due to the field error multipoles.

4.4.2 Dynamic Acceptance

After determining the disturbing structural resonances, the dynamic acceptance will be evaluated at selected tune points.

In a first step, the change of the tune with the initial amplitude is evaluated by tracking particles with step wise increasing the horizontal or vertical amplitudes and performing a Fourier transformation of the turn by turn particle coordinates. The results are shown in figures 4.8 and 4.9 for the cases only sextupoles, only wigglers, sextupoles and wigglers. It turns out, that the largest tune shift with amplitude is a variation of the vertical tune Q_y with the horizontal amplitude. This tune change is due

[b] In this case the XU at BW1, an X-WIG at BW2, BW4, BW6 and BW7, the HARWI2 at BW5, the XUV at BW3 and the HARWI at position W2 are inserted.

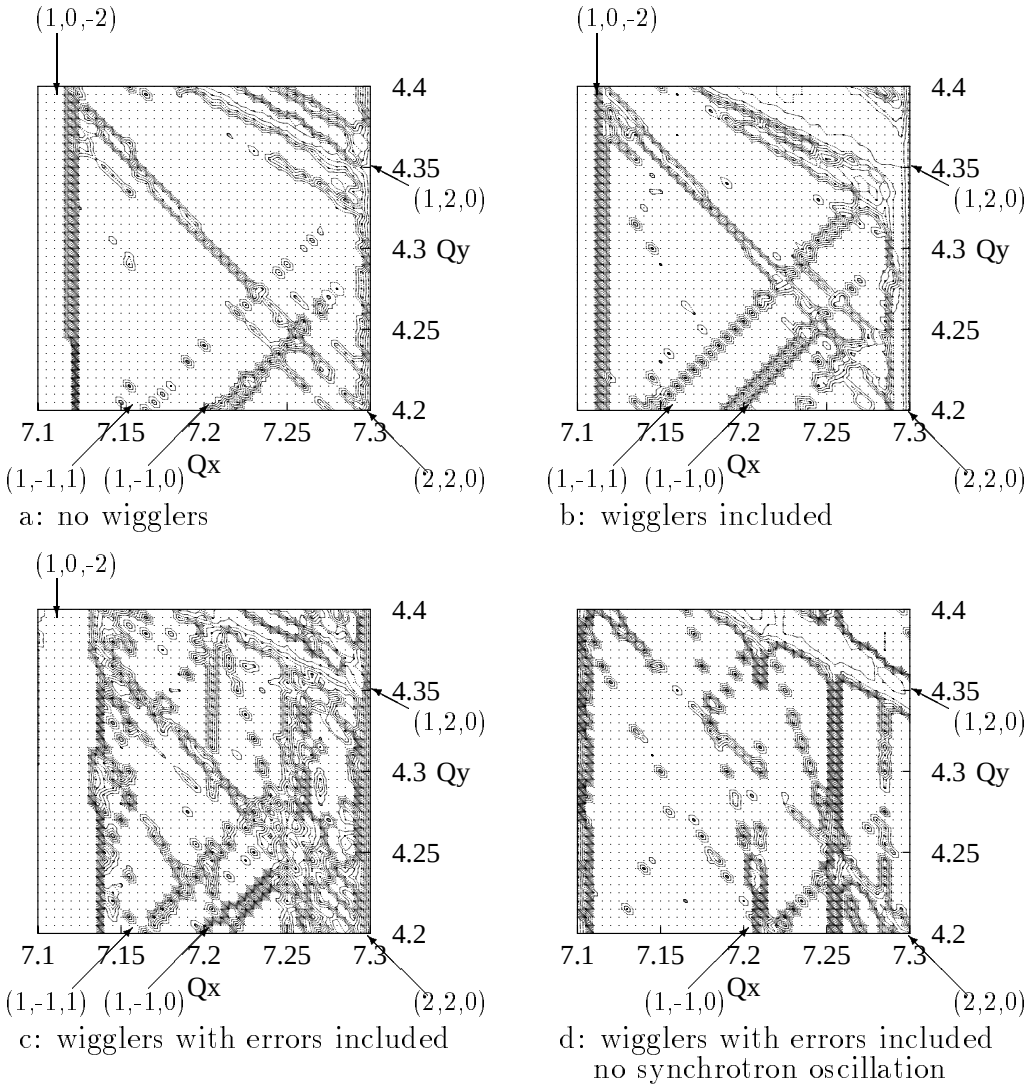

Figure 4.7: *Tune scans with the normalized transversal initial amplitudes* $x = 4.7mm$, $y = 0.65mm$ *and an initial impulse deviation of* $\frac{\Delta p}{p} = 0.005$ *for the cases a-c. The longitudinal tune is* $Q_s = 0.05$. *The sextupoles have been set to their usual values. The dark lines indicate the borders of regions with less than 512 stable turns. Resonances corresponding to these regions are marked with the coefficients* (n_x, n_y, n_s) *of the resonance condition (3.17). No wigglers have been inserted in case a, 8 ideal wigglers in a typical DORIS setup have been inserted in case b, and 8 wigglers with field errors are inserted in the cases c and d, where case d shows the situation without synchrotron oscillations. The field errors are simulated by multipole lenses with Gaussian distributed strength, where one standard deviation of the multipole strength corresponds to the values given in table 4.3.*

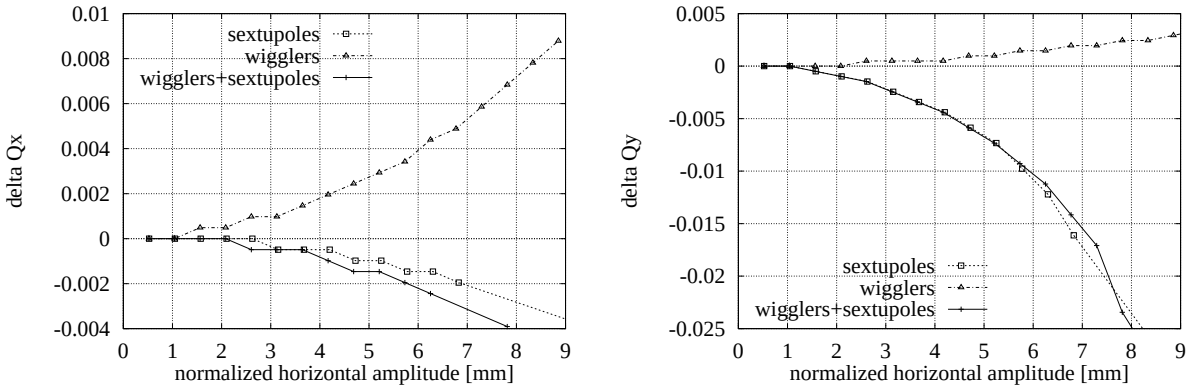

Figure 4.8: *Change of horizontal (left) and vertical (right) tunes versus initial horizontal amplitude.*

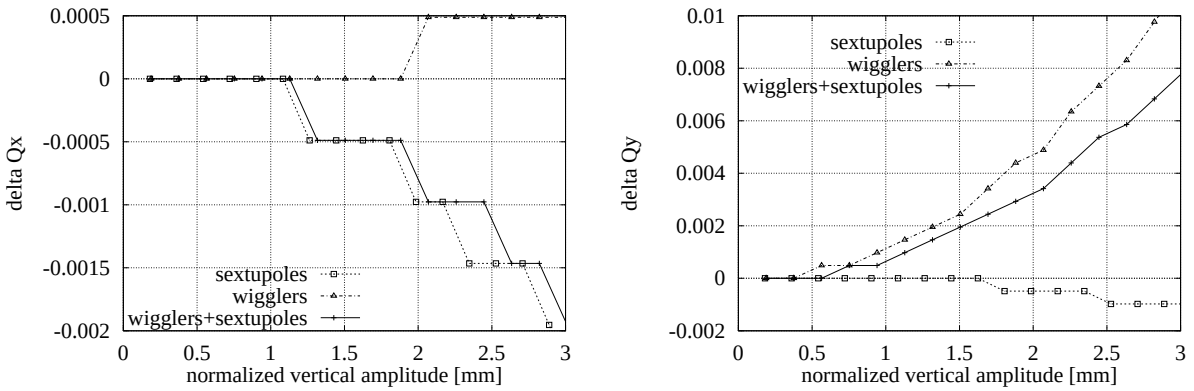

Figure 4.9: *Change of horizontal (left) and vertical (right) tunes versus initial vertical amplitude.*

to the sextupoles and not affected by the wigglers. The wigglers introduce an additional tune shift of the vertical tune with the vertical amplitude which has an opposite sign to the former one. These two effects may cancel each other partly, leading to a reduced detuning of large amplitude particles if the wigglers are closed. This effect helps to stabilize the dynamic acceptance in the presence of wigglers, because large amplitude particles do not need a large area in the tune diagram.

The dynamic acceptance for various sets of initial parameters will be discussed in the following. The calculations have been performed at a tune value far away from disturbing resonances. The sextupoles are tuned to give a chromaticity of ≈ 1, closed orbit errors are simulated by a random displacement of the nonlinear elements with a rms-value of 2mm horizontally and 1mm vertically. To calculate the momentum acceptance, the initial relative momentum deviation has been varied between 0.0 and 0.015. Results for the cases only sextupoles, wigglers[c] and sextupoles, wigglers with errors and sextupoles are shown in figure 4.10. The wiggler field errors are chosen to fit into the error limits given in table 4.3. A geometrical acceptance limitation restricts the maximum normalized amplitudes to 8.9mm in the horizontal and 2.7mm in the vertical

[c]The XU at BW1, an X-WIG at BW2, BW4, BW6 and BW7, the HARWI2 at BW5, the XUV at BW3 and the HARWI at position W2 are inserted.

plane. The number of tracked turns was 1024, several test runs with a larger number of turns (up to 10.000) have been performed to ensure the convergence of the stability limit for the chosen number of turns.

The intrinsic wiggler fields do not have a considerable effect on the dynamic acceptance. The on as well as the off momentum acceptance is unchanged. The slight decrease of the vertical acceptance is due to an increase of the $\beta-$function at the aperture limit position. The vertical acceptance is purely determined by the geometrical aperture. It increases to $\approx$ 4mm when the aperture limit is removed. The horizontal acceptance is clearly limited dynamically. It does not increase with the geometrical aperture limit removed. The dynamic acceptance is dominated by the sextupoles. Investigations have been performed to increase the dynamic acceptance by varying the sextupole distribution in DORIS. No significant improvements could be found due to the limited potentialities of the DORIS III lattice.

The introduction of field errors decreases the horizontal on momentum acceptance slightly. The off momentum acceptance is changed much stronger. Without errors, the acceptance is sufficient for particles with a relative impulse deviation of up to 1% and breaks down for $\frac{\Delta p}{p} = 1.5\%$. With errors, this limit is reached at a value of 1% impulse deviation, the acceptance for particles with $\frac{\Delta p}{p} = 0.5\%$ is strongly reduced. Thus we would expect a decrease of the horizontal dynamic acceptance due to the field errors of the wigglers if they are as big as assumed in table 4.3.

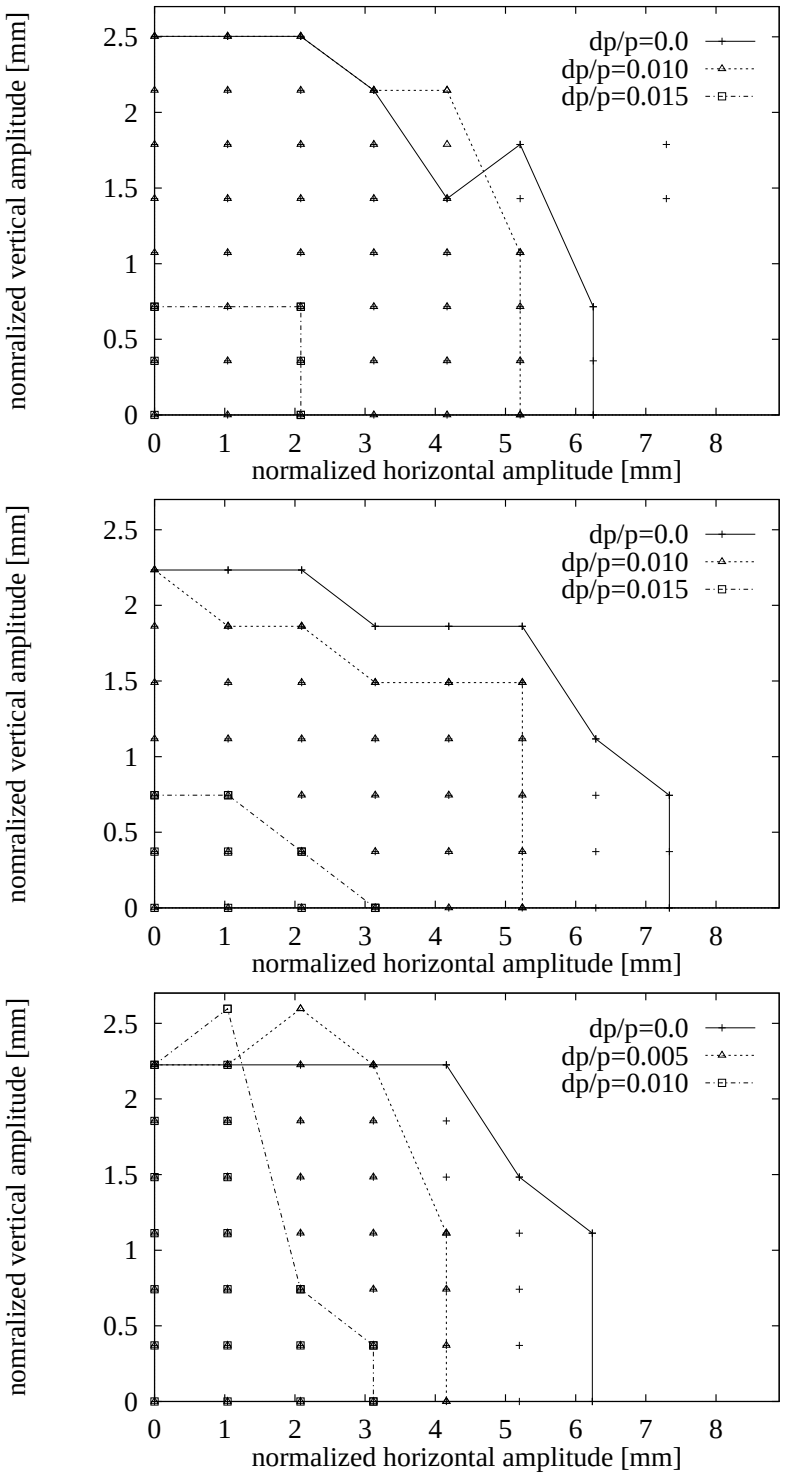

Figure 4.10: *Normalized stable initial amplitudes for the cases only sextupoles (upper), wigglers and sextupoles (middle), wigglers with errors and sextupoles (lower). The linear tunes are* $Q_x = 7.171,\ Q_y = 4.283,\ Q_s = 0.044$. *The initial relative impulse deviation is* $\frac{\Delta p}{p} = 0.0,\ 0.010,\ 0.015$ *for the upper two figures and* $\frac{\Delta p}{p} = 0.0,\ 0.005,\ 0.010$ *for the lower figure. The geometric aperture limitation corresponds to the boundaries of the plots, i.e* $2.7mm$ *vertically and* $8.9mm$ *horizontally.*

5 Measurements of Wiggler Effects on Beam Characteristics

We will now present measurements of most of the characteristics of a stored particle beam in the presence of wigglers and compare them with the theoretical and numerical results obtained before. Most of the measurements have been done at DESY's synchrotron radiation source DORIS III.

The Advanced Light Source (ALS) at the LBL in Berkeley provides the opportunity to study undulator effects at a modern third generation light source with all the features such as high lattice symmetry, strong sextupoles, vanishing dispersion etc.. A measurement of resonance excitation due to an undulator will be presented.

5.1 Linear Effects

5.1.1 Intrinsic Linear Focusing

Theoretical Basis

The linear focusing term in (3.20) causes a variation of the focusing distribution in the storage ring, leading to a different tune value and a modification of the β-function. Given a quadrupole strength $g(s)$, the resulting tune shift becomes [CS58]:

$$\Delta Q = \frac{1}{4\pi}\int_s^{s+L} \beta(s)g(s)ds \quad . \tag{5.1}$$

Together with (3.21), the tune shift due to a wiggler is:

$$\Delta Q_\mu = \frac{1}{4\pi}\beta\,\frac{1}{2}\frac{k_\mu^2}{\rho^2 k^2}\#_{of periods}\lambda \tag{5.2}$$

where λ is the period length of the wiggler, k the wave number and k_μ the horizontal or vertical field parameter as defined in equation (2.8). μ stands for the horizontal x or vertical y coordinate respectively. The bending radius ρ is defined by the maximum vertical on-axis field, thus the B_1 component of a sinusoidal wiggler. This results in a quadratic dependence of the tune shift on the vertical magnetic field amplitude.

In the presence of higher harmonics, the term $\frac{1}{2\rho^2}$ has to be calculated as follows:

$$\frac{1}{2\rho^2} = \frac{1}{2}\frac{e}{p_0}\sum_n B_n^2$$

and for measured fields:

$$\frac{1}{2\rho^2} = \frac{e}{p_0}\frac{1}{\lambda}\int_z^{z+\lambda} B_{meas}^2 dz \quad .$$

Measurements

The tune shift due to the different wigglers at their various locations has been calculated and measured with respect to the wiggler gap, which is equivalent to a variation of the magnetic field. Figure 5.1 shows the tune shift versus the measured integral of the squared field $\int_0^{L_{wiggler}} B_{meas.}^2 dz$.

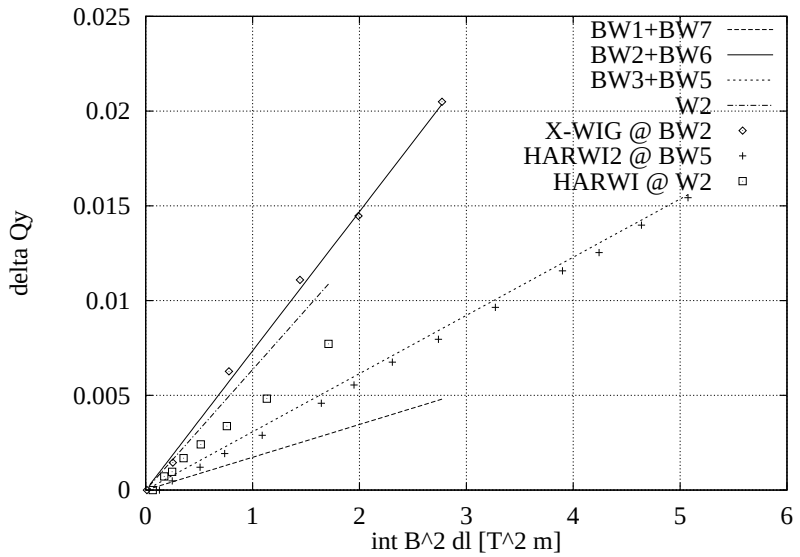

Figure 5.1: *Vertical tune shift 'delta Qy' versus integral of the squared field* $\int_0^{L_{wiggler}} B_{meas.}^2 dz$ *of different wigglers at varying locations for the DORIS optic 'BTH1'. The lines correspond to theoretical calculated tune shifts at the different locations, while the single symbols are measurements of different wigglers as indicated in the figure.*

Discussion

The tune shifts calculated with the theoretical β-functions agree in the cases HARWI2 @ BW5 and X-WIG @ BW2 very well with the measured values, which is both a measure of the β-function at the wiggler locations and the integrals of the squared fields. The maximum measured β-distortion due to magnet imperfections and closed orbit is $\approx 30\%$. The tune shift measurement proves that there is no additional quadrupole component due to field errors in these wigglers above 30% of the intrinsic focusing. Discrepancies between the theoretically predicted and measured tune shifts have been observed in the order of $\Delta Q \approx 0.002$ for all wigglers, which confirms that the quadrupole components of the field errors are well within the tolerances. The difference for the HARWI indicates a β-distortion of $\approx 30\%$ which is in agreement with measurements of the β-function.

The tune shift is corrected with the help of all ring quadrupoles in a way that the optical functions stay constant at selected locations (for example at the injection elements

and the old interaction regions). This correction scheme leads to a β-variation in addition to the spurious β-beat due to magnet imperfections and closed orbit distortions. The rms-value of this additional β-variation is:

$$\left(\frac{\Delta\beta_y}{\beta_y}\right)_{rms} = 10\% \quad .$$

In appendix C the theoretical variation of the β-function at the various wiggler locations is listed. This β-variation is not corrected. It is very difficult to find a practicable correction scheme because there are no dedicated quadrupole doublets around the wiggler straight sections.

5.1.2 Closed Orbit Distortion due to Field Errors

Theoretical Basis

The linear effects due to wiggler field errors are best described by using the first two terms of the multipole expansion of the measured field integrals (2.16). The b_1 (quadrupole) term adds an additional focusing to the one described in the previous chapter. The skew quadrupole term a_1 couples the two transversal motions, leading to an enlargement of the vertical beam size in an electron storage ring [WR88].

From the synchrotron radiation users point of view, the most disturbing effect of a wiggler is its influence on the closed orbit, caused by the dipole terms a_0, b_0 of the first field integral or by the $a_0^{(2)}$, $b_0^{(2)}$ of the second field integral. The former leads to an additional kick

$$\begin{aligned} \Delta x' &= \frac{1}{\rho_x} L_{wiggler} = \frac{e}{p_0} b_0 \\ \Delta y' &= \frac{1}{\rho_y} L_{wiggler} = \frac{e}{p_0} a_0 \ , \end{aligned} \tag{5.3}$$

while the latter introduces a shift of the closed orbit displacement of the amount

$$\begin{aligned} \Delta x &= \frac{e}{p_0} b_0^{(2)} \\ \Delta y &= \frac{e}{p_0} a_0^{(2)} \end{aligned} \tag{5.4}$$

between entrance and exit of the wiggler, both leading to a new closed orbit in the storage ring. The closed orbit under the influence of a dipole error is [CS58] (μ stands for x or y respectively and the optical functions β, ϕ and Q have to be taken in the corresponding plane):

$$\mu_{cl.o.}(s) = \frac{\sqrt{\beta(s)}}{2\sin\pi Q} \int_s^{s+L} \frac{1}{\rho_\mu(t)} \sqrt{\beta(t)} \cos(|\phi(t) - \phi(s)| - \pi Q)\, dt \tag{5.5}$$

where we can substitute (5.3) directly.

Situation (5.4) is more complicated. We can introduce a displacement $\Delta\mu$ by applying two kicks $\Delta\mu_1'$ and $\Delta\mu_2'$ at the beginning and the end of the wiggler, which have to

fulfill the following conditions to ensure a displacement but no remaining slope of the particle path after the end of the wiggler:

$$\begin{aligned} \Delta\mu_1' &= \frac{\Delta\mu}{\sqrt{\beta_2\beta_1}\sin(\Delta\phi)} \\ \Delta\mu_2' &= -\Delta\mu_1'\sqrt{\frac{\beta_1}{\beta_2}}\left(\cos(\Delta\phi) - \alpha\sin(\Delta\phi)\right) \end{aligned}$$

with $\Delta\phi = \phi_2 - \phi_1$.
If we put in these equations in (5.5), we get for the closed orbit outside the wiggler (with the assumption that $\Delta\phi \ll 1$, i.e. the phase advance over the wiggler length is small):

$$\mu_{cl.o.}(s) \approx \frac{\sqrt{\beta(s)}}{2\sin\pi Q\sqrt{\beta_2}}\sin(|\phi_1 - \phi(s)| - \pi Q)\Delta\mu \tag{5.6}$$

The rms-change of the closed orbit due to the second field integral is then:

$$(\Delta x_{cl.o.})_{rms} = \frac{\sqrt{<\beta>}}{2\sqrt{2}\sin\pi Q\sqrt{\beta_2}}\frac{e}{p_0}\, b_0^{(2)} \tag{5.7}$$

for the horizontal plane. The rms-change of the vertical closed orbit $(\Delta y_{cl.o.})_{rms}$ is obtained by exchanging $b_0^{(2)}$ with $a_0^{(2)}$. The rms-change caused by the first field integral is:

$$(\Delta x_{cl.o.})_{rms} = \frac{\sqrt{<\beta><\beta>_{wiggler}}}{2\sqrt{2}\sin\pi Q}\frac{e}{p_0}\, b_0 \tag{5.8}$$

for the horizontal plane. Again the change in the vertical orbit is obtained by exchanging b_0 with a_0. $<\beta>$ is the mean value of the β-function in the whole ring or in the wiggler, respectively. Thus the effect of an a_0, $b_0 \neq 0$ is larger at a location with a large β-function, while $a_0^{(2)}$, $b_0^{(2)} \neq 0$ has a stronger influence at locations with small β-functions.

Measurements and Discussion

The closed orbit shifts due to wigglers differ due to the quality, strength and location of the devices. At DORIS, the maximum closed orbit shifts for typical wigglers are in the order of $\approx$ 0.1mm in the vertical, and $\approx$ 0.2mm in the horizontal direction. The closed orbit can only be measured at the position monitors, thus the β-function has to be averaged over the monitor positions instead of the whole ring in (5.7) and (5.8). The corresponding DORIS III parameters are:

	horizontal	vertical
$<\beta>_{monitors}$	10.62	14.74
$<\beta>_{wiggler,max}$	22.0	22.0
$<\beta>_{wiggler,min}$	1.6	4.9

which allow an estimation of the maximum field integral values. This worst case estimate is given in table 5.1 together with typical maximum dipole components of the first and second field integral obtained from field measurements.

Table 5.1: *Estimated values of the dipole components of the first and second field integral together with values obtained from field measurements*

	first field integral [Tm]		second field integral [Tm^2]	
	estimate	field measurement	estimate	field measurement
vertical field (b_0)	$1.0 \cdot 10^{-3}$	$1.0 \cdot 10^{-3}$	$6.0 \cdot 10^{-3}$	$7.0 \cdot 10^{-3}$
horizontal field (a_0)	$0.36 \cdot 10^{-3}$	$0.5 \cdot 10^{-3}$	$3.9 \cdot 10^{-3}$	$2.0 \cdot 10^{-3}$

Figure 5.2 shows the rms-change of the closed orbit due to the HARWI2. The predicted value, obtained with (5.7) and (5.8) from measurements of the vertical field integrals I_y, $I_y^{(2)}$ (figure 5.3) is also plotted in figure 5.2. The strong dependence on the gap is qualitatively in good agreement with the field measurements, while there are some quantitative discrepancies at larger gap values.

Some outstanding wigglers show much stronger influences on the closed orbit than described above. The asymmetric wiggler has a strong gap dependence of the field integrals. The influence of the first field integral has to be corrected by a correction coil wound onto the magnet structure. The final adjustment of the correction coil current as a function of the wiggler gap was done with the help of closed orbit measurements.

At some of the synchrotron radiation beam lines the closed orbit shifts can be corrected with the help of a position feedback system [Bre].

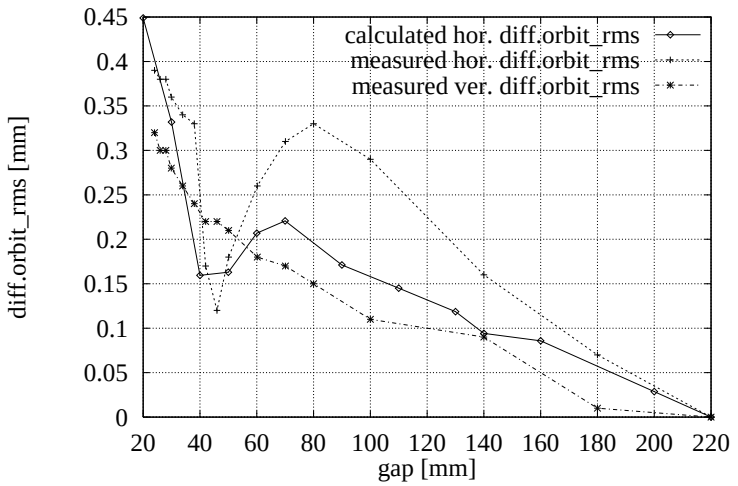

Figure 5.2: *Rms-change of the closed orbit due to the field errors of the HARWI2 versus wiggler gap.*
dashed line: measured horizontal orbit change
solid line: horizontal orbit calculated from the measured first and second field integrals (see figure 5.3) by (5.7) and (5.8)
dashed dotted line: measured vertical orbit change

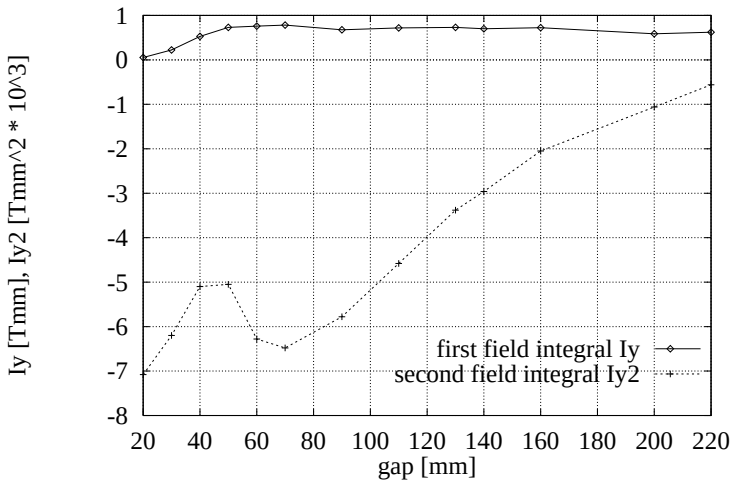

Figure 5.3: *Measured vertical field integrals of the HARWI2 versus wiggler gap. solid line: first field integral I_y corresponding to the dipole component b_0 dashed line: second field integral $I_y^{(2)}$ corresponding to $b_0^{(2)}$*

5.2 Nonlinear Tune Shift with Amplitude

Theoretical Basis

We have measured the nonlinear tune shift versus the closed orbit amplitude in a wiggler. Because of the high energy of DORIS and thus the relatively small nonlinear terms, a tune shift can hardly be seen when changing the orbit in the wiggler. The best positions for these measurements are those with high vertical β-functions.

Taking equation (5.1), which gives the dependence of the tune shift on an additional quadrupole gradient, we can estimate the nonlinear tune shift due to a wiggler by calculating the quadrupole gradient from the equations of motion (3.30):

$$g \equiv \frac{\partial f(y)}{\partial y} = -\frac{k_y^4}{\rho^2 k^2} y^2 - \frac{k_x^2}{2\rho^2} x^2$$

The horizontal tune shift can be calculated similarly.

Measurements and Discussion

The parameters of the X-WIG at position BW2 are:

k	$44.88\mathrm{m}^{-1}$
k_y	$46.35\mathrm{m}^{-1}$
$\frac{1}{\rho}$	$7.66 \cdot 10^{-2}\mathrm{m}^{-1}$
β_y	25.0m
$\lambda \cdot \#_{ofperiods}$	3.92m

yielding a nonlinear vertical tune shift depending on the vertical deviation y of the closed orbit from the wiggler axis:

$$\Delta Q_y = 105[\mathrm{m}^{-2}] \cdot y^2$$

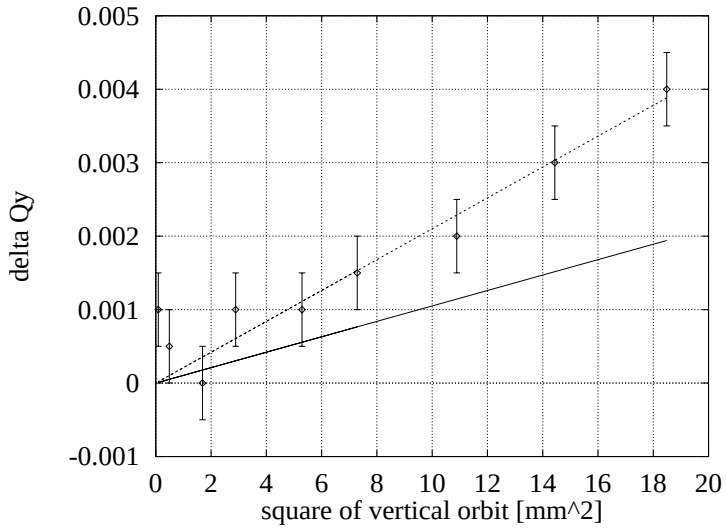

Figure 5.4: *Measured nonlinear tune shift versus the square of the vertical closed orbit inside the wiggler.*
diamonds: measured values
solid line: theoretical dependence $\Delta Q_y = 105[m^{-2}] \cdot y^2$
dashed line: fit with $\Delta Q_y = 210[m^{-2}] \cdot y^2$

Figure 5.4 shows the corresponding measurement. The values are derived by steering the closed orbit approximately parallel inside the wiggler with the help of a closed bump involving 4 steering magnets. This guarantees an unchanged orbit outside the bump, thus no other nonlinear elements are involved. The tune shift is plotted versus the square of the closed orbit, assuming a quadratic dependence on the closed orbit. The solid line gives the theoretically predicted value, while the dashed line is the best linear fit which gives a quadratic dependence of $\Delta Q_y = 210[\mathrm{m}^{-2}] \cdot y^2$, twice as large as the predicted one. The values, which have been calculated with a transfer map based on a more realistic field model using the current sheet method, differ only slightly from the theoretically predicted values.

Unfortunately there was no field measurement data available to study the influence of field errors on the measured nonlinear tune shift. The remaining discrepancies can be explained by an octupole term of the field integral in the order of $b_3 = 2.6 \cdot 10^2 \mathrm{Tm}^{-2}$, a rather small value which is well below the tolerance limit for this field component (see table 4.3).

5.3 Resonances

Experimental Method

An important method of investigating the nonlinear effects of wigglers is the observation of the excitation of resonances. As one method of observing resonances we have measured the dependence of the lifetime of the stored beam on the tunes. As stated before, DORIS III was operated in two different regimes of the tune diagram, one with the vertical tune below an integer, the other with the vertical tune above an integer. This

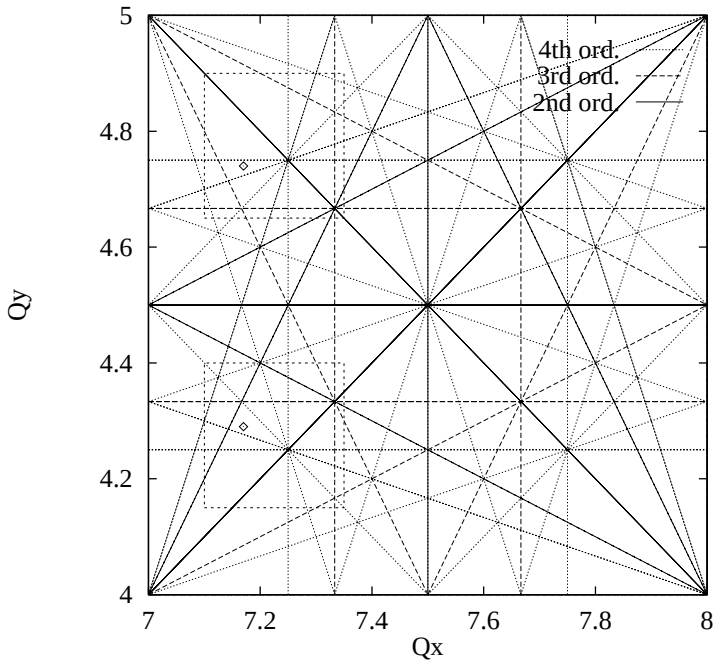

Figure 5.5: *Tune diagram with all betatron resonances up to 4th order. The normal working points are marked with diamonds, the boxes around the working points denote the investigated tune areas.*

allowed the observation of different resonances. Figure 5.5 illustrates the two regions in the tune diagram, with the investigated areas surrounded by a box. The tune diagram shows all betatron resonances up to fourth order.

The tune scans were normally performed with a low electron current, thus avoiding effects due to higher currents such as large coherent tune shifts, lifetime reduction due to the capture of ionized particles [Kau94] or instabilities. Lifetime variations above a limit of 4 hours have not been considered, because the time needed to measure the lifetime increases with increasing lifetime. The tune was varied with the help of all quadrupoles, keeping optical functions constant at selected positions in the ring. Within a tune change of $\Delta Q = \pm 0.2$ the disturbance of the linear optics is tolerable.

5.3.1 Resonances in the Vicinity of $Q_y = 4.75$

Measurements

We will first discuss the resonances observed in the upper left quadrant of figure 5.5. The results of tune scans along a straight line in the Q_y-direction are presented in figure 5.6. The scans are performed without a wiggler and with an X-WIG closed to its minimum gap at position BW6. The horizontal tune was $Q_x = 7.173$ and the longitudinal tune was $Q_s = 0.051$. The resonances which cause the decrease of lifetime are named with their coefficients (n_x, n_y, n_s) of the resonance condition $n_x Q_x + n_y Q_y + n_s Q_s = n$. They were identified by changing the tunes slightly in the vicinity of an observed decrease in lifetime. The ratio of the tune changes to decrease the lifetime by the same amount gives the coefficients named above. Without the wiggler, the sum-resonance (1,1,0) and

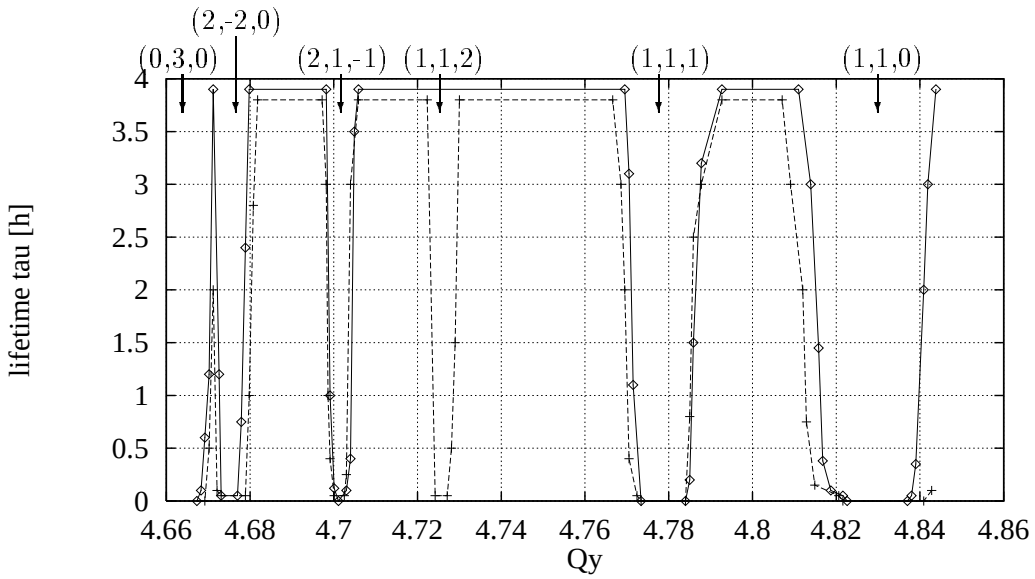

Figure 5.6: *Lifetime versus vertical tune by keeping $Q_x = 7.173$ and $Q_s = 0.051$ constant.*
Solid line: All wigglers at their maximum gap (i.e. off)
Dashed line: X-WIG closed at position BW6

its first synchrotron sideband (1,1,1) are excited, together with the vertical third integer (0,3,0) and the difference resonance (2,-2,0). Somehow surprising is the appearance of the satellite (2,1,-1). In addition the wiggler drives the second synchrotron sideband of the sum-resonance (1,1,2) and broadens slightly the other resonances.

Closing all wigglers amplifies these effects. Figure 5.7 shows a summary of tune scans performed with all wigglers[a] closed to their minimum gap. The dashed lines in the plot denote sections of the tune scans with lifetimes > 1 hour. One clearly sees the appearance of the resonances mentioned above. In addition, the resonance (1,-3,0) is visible. On all resonances, the lifetime decreases to a few seconds and most or all of the beam is lost when crossing the resonance.

The dependence of lifetime on tune is extremely sensitive to closed orbit errors. Figure 5.8 shows a tune scan with horizontal constant tune where the vertical closed orbit in the wiggler was changed with the help of four steering coils to a value of $y_{cl.o} \approx 2$mm. The scan was performed with an X-WIG at position BW2 closed, respectively open. In comparison to figure 5.6 many more resonances are observed when the closed orbit is changed and the wiggler is closed. Not all of them have been identified. It is very difficult to find a satisfying working point.

Table 5.2 summarizes the resonances observed with and without wigglers. The resonance width is defined as the difference between those tune values on both sides of the resonance, where the lifetime τ decreases below 1 hour.

The width of the sum-resonance and its synchrotron sidebands without wigglers depends strongly on other machine parameters such as closed orbit, magnet alignment or beam current. After a realignment it increased in the 1993 run period nearly to the values obtained with closed wigglers.

[a]This means the XU at BW1, an X-WIG at BW2, BW4, BW6 and BW7, the XUV at BW3 and the HARWI at position W2.

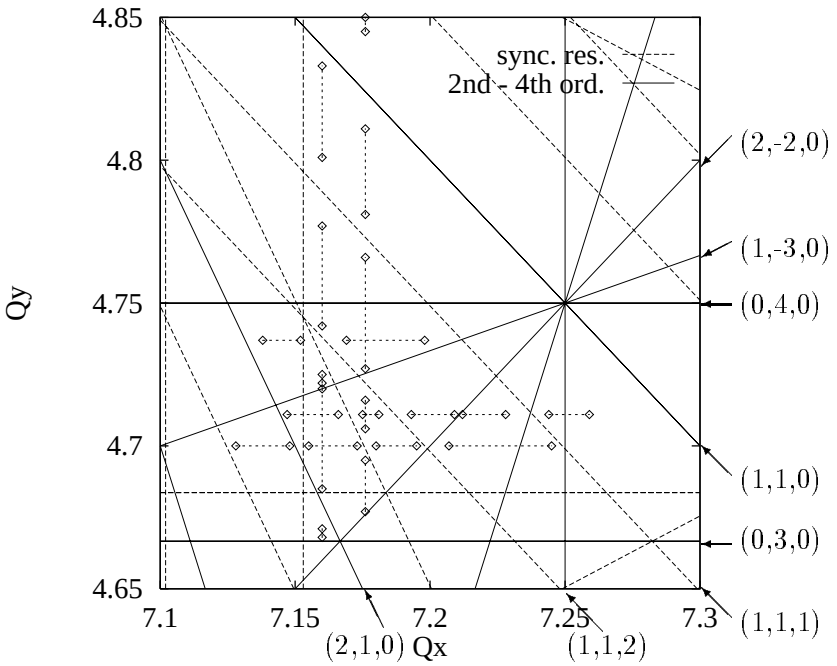

Figure 5.7: *Summary of tune scans with all wigglers closed. The solid lines are betatron resonances up to 4th order, the dashed lines are synchro-betatron resonances up to 4th order. The synchrotron tune was* $Q_s = 0.051$ *for all scans.*
The dashed lines with diamonds mark sections of the scans with lifetimes > 1 *hour.*

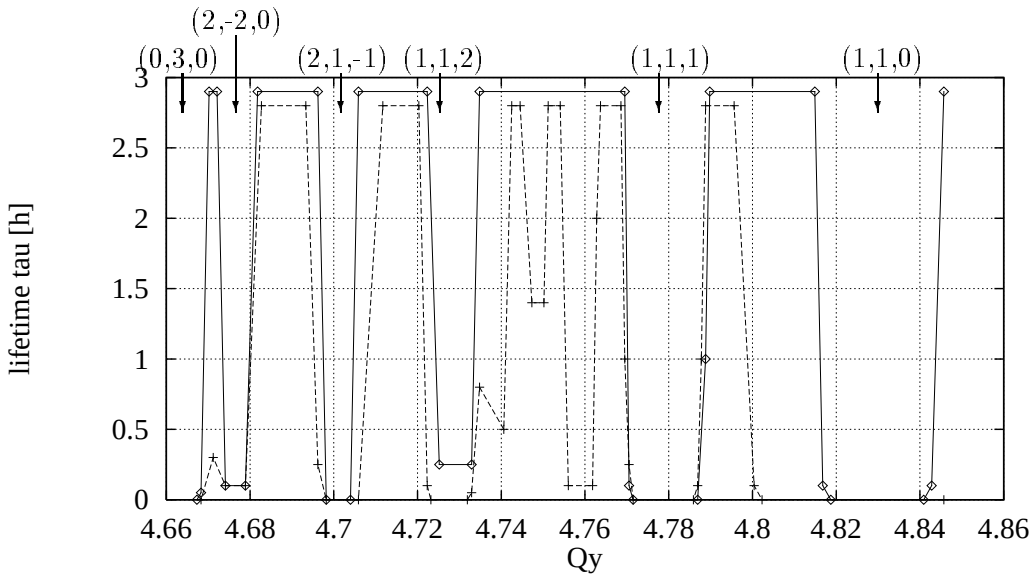

Figure 5.8: *Scan of the vertical tune by keeping* $Q_x = 7.173$ *and* $Q_s = 0.051$ *constant. The vertical orbit within the wiggler was changed to +2mm.*
Solid line: X-WIG closed to 60mm at position BW2, all other wigglers at their maximum gap
Dashed line: X-WIG closed to 30mm at position BW2

Table 5.2: *Measured width of resonances in the vicinity of the working point* $Q_x = 7.17$, $Q_y = 4.75$ *without and with wigglers*

order	resonance	resonance width	
	n_x, n_y, n_s	without wigglers	with wigglers [a]
2	$1, 1, 0$	$0.01 - 0.02$	$\approx .025$
3	$1, 1, 1$	$\approx .010$	$\approx .020$
	$2, 1, 0$	.004	.007
	$0, 3, 0$	$.004 - .01$	.006 - .01
4	$1, 1, 2$	0 - .010	.010 -.020
	$2, 1, -1$	.004	.007
	$2, -2, 0$	.005	.005 - .010
	$1, -3, 0$	0	.003
	$0, 4, 0$	0	.002[b]

[a]This means the XU at BW1, an X-WIG at BW2, BW4, BW6 and BW7, the XUV at BW3 and the HARWI at position W2.

[b]Only observed with bad vertical orbit.

5.3.2 Resonances in the Vicinity of $Q_y = 4.25$

Measurements

DORIS has been operated since 1994 with a working point in the lower left corner of figure 5.5. We have performed similar resonance measurements as above. Figure 5.9 summarize the results. The dominant role is played by the difference resonance (1,-1,0) and its first and second synchrotron sideband. The appearance of the synchro-betatron resonance (2,-1,1) together with the broadening of the (1,-1,2) leads to an extremely small working area in the tune diagram. At high currents, the tune has to stay within $\Delta Q = \pm 0.005$ for both transversal planes. A summary of the observed resonances is given in table 5.3.

Discussion

The most severe effect of wigglers on the resonance structure in the vicinity of the investigated working points is the excitation of the 4th order synchro-betatron resonances $(1, \pm 1, \pm 2)$ and $(2, \pm 1, \pm 1)$. The excitation of these resonances is predicted by the perturbation treatment of the equations of motion in a wiggler, as described in chapter 3.3. These resonances are only excited with a horizontal and vertical dispersion in the wiggler. The vertical dispersion in DORIS is due to the radiation shielding scheme of the former ARGUS experiment, which could be removed after the shut down of the experiment. This should decrease the excitation strength of these resonances. The extreme lifetime reductions at all the observed resonances is due to the extremely small vertical aperture of DORIS. Measurements of the vertical acceptance (chapter 5.5) give an acceptance of 2.5π mrad mm which has to be compared with a beam emittance of 0.016π mrad mm, assuming 4% coupling. Thus even a small increase of particle amplitudes leads to the

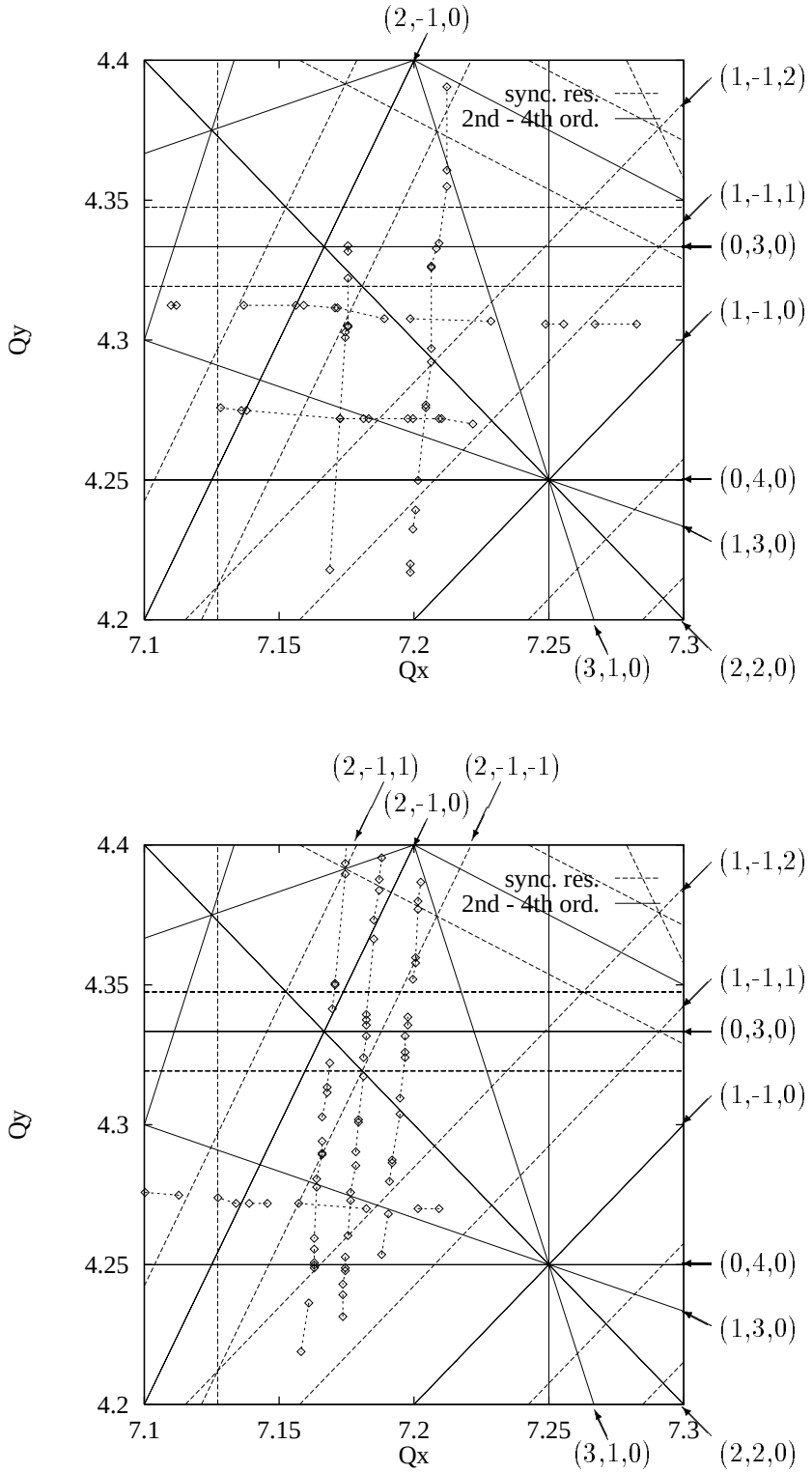

Figure 5.9: *Summary of tune scans with all wigglers open (upper) or closed*[a] *(lower). The solid lines are betatron resonances up to 4th order, the dashed lines are synchro-betatron resonances up to 4th order. The synchrotron tune was* $Q_s = 0.041$ *for all scans. The dashed lines with diamonds mark sections of the scans with lifetimes* > 1 *hour.*

[a]This means the XU at BW1, an X-WIG at BW2, BW4, BW6 and BW7, the XUV at BW3 and the HARWI at position W2 closed to their minimum gap.

Table 5.3: *Measured width of resonances in the vicinity of the working point* $Q_x = 7.17$, $Q_y = 4.25$ *without and with wigglers*

order	resonance n_x, n_y, n_s	resonance width without wigglers	with wigglers [a]
2	$1, -1, 0$	$\approx .015$	$\approx .025$
3	$1, -1, 1$	$\approx .010$	$\approx .020$
	$2, -1, 0$	.002	.005
	$0, 3, 0$	$.0 - .001$	.002
4	$1, -1, 2$	0	.010
	$2, -1, \pm 1$	.0	.005
	$2, 2, 0$	.005	.005–.010
	$1, 3, 0$	0	.002
	$0, 4, 0$	0	.002[b]
	$0, 3, \pm 1$	0	[c]

[a] This means the XU at BW1, an X-WIG at BW2, BW4, BW6 and BW7, the XUV at BW3 and the HARWI at position W2.

[b] Only observed with bad vertical orbit.

[c] Only observed at points where other resonances cross.

loss of these particles at the geometric aperture.

The comparison of tracking data and the measured resonances gives a somewhat mixed picture. The resonances dominating the storage ring without wigglers, i.e. the (1,-1,0), (1,-1,1) and (2,2,0) can clearly be identified in the tracking data (see figure 4.7). The excitation of the 4th order synchro-betatron resonances by the intrinsic wiggler fields is not deducible from figure 4.7. Nevertheless an analysis of the turn by turn tracking data shows a slight increase of the maximum vertical particle coordinate on the (1,-1,2) resonance, which may explain, together with the small measured acceptance, the observed lifetime decrease on this resonance.

By inserting typical wiggler field errors in the tracking, a wide variety of resonances appears (figure 4.7). The additional resonances observed when closing the wigglers may thus be driven by the wiggler field errors, leading again, together with the vertical aperture restriction, to the extreme lifetime reductions.

5.4 Beam Profiles

Experimental Method

One possible method of measuring beam profiles in DORIS is to move a scraper into the beam, thus reducing the free aperture and thereby the lifetime. By measuring scraper position and beam lifetime one gets information about the tails and center areas of the beam. The basic formulas, which describe the dependence of lifetime on the aperture are given in appendix B. The beam emittance can be evaluated by fitting a curve corresponding to (B.1) to the measured lifetimes for scraper positions close to the beam

center. This assumes a Gaussian distribution of particles in the core of the beam. With known β-functions and damping times, the emittance is the only fitting parameter. Thus these measurements give both information about the beam emittance and about the behavior of the tails of the distribution, which are far from being Gaussian.

To measure the Gaussian part of the distribution, one has to be closer to the beam center than $\approx 6\sigma$. The small vertical beam size makes the measurement difficult and inaccurate because of the positioning error of the scraper.

Measurements

Figure 5.10 shows a measurement of a horizontal and vertical beam profile. The scraper positions are corrected for the closed orbit and normalized to a β-function of 1m. In addition the theoretical curve for the quantum lifetime assuming a Gaussian distribution of the particles in the beam is fitted to the measured data.

The horizontal beam profile is not changed by the wigglers, as expected from theoretical investigations. In the equilibrium state the additional damping introduced by the wigglers is counterbalanced by the quantum excitation due to the dispersion in the wigglers.

The vertical emittance evaluated from the fitting of (B.1) to the lifetime data is slightly larger when closing all wigglers, but this increase is still within the error of the measurement.

The vertical beam profile is rather sensitive to other beam parameters, as shown in figure 5.11. In this measurement, in addition to closing one X-WIG the vertical orbit within this wiggler has been varied. There is no change in the beam profile as long as the wiggler is open. When closing the wiggler, the emittance increases by a factor of 2 and the beam tails are more strongly populated if the vertical closed orbit is varied by 2mm in the wiggler. The closed orbit is varied with 4 steering magnets in the vicinity of the wiggler. This ensures that the orbit is constant in all other nonlinear elements. The population of beam tails has also been observed in the vicinity of the (1,1,1) resonance,

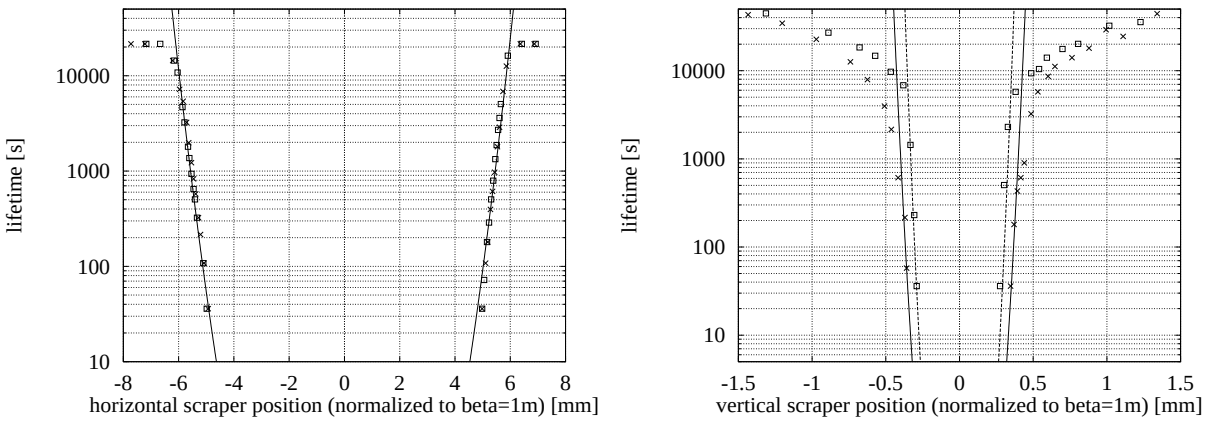

Figure 5.10: *Measured beam lifetime versus normalized horizontal (left) and vertical (right) scraper position for the cases without wigglers (×) and with wigglers (□). The lines are fits of the quantum lifetime function, assuming a Gaussian particle distribution, to the measurements in the inner part of the beam.*

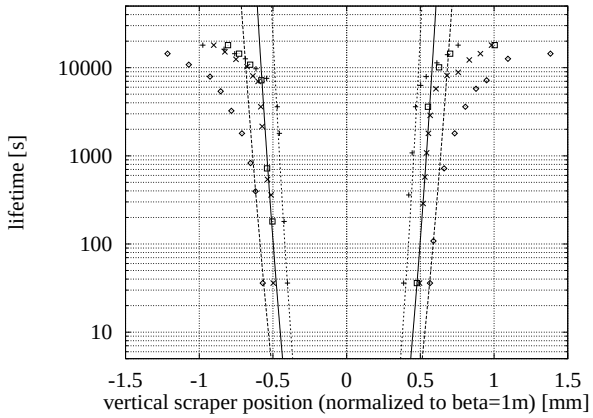

Figure 5.11: *Beam lifetime versus normalized vertical scraper position for the cases X-WIG opened/closed at BW2 and different closed orbits at the wiggler position.*
×: X-WIG open, vertical orbit 0 mm *+: X-WIG closed, vertical orbit 0 mm*
□: X-WIG open, vertical orbit 2 mm *◇: X-WIG closed, vertical orbit 2 mm*
The lines are fits of the quantum lifetime function, assuming a Gaussian particle distribution, to the measurements in the inner part of the beam.

with no dependency on the wiggler status [Dec94c].

Table 5.4 summarizes the beam profile measurements and gives the emittances, evaluated from the fitting of the quantum lifetime to the lifetime measurements with scraper positions close to the beam core.

Table 5.4: *Summary of emittances evaluated from lifetime measurements with scraper positions close to the beam core*

plane	wiggler status	ε [π mrad mm]	tails
horizontal	open	0.41 ± 0.1	
	all closed	0.41 ± 0.1	
vertical	open	$(3.4 \pm 4.0) \cdot 10^{-3}$	
	all closed	$(4.9 \pm 4.0) \cdot 10^{-3}$	enlarged
	open	$(9.0 \pm 4.0) \cdot 10^{-3}$	
	open + bump	$(9.0 \pm 4.0) \cdot 10^{-3}$	
	BW2 closed	$(6.4 \pm 4.0) \cdot 10^{-3}$	
	BW2 closed + bump	$(13.0 \pm 4.0) \cdot 10^{-3}$	enlarged

Discussion

The horizontal beam profile measurements are in good agreement with the theory. The vertical beam profiles show an increase of both the core emittance and the beam tails when wigglers are inserted. These increases are within the errors of the measurement and give only a hint of an effect of the wigglers. A change of other storage ring parameters such as the closed orbit could also produce these small effects. More detailed

measurements with a higher accuracy should be performed to investigate the vertical beam sizes versus different storage ring parameters.

The increase of the vertical beam size when passing a wiggler with a vertical closed orbit offset was investigated with single particle tracking. This has been done by observing the change of the ratio of the vertical and horizontal emittance during the tracking run. An increase of the vertical emittance could be observed at some working points close to sum resonances, while the emittance ratio does not change at other working points. The wiggler has only a minor effect on the emittance ratio. Further measurements should be done to ensure whether this is a fault of the model or an error of the measurement.

5.5 Acceptance

The acceptance of a storage ring is an important parameter which determines the beam lifetime. It is straightforward to distinguish between the geometric acceptance given by hardware limits in the storage ring and the dynamic acceptance which is the maximum possible stable amplitude of particles, determined by the nonlinear fields.

The installation of wigglers influences the geometric aperture due to the requirements of small vertical magnetic gaps and thus reduces the free vertical aperture. The nonlinear fields of a wiggler reduce the dynamical acceptance.

Experimental Method

The acceptance is measured with the help of a fast kicker magnet. With this the beam is kicked in one direction with increasing kick strength until the lifetime is distinctly reduced. This lifetime reduction is due to either the geometric or dynamic acceptance. This method can serve as a relative measurement of acceptance by comparing the kicker amplitudes at different storage ring parameter settings. To get a quantitative result, a pair of scrapers is used to reduce the lifetime even more by decreasing the geometrical aperture from both sides of the beam. These geometrical limits sc_{top} and sc_{bottom} correspond to the acceptance:

$$acceptance = \frac{\left(\frac{sc_{top} - sc_{bottom}}{2}\right)^2}{\beta} \quad .$$

Error sources for this measurement are a variation of the kicker amplitude and the error of the β-function at the scraper. The absolute value of the acceptance varies due to the scraper which was used, the date and the person who performed the measurement.

Measurements

The following table gives an average of all acceptance measurements:

	measured dynamic acceptance		calculated geometric acceptance
	no wigglers	with wigglers	of ideal machine
	[π mrad mm]		
horizontal	60 ± 10	40 ± 10	80
vertical	2.5 ± 0.5	2.5 ± 0.5	5

The horizontal acceptance is decreased with wigglers. This decrease has been observed even when only one X-WIG closed. The small vertical acceptance is unchanged.

Discussion

The vertical dynamic acceptance is not affected by the introduction of wigglers. It is defined by the geometric aperture, which is very small due to the narrow wiggler vacuum chambers and vertical closed orbit errors. Closed orbit and alignment errors reduce the vertical geometric aperture from the calculated 5.0π mrad mm of the ideal machine to the measured 2.5π mrad mm. The tracking calculations presented in chapter 4.4.2 also showed no decrease of the geometrical limited acceptance due to nonlinear dynamics effects.

The horizontal dynamic acceptance is slightly reduced when the wigglers are closed. Tracking calculations showed that this is not due to the intrinsic nonlinearities of the wigglers. The combination of wiggler fields and their errors is responsible for the slight reduction of the dynamic acceptance (see chapter 4.4.2). The acceptance was calculated from tracking data by determining the maximum stable horizontal phase space area. A reduction of the horizontal acceptance from $\approx 70\pi$ mrad mm down to $\approx 40 - 50\pi$ mrad mm can be observed when wigglers with typical field errors[b] are inserted in the tracking.

The dynamic acceptance with wigglers is large enough to provide satisfactory lifetimes.

5.6 Measurements in the Fringe Field

Experimental Method

Due to the finite width of the wiggler poles, the magnetic field depends on the horizontal position in the wiggler (see chapter 2). We have performed an experiment to investigate this effect. For this case, an X-WIG at position BW2 was shifted horizontally by 17mm to the inner side of the ring. By using horizontal orbit bumps it was possible to move the orbit within the wiggler between $0 - 30$ mm with respect to the wiggler axis. Figure 5.12 shows the vertical field obtained from the current sheet model together with the $10\sigma_x$ beam dimension drawn at the outermost position of the beam center with respect to the wiggler axis.

Measurements

We have observed a strong influence of the coupling resonance width on the horizontal beam position in the wiggler as shown in figure 5.13, where the width of the resonance (1,1,0) is plotted versus the horizontal position of the beam center with respect to the wiggler axis. The resonance width decreases when steering the closed orbit to the outer parts of the wiggler, and the width was increased by more than a factor of 2 when operating close to the axis of the wiggler. The other resonances remained unchanged.

[b] Multipole kicks with Gaussian distributed strength where one standard deviation corresponds to half of the strength given in table 4.3.

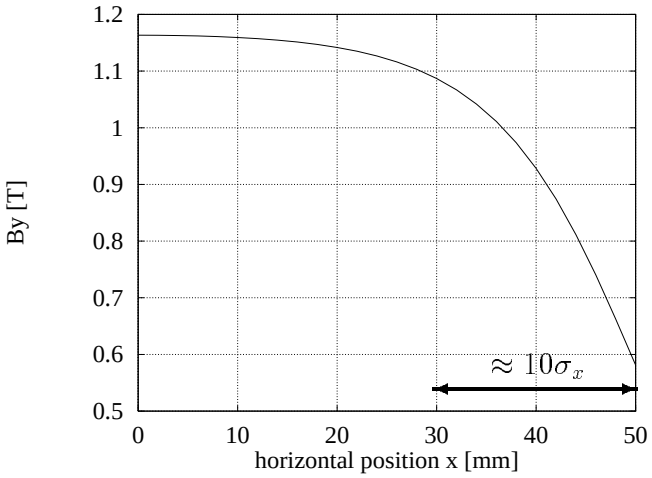

Figure 5.12: *Vertical field of an X-WIG pole versus the horizontal position, in addition the $10\sigma_x$ beam dimension is shown*

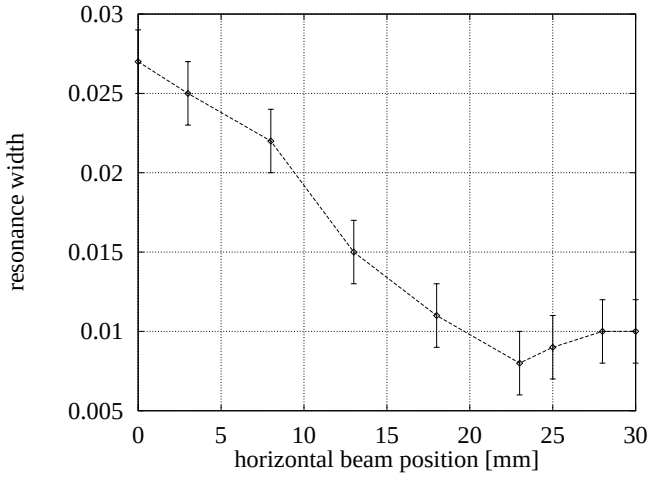

Figure 5.13: *Resonance width of the $Q_x + Q_y$ resonance versus horizontal closed orbit with respect to the wiggler axis*

The horizontal dynamic acceptance was slightly reduced by $10 - 20\%$, thus within the error of the measurement. The vertical acceptance remained unchanged.

Discussion

The influence on the sum resonance (1,1,0) indicates additional linear coupling when changing the horizontal beam position in the wiggler. The orbit bump which was used does not include other nonlinear elements like sextupoles. Furthermore, the variation of the closed orbit with the wiggler open showed no influence on the sum resonance. Thus the additional coupling is clearly produced by the wiggler. A numerical generating function of the X-WIG modeled with the current sheet method and a horizontal offset from the wiggler axis has been calculated (see chapter 3.6). Tracking calculations have been performed with this numerical generating function. An intrinsic coupling was

produced in the machine by displacing the sextupoles randomly. The resonance width of the (1,1,0) resonance has been evaluated through tune scans with particles started at initial transversal amplitudes corresponding to a lifetime of 1 hour (see chapter 4.1). The width of the resonance is defined by the closest pair of particles on both sides of the resonance which survive 1024 turns. The resonance width with no wiggler was ≈ 0.01 which remained unchanged when introducing the wiggler with no offsets. It increased to ≈ 0.015 when the numerical generating function with both a horizontal and vertical offset was used. Thus the tracking shows a slight influence on the (1,1,0) resonance due to closed orbit errors in the wiggler, although not with the measured strength. The different signs of the variations of the resonance width can be due to the different (and unknown) distributions of the coupling elements in the real machine and in the model used for the tracking.

The measurements of the dynamic acceptance agree with the tracking calculations made for different pole width. In chapter 4.3.2 a slight decrease of the acceptance has been calculated for a half pole width of $\approx 10\sigma_x$, which corresponds to the case of the beam center steered to 30mm horizontal amplitude in the wiggler. A small decrease of the horizontal acceptance has been measured for this case, while the vertical acceptance is still specified by the geometric aperture.

Wigglers with smaller pole widths than the ones presently used in DORIS would be acceptable from the beam dynamics point of view.

5.7 Wiggler with Large Multipole Errors

Experimental Method

The asymmetric wiggler ASYH was introduced in chapter 2.6 and 2.7. This device had a very strong sextupole component, which varied with the gap. The sextupole component is shown in the left figure 5.14. With fully closed gap, the sextupole due to the ASYH was four times stronger than that of the chromaticity correcting sextupoles.

Although tracking calculations indicated that it would have been impossible to operate DORIS with the ASYH closed, we tried to close the ASYH to the smallest gap possible. The sextupole effect was partly compensated by a lattice sextupole with an appropriate phase advance to the ASYH. This experiment gives a rigorous bound for the acceptable multipole error and verifies the quantitative predictions of the tracking calculations.

Measurements

Without the sextupole compensation, the ASYH could be closed down to 90 mm, which corresponds to a sextupole component of $b_2 = 17\text{T/m}$. The free area around the working point is reduced to $\Delta Q = \pm 0.0025$. Setting the lattice sextupole to its maximum strength which is $b_2 = -12.0\text{T/m}$ restores the free area to $\Delta Q = \pm 0.012$. With this sextupole setting, it is possible to close the ASYH to 70mm, corresponding to a sextupole strength of $b_2 = 24.0\text{T/m}$, which again gives the extremely reduced working area described above. By further closing the ASYH down to 60mm ($b_2 = 28\text{T/m}$), the lifetime is reduced to less than 30min., with no working point or parameters found which

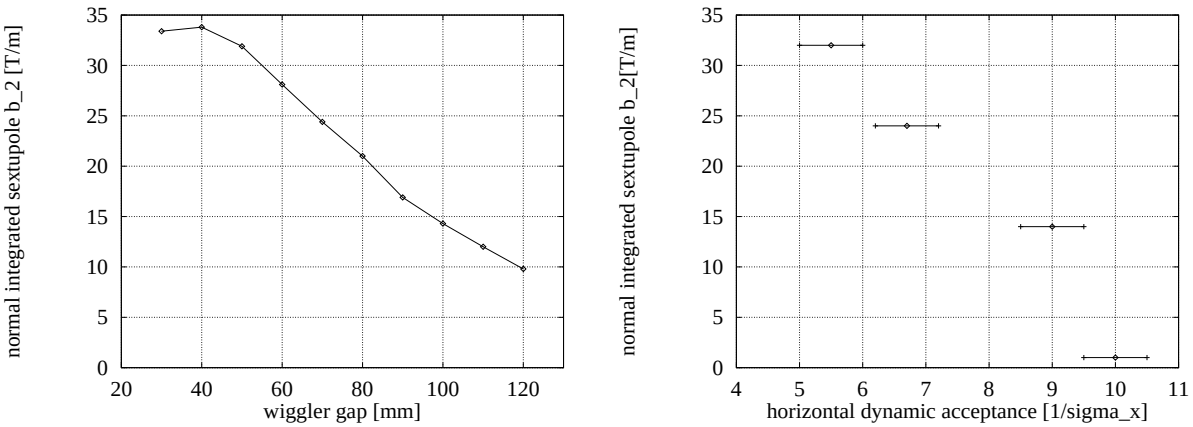

Figure 5.14: Left: *Normal integrated sextupole versus gap of the asymmetric wiggler ASYH before the correction with pole shims.*
Right: *Numerically calculated horizontal dynamic acceptance with the asymmetric wiggler and a sextupole kick with various strengths inserted in DORIS. The acceptance is given in units of the horizontal beam dimensions.*

increase the lifetime. The storage ring operates at its dynamic acceptance limit.

After a correction with pole shims, the multipole components were reduced to $b_2 = -0.46\mathrm{T/m}$ and $b_4 = 5400\mathrm{T/m}^3$ at the minimum gap, which allows the ASYH to be operated with no restrictions on the storage ring performance.

Discussion

The measurements of the storage ring behavior in the presence of the ASYH serve as an excellent proof of the predictive power of the single particle tracking. The right figure 5.14 shows the results of tracking calculations performed with the ASYH wiggler and a sextupole kick with various strengths inserted in the standard DORIS lattice. The horizontal acceptance has been calculated with a fixed initial coupling of $\approx 10\%$. At a sextupole strength of $b_2 = 24\mathrm{T/m}$ the calculated acceptance decreases to about $6\sigma_x$, which is in very good agreement with the observed lifetimes at the corresponding wiggler gap. The tracking thus gives a good quantitative prediction of the acceptance. Furthermore these measurements prove the validity of the multipole treatment of wiggler field errors, as investigated in chapter 4.3.3.

5.8 Influence of an Undulator on the Advanced Light Source

5.8.1 The 3rd Generation Light Source ALS

The Advanced Light Source at the Lawrence Berkeley Laboratory (LBL) in Berkeley is one of the first members of the new family of third generation light sources in operation. It is designed to generate small beam emittances and to provide much space for the insertion of undulators. The ALS can operate between 1 – 2 GeV, thus providing syn-

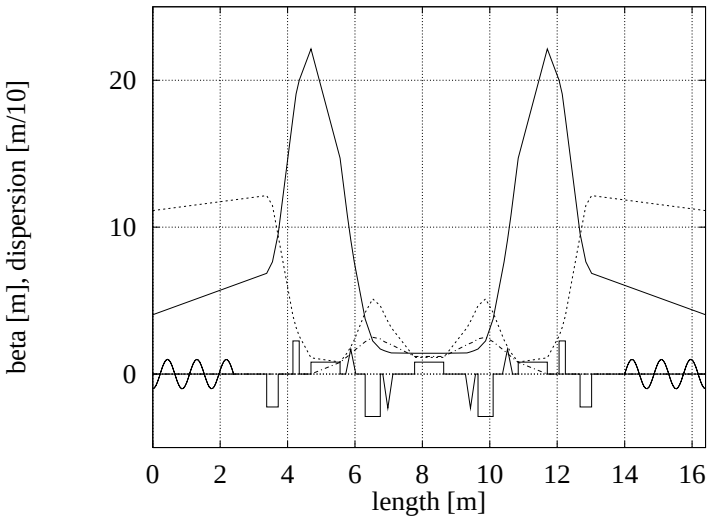

Figure 5.15: *Optical functions of one cell of the ALS. The boxes at the zero line symbolize the quadrupoles, the triangles the sextupoles and the wiggle the position of the undulators. The quadrupole magnets 3, 5 and 7 are combined function magnets providing the bending and vertical focusing.*
solid line: vertical β-function
dashed line: horizontal β-function
dashed-dotted line: horizontal dispersion

chrotron radiation in the ultra-violet and soft-X-ray regime. Commissioning started in 1993 [Jac93], and the ALS is now operating routinely to provide the increasing community of users with synchrotron radiation [Jac94]. A detailed description of the ALS may be found in [LBL86], [Sch89], some of the important parameters are listed in appendix C, while the optical functions of one cell of the storage ring are given in figure 5.15. The ALS is built from 12 of these cells, providing 10 straight sections for the installation of undulators and wigglers. In addition, all 36 bending magnets are equipped with synchrotron radiation ports.

The beam dynamics is dominated by the strong quadrupoles and sextupoles, the former are needed to control the beam size and the latter to compensate for the strong chromatic effects of the quadrupoles. The twelve-fold symmetry helps to minimize the effect of nonlinear resonances driven by the strong sextupoles. This becomes clear by looking to the Fourier coefficients of the perturbed Hamiltonian (3.16). In the presence of a lattice out of M identical pieces, the perturbation only contributes if the resonance condition

$$n_x Q_x + n_y Q_y + n_s Q_s = M \cdot n \tag{5.9}$$

is fulfilled.

Thus, the effects of an undulator, considering the nonlinear behavior of the machine, can be split into the symmetry break due to its linear focusing, which allows additional resonances to be driven by the sextupoles, and the nonlinear effects of the undulator itself [JFNZ89].

5.8.2 Measurement of Resonance Excitation caused by an Undulator

Experimental Method

Measurements have been performed to investigate the onset of resonances in the presence of an undulator or an artificial symmetry break caused by a quadrupole. The experimental technique differs from the one we used at DORIS.

Excited resonances may change the distribution of particles in the bunch and populate the beam tails. These can be measured by using a scraper to define the smallest geometric aperture and detect the showers which are created by particles hitting the scraper. An increased population of the tails will produce an increased counting rate in the detector behind the scraper. In principle this method is equivalent to the measurement of beam lifetime, but it is much faster and more sensitive. It allows many more tune points to be scanned and thus gives a more representative picture of the tune space. An investigation of more machine parameters is also possible. The experimental technique is described in some detail in [RCD+94].

The tune scans have been performed in the area marked in the tune diagram (figure 5.16). All resonances up to fifth order are plotted, the resonances allowed by the machines symmetry are emphasized. This section of the tune space was chosen because it

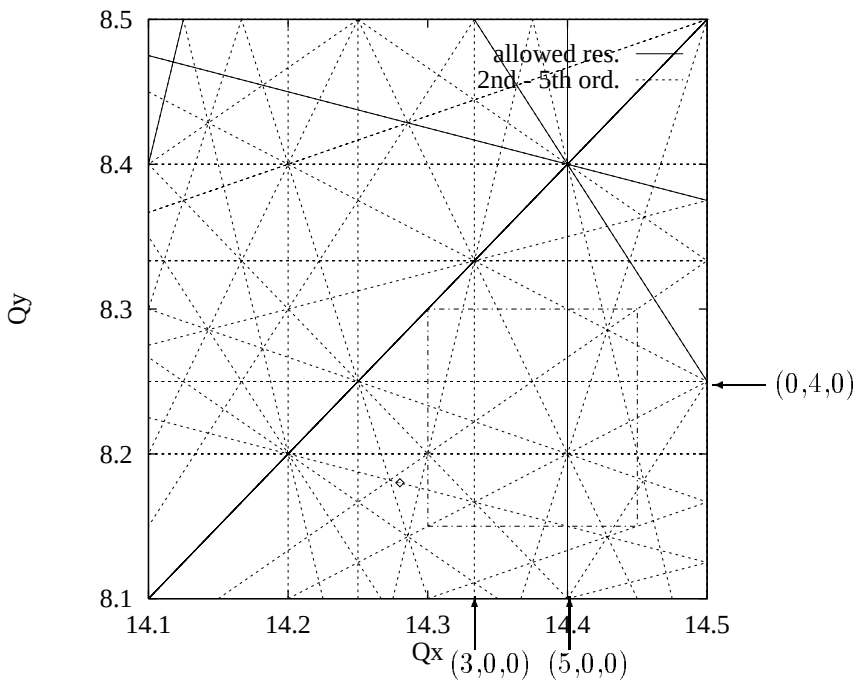

Figure 5.16: *Tune diagram with all betatron resonances up to 5th order. The resonances which are allowed by the machine symmetry are emphasized as solid lines. The normal ALS working point is marked as a diamond, the dashed dotted square indicates the investigated area of the tune diagram.*

covers the allowed resonance (5,0,0) as well as the unallowed (3,0,0), which is strongly driven by sextupoles. Furthermore the undulator driven resonance (0,4,0) crosses this

region.

Two tune scans have been performed in this region, one with the bare machine and the other with the undulator U8 closed in straight section 9. The parameters of the undulator are given in the following table:

gap [mm][c]	B_{max} [T]	λ [mm]	$\#_{ofperiods}$	length [m]
24.6	0.8	80	55	4.4

Measurements

The results are shown in figure 5.17, where the normalized count rate in a beam loss monitor down stream of the horizontal and vertical scraper is plotted versus the horizontal and vertical tunes.

The left figure shows the scan without the undulator. The resonances (3,0,0) and (2,1,0), both not allowed by symmetry, and the (5,0,0) are excited. There was no remarkable beam loss during this scan.

The right figure of 5.17 shows the same scan with the undulator closed. The resonance (3,0,0) and (2,1,0) are more pronounced, while the (5,0,0) remains unchanged. During this scan, approximately three quarters of the beam were lost during the various crossings of the (3,0,0) resonance.

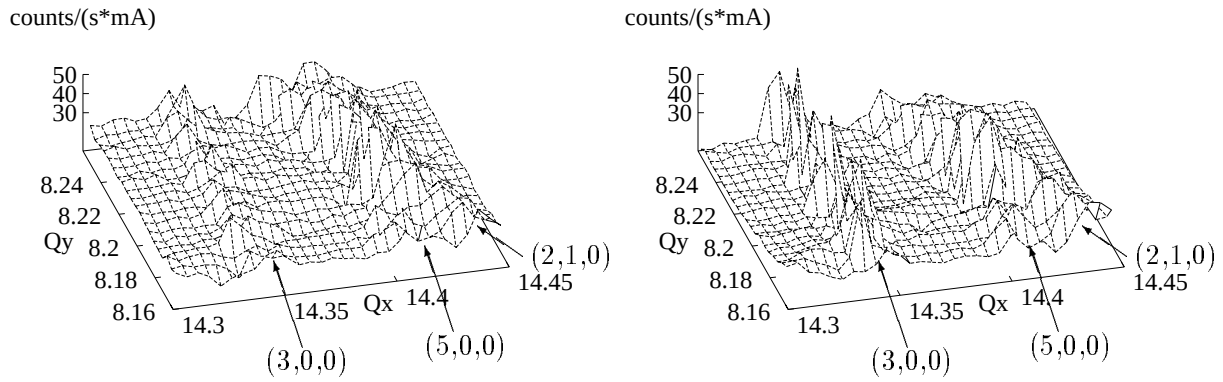

Figure 5.17: *Normalized count rate of photons, detected in a counter downstream of a horizontal and vertical scraper, versus horizontal and vertical tune. The tune was changed in steps of* $\Delta Q = 0.005$ *in each direction.*
Left: *ALS with no undulator*
Right: *undulator U8 closed to its minimum gap*

We get a more quantitative insight with line scans along a straight horizontal or vertical line in the tune diagram with a smaller step size for the tune changes. A scan with a fixed horizontal tune of $Q_x = 14.31$ is shown in figure 5.18. Despite of a small increase of the loss rate on the (1,-2,0) resonance, which has not been observed in the

[c]The ALS operated with commissioning vacuum chambers during these investigations, which allowed a minimum gap of 24.6mm. The maximum field of $B_{max} = 1.32$T will be reached at a gap of 14.0mm [ALS90].

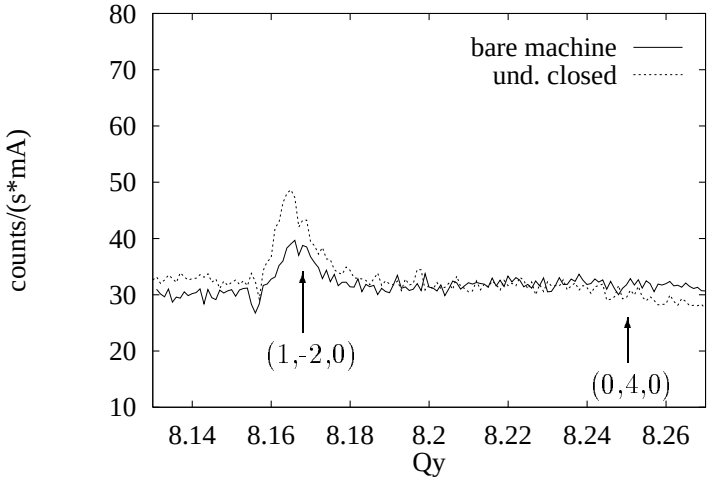

Figure 5.18: *Normalized count rate of photons, detected in a counter downstream of a vertical and horizontal scraper, versus vertical tune for the ALS without undulator (solid line) and with undulator U8 closed to its minimum gap (dashed line). The horizontal tune is fixed at* $Q_x = 14.31$*. The vertical tune was changed by steps of* $\Delta Q_y = 0.001$*.*

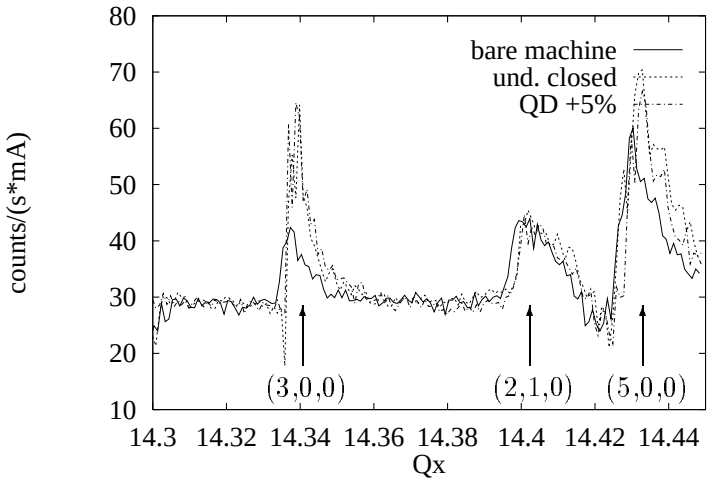

Figure 5.19: *Normalized count rate of photons, detected in a counter downstream of a vertical and horizontal scraper, versus horizontal tune for the ALS without any additional disturbance of the machine (solid line), with undulator U8 closed to its minimum gap (dashed line) and with a quadrupole detuned to match the linear optics distortion produced by the undulator (dashed dotted line). The vertical tune is fixed at* $Q_y = 8.15$*. The horizontal tune was changed by steps of* $\Delta Q_x = 0.001$*.*

raster scans above, no other resonance is observed. This is especially true for the (0,4,0), which is supposed to be driven by an undulator.

Figure 5.19 shows a horizontal tune scan with a fixed vertical tune of $Q_y = 8.15$. One can see clearly the excitation of the (3,0,0) and (2,1,0) resonances due to the closing of the undulator. To investigate the source of these resonances, we detuned a quadrupole

in the vicinity of the undulator such that it reproduces the optics distortion due to the linear focusing of the undulator. The dashed dotted line shows a line scan with the quadrupole set to a value equivalent to the vertical wiggler focusing. The quadrupole acts of course in both directions, thus the resulting additional maximum β-variation $\frac{\Delta\beta}{\beta}_{max.}$ is:

	$\frac{\Delta\beta}{\beta}_{max.}$	
	QD =3A	ideal undulator
horizontal	$\pm 2\%$	0%
vertical	$\pm 10\%$	$\pm 10\%$

Discussion

The beam loss rate with the detuned quadrupole is similar to the one produced by the undulator. Thus the main effect of the undulator is due to the optics distortion caused by the intrinsic vertical focusing and the horizontal focusing caused by magnetic field errors. The field error, which can be deduced from the resonance excitation measurement, agrees with the one obtained from tune shift measurements and the tolerable quadrupole gradient error [ALS90],[Dec94b]. The observed beam loss rate is quantitatively similar to that observed in an experiment where the effect of a horizontal optics distortion (i.e. symmetry break) on the (3,0,0) resonance was investigated [RCD+94]. The effect of the undulator can be successfully compensated by varying the optics with the help of a pair of quadrupoles on both sides of the corresponding straight section [RDK+95].

These measurements demonstrate the minor influence of the undulator nonlinearities on the beam dynamics of a third generation light source. The major effect is due to the disturbance of the linear optics. Resonances which are usually suppressed due to the machine symmetry can now be driven by the strong sextupoles in the machine.

6 Summary

This thesis analyzed the influence of wigglers and undulators on electron beam dynamics.

The analytical treatment emphasized the inclusion of the coupling between the transversal and longitudinal motion due to the placement of wigglers in dispersive regions. By applying a 6-dimensional Hamiltonian formalism, the excitation of 4th order synchro-betatron resonances could be demonstrated and the excitation coefficients have been derived.

The advantages of the current sheet model for permanent magnet blocks as opposed to the commonly used expansion series for periodic fields allowed the treatment of various wiggler magnetic field features. A fast tracking routine based on a numerical Taylor expansion for generating functions had to be implemented to make use of the current sheet method in single particle tracking. In this connection a comparison of different transfer maps for wigglers was performed, pointing out the advantages of the analytical and numerical generating function approach.

A detailed analysis of different field parameters gave design criteria for field errors and pole width: It could be shown that wiggler field errors are sufficiently described by a multipole expansion of the field integrals. The tune shift with amplitude as well as the dynamic acceptance were obtained using ideal wiggler models and multipole lenses, these agreed with the values derived from more realistic wiggler models using the current sheet method. Error limits for the multipole coefficients were derived on this basis.
The requirements on the periodicity of the wiggler fields are beyond those set by the quality requirements for the synchrotron radiation spectrum.
An analysis of the influence of the pole width showed the possibility of decreasing the pole width down to $\approx$ 15 standard deviations of the (Gaussian) horizontal beam size without decreasing the dynamic acceptance of the DORIS storage ring. The tools developed in the thesis allow an equivalent analysis for any other storage ring.

Tracking calculations indicated that the ideal wigglers would have minor influence on the DORIS storage ring. Including realistic field errors, new synchro-betatron resonances occur. The horizontal dynamic acceptance should decrease slightly, while the vertical dynamic acceptance remains unchanged. The vertical acceptance is determined by the geometric aperture, which is defined by the very narrow wiggler vacuum chambers.

The observations at DORIS are in very good agreement with these results. The free area in the tune diagram is reduced, especially due to the occurrence of 4th order synchro-betatron resonances, as predicted analytically. The vertical dynamic acceptance remains unchanged at a small value, while the horizontal acceptance decreases by 20 %.

Additional experiments on the special topics pole width and multipole errors verified the numerical results. The experiments on pole width verified the possibility of decreasing the wiggler pole width without an effect on the dynamic acceptance.

The linear influence of the wigglers on DORIS is sufficiently described by the intrinsic vertical focusing (tune shift) and the measured first and second field integrals (closed orbit distortion).

Measurements at the ALS underlined the importance of the linear optics distortion due to an undulator. The intrinsic vertical focusing and the small horizontal focusing due to field errors lead to an increase of resonance width. No evidence was found for resonances specifically driven by the undulator. These results agree with tracking calculations, where the change of the particle dynamics can either be simulated by an undulator or a quadrupole with appropriate strength. The nonlinear dynamics is determined by the strong lattice sextupoles.

The methods which have been developed here can serve as a basis for further analytical and numerical analysis of storage rings with wigglers and undulators, such as damping rings or 3rd generation light sources under construction.

The results of this thesis, and the experience at other synchrotron light sources, should encourage the extended integration of wigglers in storage rings, wherever they can be useful.

Acknowledgments

Many people were involved in the creation of this thesis by giving help, support, encouragement and advice. I am indebted to all of them.

I wish to thank Jörg Roßbach for making this work possible and for continuous support and interest.

I am indebted to the members of the DORIS-crew, namely Ortwin Kaul, Horst Nesemann and Bernd Sarau, for help, encouragement and support during the investigations at DORIS. They and the technicians and engineers of the shift-crews made it always worthwhile to spend nights and days in the control room.

I would like to thank all my colleagues and friends at DESY for innumerable suggestions and discussions, co-operation and help. Special thanks to Michael Böge, Werner Brefeld, Reinhard Brinkmann, Oliver Brüning, Jörg Feikes, Klaus Flöttmann, Bernhard Holzer, Michalea Marx, Anuschka Pauluhn, Joachim Pflüger, Anton Piwinski, Gustav-Adolf Voss, Ferdinand Willeke and Susan Wipf.

The friendly reception by the ALS staff during my research stay in 1994 is warmly acknowledged. Many people made it a pleasant, interesting and successful stay, among them are Alan Jackson, Rod Keller, Charles Kim, Hiroshi Nishimura, Greg Portmann, David Robin, Lindsay Schachinger, Greg Vierra and Alexander 'Sacha' Zholents.

Financial support was appreciated by the Deutsches Elektronen-Synchrotron DESY and the Deutscher Akademischer Austauschdienst (DAAD).

Finally, I wish to thank Oliver Brüning, Jörg Roßbach, Susan Wipf and Joachim Pflüger for reading the manuscript.

Appendix

A Numerical Evaluation of Multipole Coefficients from Field Integral Measurements

A measured field integral value $I_x(x_i, y_i)$, $I_y(x_i, y_i)$ at the position $(x_i,\, y_i)$ is fitted by a multipole expansion:

$$\begin{aligned} I_x(x_i, y_i) &= \sum_{n=0}^{\mathcal{O}} -\mathrm{Re}(x_i + \mathrm{i}y_i)^n\, a_n + \mathrm{Im}(x_i + \mathrm{i}y_i)^n\, b_n \\ I_y(x_i, y_i) &= \sum_{n=0}^{\mathcal{O}} \mathrm{Im}(x_i + \mathrm{i}y_i)^n\, a_n + \mathrm{Re}(x_i + \mathrm{i}y_i)^n\, b_n \end{aligned}$$

where $\mathcal{O}$ is the order of the expansion and a_n the skew, b_n the normal coefficients. To derive the multipole coefficients from a set of N measured field integral points, it is convenient to write the N equations of the multipole expansion in a matrix form:

$$\begin{pmatrix} \vdots & \vdots & \ddots & \vdots & \vdots \\ -\mathrm{Re}(x_i + \mathrm{i}y_i)^0 & \mathrm{Im}(x_i + \mathrm{i}y_i)^0 & \ddots & -\mathrm{Re}(x_i + \mathrm{i}y_i)^{\mathcal{O}} & \mathrm{Im}(x_i + \mathrm{i}y_i)^{\mathcal{O}} \\ \vdots & \vdots & \ddots & \vdots & \vdots \\ -\mathrm{Re}(x_N + \mathrm{i}y_N)^0 & \mathrm{Im}(x_N + \mathrm{i}y_N)^0 & \ddots & -\mathrm{Re}(x_N + \mathrm{i}y_N)^{\mathcal{O}} & \mathrm{Im}(x_N + \mathrm{i}y_N)^{\mathcal{O}} \\ \vdots & \vdots & \ddots & \vdots & \vdots \\ \mathrm{Im}(x_i + \mathrm{i}y_i)^0 & \mathrm{Re}(x_i + \mathrm{i}y_i)^0 & \ddots & \mathrm{Im}(x_i + \mathrm{i}y_i)^{\mathcal{O}} & \mathrm{Re}(x_i + \mathrm{i}y_i)^{\mathcal{O}} \\ \vdots & \vdots & \ddots & \vdots & \vdots \\ \mathrm{Im}(x_N + \mathrm{i}y_N)^0 & \mathrm{Re}(x_N + \mathrm{i}y_N)^0 & \ddots & \mathrm{Im}(x_N + \mathrm{i}y_N)^{\mathcal{O}} & \mathrm{Re}(x_N + \mathrm{i}y_N)^{\mathcal{O}} \end{pmatrix}$$

$$\cdot \begin{pmatrix} a_0 \\ b_0 \\ \vdots \\ a_{\mathcal{O}} \\ b_{\mathcal{O}} \end{pmatrix} = \begin{pmatrix} \vdots \\ I_{x,i} \\ \vdots \\ I_{x,N} \\ \vdots \\ I_{y,i} \\ \vdots \\ I_{y,N} \end{pmatrix} . \qquad \text{(A.1)}$$

This reads in matrix notation:

$$\mathbf{X}\vec{a} = \vec{I} \quad .$$

To solve these system of equations with measured field integrals, one has to minimize the error vector $\vec{e}$ of the equation $\mathbf{X}\vec{a} - \vec{I} = \vec{e}$, with $\mathbf{X}$, $\vec{a}$ and $\vec{I}$ defined above. This is easily done with the Gaussian principle :

$$\sum_{i=1}^{N}(\vec{X}_i\vec{a} - \vec{I})^2 = \sum_{i=1}^{N}\vec{e}^2 \stackrel{!}{=} \min \tag{A.2}$$

which leads by differentiating partially to the a_n, b_n to the Gaussian normal equations. An alternative and numerically stable way of solving (A.2) is the method of Householder [Bih93],[EMR88].

B Beam Lifetime in Electron Storage Rings

This section gives a summary of the lifetime limiting effects in electron storage rings (see for example [Wru94]). All these effects are somehow related to an aperture limitation in the transversal ($\Delta_{x,y}$) or longitudinal plane (Δ_s). These limitations are either geometric or dynamical in the transversal plane, respectively given by the rf-acceptance or the momentum acceptance of the storage ring for the longitudinal plane.

- Quantum lifetime

The lifetime due to the radiation damping and quantum fluctuation in electron storage rings is:

$$\tau_q = \tau_D \frac{\varepsilon\beta}{\Delta^2_{x,y,s}} \exp\left(\frac{\Delta^2_{x,y,s}}{2\varepsilon\beta}\right) \tag{B.1}$$

where the damping time τ_D is given by the synchrotron radiation integrals [Wal94]. The above equation is equally valid in the transversal and longitudinal planes, with the damping time calculated for the particular plane. The emittance ε and the $\beta-$function have been defined in chapter 3.1. Usually the quantum excitation dominates the lifetime for aperture limits below $6\sqrt{\varepsilon\beta}$. Equation (B.1) is only valid as long as the distribution function of the particles in the beam is approximately Gaussian. For aperture limitations from $4 - 6\sqrt{\varepsilon\beta}$, the emittance can be evaluated by fitting (B.1) to measured lifetime versus aperture limitation data. The solution of the Fokker-Planck equation determining the beam profile gives not longer a Gaussian distribution for aperture limitations smaller than $\approx 4\sqrt{\varepsilon\beta}$.

- Elastic gas scattering

If a particle is scattered elastically (Rutherford scattering) on a nucleus of the remaining gas in the machine, it increases its betatron amplitude and may get lost at the transversal aperture. The lifetime depends on the average pressure $< P >$ and constitution of the residual gas, thus giving:

$$\tau_{el} \sim \frac{1}{< \beta >< P >} E_0^2 \frac{\Delta^2_{x,y}}{\beta} \tag{B.2}$$

The elastic scattering lifetime gets shorter for small energy (E_0) machines and high average β-functions $< \beta >$.

• Inelastic gas scattering

By an inelastic scattering with the residual gas the particle changes its energy and can exceed the longitudinal acceptance Δ_s, which is the maximum accepted energy deviation. The lifetime becomes:

$$\tau_{inel} \sim f_1 \ln\left(\frac{1}{\Delta_s} - \frac{5}{8}\right) + f_2 \ln\left(\frac{1}{\Delta_s} - 1\right) \tag{B.3}$$

where f_1, f_2 are given by the gas properties.

• Touschek and intrabeam scattering

Touschek scattering and intrabeam scattering describes the scattering effects of particles within a bunch. The lifetime due to Touschek scattering is proportional to the particle density within the bunch and the momentum acceptance [Wru94].

$$\tau_{touschek} \sim \frac{\sqrt{\varepsilon_x^2 \varepsilon_y \beta_y} \sigma_s E_0^3}{I_{bunch}} \Delta_s^2$$

with I_{bunch} the bunch current and σ_s one standard deviation of the longitudinal particle distribution. $\tau_{touschek}$ limits the lifetimes of all small emittance and low energy machines such as the ALS.

• Charged particle trapping

The lifetime can considerably decrease by the trapping of charged particles. These particles get ionized due to a scattering process with a beam particle and are attracted by the electromagnetic forces of the circulating beam. This will locally increase the vacuum pressure. Among others, the electron storage ring of HERA as well as DORIS suffered form the trapping of charged dust particles [Zim93], which finally lead to the usage of positrons.

The lifetime depends on the beam current and charge distribution in the storage ring, the trapping may only occur above a certain threshold of the beam current.

C Parameter Lists of DORIS III and the ALS

The main parameters of the storage rings DORIS III and ALS are summarized in table C.1 and table C.2.

Table C.3 gives an extended set of parameters for all wigglers and undulators used in DORIS. In addition to the data given in table 4.1, the critical energy and the wiggler parameter K are printed.

Table C.1: *Parameters of DORIS III*

circumference	289 m
energy	4.5 GeV
Current and Lifetimes	
I_{max}	$\approx$ 140 mA in 5 Bunches
τ (140 mA)	14 h
Tunes	
Q_x	7.18
Q_y	4.26 / 4.76
Q_s	0.04 – 0.06
Emittances	
ε_x	0.44 π mrad mm
$\varepsilon_z/\varepsilon_x$	2% – 4%
$\Delta p/p$	0.1%
Damping Times	
transversal	$\approx$ 3 msec ($\hat{=}$ 3000 turns)
longitudinal	$\approx$ 1.5 msec ($\hat{=}$ 1500 turns)
Optical Functions at ID-positions	
$\beta_x = 5 - 22$ m	$\beta_y = 5 - 21$ m
$D_x = 20 - 80$ cm	$D_y = 10 - 20$ cm

Table C.2: *Parameters of the ALS*

circumference	196.8 m
energy	1 – 2 GeV
Current and Lifetimes	
I_{max}	400 mA in up to 328 Bunches
τ (400 mA)	10 – 18 h
Tunes	
Q_x	14.28
Q_y	8.20
Emittances	
ε_x	4 π mrad μm
$\varepsilon_z/\varepsilon_x$	$\approx$ 5%
$\Delta p/p$	0.7% in multi bunch mode
$\Delta p/p$	0.07% in single bunch mode
Damping Times	
horizontal	$\approx$ 13.1 msec ($\hat{=}$ 20,000 turns)
vertical	$\approx$ 17.6 msec ($\hat{=}$ 26,000 turns)
longitudinal	$\approx$ 10.7 msec ($\hat{=}$ 16,000 turns)
Optical Functions at ID-positions	
$\beta_x = 11$ m	$\beta_y = 4$ m
$D_x = 0.0$ cm	$D_y = 0.0$ cm

Table C.3: *List of DORIS III wiggler and undulator parameters*

name of wiggler	short name	λ cm	number of periods	B_{max} T	gap cm	$1/f$ m^{-1}	o m^{-3}	K	E_c KeV	#
X-Ray Wiggler	X-WIG	14.0	28	1.17	3.0	.012	16.0	13.6	15.8	4
Hard X-Ray Wiggler	*HARWI2*	*22.6*	*17*	*2.0*	*2.0*	*.036*	*18.6*	*34.0*	*27.0*	*1*
Asymmetric Wiggler	ASYH	22.0	18	max. 1.17 / min. -0.6	3.0	.005	2.7	15.0	15.7	*1*
Triple XUV Undulator[a]	*XUV I*	*9.0*	*44*	*0.56*	*3.0*	*.003*	*9.7*	*4.7*	*7.5*	*1*
	XUV II	*12.0*	*33*	*0.50*	*3.0*	*.002*	*3.7*	*5.6*	*6.8*	*1*
	XUV III	*18.6*	*21*	*0.66*	*3.0*	*0.004*	*3.0*	*11.5*	*8.9*	*1*
X-Ray Undulator	XU	3.14	127	0.8	1.4	.006	160	2.25	10.8	1
X-Ray Wiggler	HARWI	24.	10	1.25	3.0	.008	3.7	26.9	16.1	1
Wiggler-Undulator	W1	*13.2*	*16*	*0.6*	*3.0*	*.002*	*3.0*	*7.4*	*8.1*	*1*
Mini-Wiggler	W3	12.	4	0.3	5.8			3.5	4.2	1
Bending Magnet	BM			1.25					16.8	24

[a] 3 structures mounted onto one girder.

The following tables C.4 and C.5 summarize the theoretical optical functions as well as the minimum vertical gap for all wiggler and undulator locations in DORIS III. The values are both given for the optics ATH1 and BTH1 for the cases all wigglers open and all wigglers closed and tune shift corrected.

Table C.4: *Optical functions at wiggler locations for the optics ATH1*

		no wigglers				all wigglers[a]			
name	vert. aperture mm	β_x m	α_x rad	β_y m	α_y rad	β_x m	α_x rad	β_y m	α_y rad
BW1	10	16.52	0.00	4.13	0.00	16.29	-0.95	3.11	0.04
BW2	24	8.98	0.00	24.09	0.00	9.40	-0.14	30.66	-0.32
BW3	24	21.02	0.00	10.38	0.00	22.61	0.01	11.48	0.42
BW4	24	1.64	0.00	8.93	0.00	1.75	0.00	6.75	0.04
BW5	16	21.02	0.00	10.38	0.00	22.63	-0.01	10.26	-0.25
BW6	24	8.98	0.00	24.09	0.00	9.41	0.14	22.70	0.32
BW7	24	16.52	0.00	4.13	0.00	16.28	0.95	3.63	-0.28
W1	50	6.44	-0.01	12.16	-0.09	6.90	-0.01	12.74	0.26
W2	24	13.53	2.74	8.54	-3.17	13.88	2.84	10.87	-3.91
W3	50	2.75	0.37	10.21	-0.94	2.57	0.37	8.15	-0.96

Table C.5: *Optical functions at wiggler locations for the optics BTH1*

		no wigglers				all wigglers[a]			
name	vert. aperture mm	β_x m	α_x rad	β_y m	α_y rad	β_x m	α_x rad	β_y m	α_y rad
BW1	10	16.35	0.00	4.88	0.00	16.13	-1.28	4.50	0.31
BW2	24	10.11	0.00	20.79	0.00	10.13	-0.06	19.11	-0.17
BW3	24	22.03	0.00	8.73	0.00	22.11	0.00	9.27	-0.02
BW4	24	1.58	0.00	7.71	0.00	1.74	0.00	8.23	0.07
BW5	16	22.03	0.00	8.73	0.00	22.12	0.00	7.74	0.11
BW6	24	10.11	0.00	20.79	0.00	10.14	0.07	15.19	0.01
BW7	24	16.35	0.00	4.88	0.00	16.13	1.28	5.61	-0.39
W1	50	8.13	-0.01	9.98	-0.01	8.10	-0.01	11.76	-0.25
W2	24	14.45	2.50	21.96	-2.98	14.55	2.51	17.64	-2.21
W3	50	2.49	0.54	8.61	-1.18	2.49	0.54	7.90	-0.82

[a]The XU at BW1, an X-WIG at BW2, BW4, BW6 and BW7, the HARWI2 at BW5, the XUV at BW3 and the HARWI at position W2 are inserted.

Bibliography

[ALS90] ALS Insertion Device Design Group. U8.0 undulator conceptual design report. *LBL PUB-5276*, 1990.

[B+90] M. Bartsch et al. MAFIA release 3: The new version of the general purpose electromagnetic design code family. *DESY M-90-05K*, 1990.

[BBH+95] K. Balewski, W. Brefeld, U. Hahn, J. Pflüger, and R. Rossmanith. PETRA II - a synchrotron radiation source at DESY. *Proc. Particle Accelerator Conference, Dallas, (to be published)*, 1995.

[Bel87] J.S. Bell. Hamiltonian mechanics. *Proc. CERN Accelerator School Advanced Accelerator Physics, Oxford, CERN 87-03*, pages 5–40, 1987.

[BES89] BESSY. *BESSY II - Eine optimierte Undulator/Wiggler- Speicherring Lichtquelle für den VUV- und XUV-Spektralbereich - 2.Teil: Technische Studie*, 1989.

[BHHW83] G. Brown, K. Halbach, J. Harris, and H. Winick. Wiggler and Undulator Magnets - a Review. *Nuclear Instruments and Methods A208*, pages 65–77, 1983.

[BHRW94] D.P. Barber, K. Heinemann, G. Ripken, and F. Willeke. Notes on synchro-betatron coupling for particles of arbitrary energy using a 6-dimensional symplectic dispersion formalism. *DESY HERA 94-02*, 1994.

[Bih93] M. Bihn. Multipolentwicklung numerisch berechneter Felder in Beschleunigermagneten. Diplomarbeit, Technische Hochschule Darmstadt, 1993.

[BMRW86] D.P. Barber, H. Mais, G. Ripken, and F. Willeke. Nonlinear theory of coupled synchro-betatron motion. *DESY 86-147*, 1986.

[BNR88] W. Brefeld, H. Nesemann, and J. Roßbach. The bypass project at DORIS III. *Proc. 1st European Particle Accelerators Conference, Rome*, pages 389–391, 1988.

[Bre] W. Brefeld. private communication.

[Bru92] P. Brunelle. Beam Dynamics with four Undulators on Super-ACO: Experimental and Theoretical Results. *Particle Accelerators 39*, pages 89–106, 1992.

[BS89] I.N. Bronstein and K.A. Semendjajew. *Taschenbuch der Mathematik*. Verlag Harri Deutsch, 1989.

[BW90] J. Bahrdt and G. Wüstefeld. A new tracking routine for particles in undulator and wiggler fields — Part I,II and III. *BESSY TB 90-158 and BESSY TB 90-163*, 1990.

[BW92] J. Bahrdt and G. Wüstefeld. A Taylor-expanded generating function for particle motion in arbitrary magnetic fields. *Proc. 3rd European Particle Accelerator Conference, Berlin*, pages 670–672, 1992.

[CS58] E.D. Courant and H.D. Snyder. Theory of the Alternating-Gradient Synchrotron. *Annals of Physics 3*, pages 1–48, 1958.

[Dec94a] W. Decking. Influence of insertion devices on the beam dynamics of DORIS III. *Proc. 4th European Particle Accelerator Conference, London*, pages 1003–1005, 1994.

[Dec94b] W. Decking. What is wrong with 9U ? ALS internal note, 1994.

[Dec94c] W. Decking. Wiggler und Undulatoren in DORIS III. *Proc. HERA-Seminar, Bad Lauterberg, DESY HERA 94-03*, pages 219–244, 1994.

[Dec95] W. Decking. Treatment of wiggler and undulator field errors in tracking codes. *Proc. Particle Accelerator Conference, Dallas, (to be published)*, 1995.

[DES94] DESY. *Koloquium 30 Jahre Synchrotronstrahlung am Deutschen Elektronen-Synchrotron DESY*, 1994.

[EG54] W.C. Elmore and M.W. Garrett. Measurement of two-dimensional Fields (Part I). *Review of Scientific Instruments 25*, pages 480–485, 1954.

[EMR88] G. Engeln-Müllges and F. Reuter. *Formelsammlung zur numerischen Mathematik mit Standard-Fortran-77-Programmen.* BI Wissenschaftsverlag, 1988.

[FO92] É. Forest and K. Ohmi. Symplectic integration for complex wigglers. *KEK-Report-92-14*, 1992.

[FP82] M.W. Fan and M.W. Poole. PMU3D - a program for three dimensional field calculations on periodic permanent magnet systems. *Daresbury Laboratory DL/SCI/TM 29 A*, 1982.

[Gol85] H. Goldstein. *Klassische Mechanik.* Aula-Verlag, 1985.

[Gui78] G. Guignard. A general treatment of resonances in accelerators. *CERN 78-11*, 1978.

[Gür] P. Gürtler. private communication.

[H+] K. Halbach et al. PANDIRA is an improved version of the POISSON codes to calculate two dimensional magnet field problems.

[Hag57] R. Hagedorn. Stability and amplitude ranges of two-dimensional non-linear oscillations with periodical Hamiltonian. *CERN 57-1*, 1957.

[Hal81] K. Halbach. Fields of Undulators and Wigglers. *Nuclear Instruments and Methods A187*, pages 109–177, 1981.

[Hal86] K. Halbach. Concepts for Insertion Devices that will produce high quality Synchrotron Radiation. *Nuclear Instruments and Methods A246*, pages 77–81, 1986.

[Hän92] R. Hänsel. The European Synchrotron Radiation Facility ESRF in Grenoble. *IEEE Transactions on Nuclear Science 39*, pages 44–48, 1992.

[HAS94] HASYLAB, DESY. *Jahresbericht 1994 - Hamburger Synchrotronstrahlungslabor HASYLAB*, 1994.

[Hof90] A. Hofmann. Characteristics of synchrotron radiation. *Proc. CERN Accelerator School Synchrotron Radiation and Free Electron Lasers, Chester, CERN 90-03*, pages 115–141, 1990.

[Jac82] J.D. Jackson. *Klassische Elektrodynamik*. W. de Gruyter, 1982.

[Jac93] A. Jackson. Commissioning and performance of the Advanced Light Source. *Proc. Particle Accelerator Conference, Washington*, pages 1432–1435, 1993.

[Jac94] A. Jackson. Performance of the Advanced Light Source. *Proc. 4th European Particle Accelerator Conference, London*, pages 107–109, 1994.

[JFNZ89] A. Jackson, É. Forest, H. Nishimura, and M.S. Zisman. The effects of insertion devices on the beam dynamics in the ALS. *LBL-25958*, 1989.

[Kau94] O. Kaul. Lebensdauerprobleme in DORIS. *Proc. HERA-Seminar, Bad Lauterberg, DESY HERA 94-03*, pages 245–269, 1994.

[KB90] P. Kuske and J. Bahrdt. Influence of the BESSY undulator on the beam dynamics. *BESSY TB 90-152*, 1990.

[LBL86] LBL. *1 – 2 GeV Synchrotron Radiation Source - Conceptual Design Report. LBL PUB-5172 Rev.*, 1986.

[N+92] H. Nesemann et al. First experience with DORIS III. *Proc. XVth International Conference on High Energy Accelerators, Hamburg*, pages 549–551, 1992.

[Pfla] J. Pflüger. Field integrals of the ASYH. private communication.

[Pflb] J. Pflüger. Field measurements on DORIS wigglers.

[Pfl92] J. Pflüger. Insertion Devices for DORIS III. *Review of Scientific Instruments 63*, pages 295–300, 1992.

[Pfl93a] J. Pflüger. Magnetic measurements on the asymmetric hybrid structure (ASYH) for DORIS III. *Proc. International Workshop on Magnetic Measurements of Insertion Devices, Argonne*, pages 213–241, 1993.

[Pfl93b] J. Pflüger. New insertion device developments at HASYLAB. *Proc. Workshop on Electron Beam Sources of High Brightness Radiation, San Diego*, pages 102–109, 1993.

[Piw93] A. Piwinski. Synchrotron sidebands of betatron coupling resonances. *DESY 93-189*, 1993.

[PW76] A. Piwinski and A. Wrulich. Excitation of betatron-synchrotron resonances by a dispersion in the cavities. *DESY 76-07*, 1976.

[RCD+94] D. Robin, H. Collins, W. Decking, G. Portmann, L. Schachinger, and A. Zholents. Observation of nonlinear resonances in the Advanced Light Source. *Proc. Workshop Nonlinear Dynamics in Particle Accelerators, Arcidosso, (to be published)*, 1994.

[RDK+95] D. Robin, W. Decking, G. Krebs, G. Portmann, and A. Zholents. Reduction of non linear resonance excitation from insertion devices in the ALS. *Proc. Particle Accelerator Conference, Dallas, (to be published)*, 1995.

[Rip85] G. Ripken. Nonlinear canonical equations of coupled synchro-betatron motion and their solution within a framework of a nonlinear 6-dimensional (symplectic) tracking program for ultra-relativistic protons. *DESY 85-84*, 1985.

[RS94] J. Roßbach and P. Schmüser. Basic course on accelerator optics. *Proc. CERN Accelerator School General Accelerator Physics, Jyvaeskylae, CERN 94-01*, pages 17–88, 1994.

[San70] M. Sands. The physics of electron storage rings. *SLAC report 121*, 1970.

[Sch49] J. Schwinger. On the Classical Radiation of Accelerated Electrons. *Physical Review 75*, pages 1912–1932, 1949.

[Sch57] A. Schoch. Theory of linear and non-linear perturbations of betatron oscillations in alternating-gradient synchrotrons. *CERN 57-21*, 1957.

[Sch89] A.S. Schlachter. The Advanced Light Source : a new 1.5 GeV synchrotron radiation facility at the Lawrence Berkeley Laboratory. *LBL-27437*, 1989.

[Sch91] F. Schmidt. SIXTRACK. *CERN/SL/91-52(AP)*, 1991.

[Sch92] M. Scheer. Effects of a superconducting wavelength shifter on the planned storage ring BESSY II — Part I: Canonical tracking calculations. *BESSY TB 92-169-A*, 1992.

[SHH+90] R. Savoy, K. Halbach, W. Hassenzahl, E. Hoyer, D. Humphries, and B. Kincaid. Calculation of Magnetic Errors in Hybrid Insertion Devices. *Nuclear Instruments and Methods A291*, pages 408–412, 1990.

[Smi86] L. Smith. Effect of insertion devices on beam dynamics. *ESG TECH NOTE-24*, 1986.

[Tos88] L. Tosi. Effects of insertion devices on beam dynamics. *Sincrotrone Trieste ST/M-88/25*, 1988.

[Wal94] R.P. Walker. Quantum excitation and equilibrium beam properties. *Proc. CERN Accelerator School General Accelerator Physics, Jyvaeskylae, CERN 94-01*, pages 481–498, 1994.

[WB91] G. Wüstefeld and J. Bahrdt. Canonical particle tracking in undulator fields. *Proc. Particle Accelerator Conference, San Francisco*, pages 266–268, 1991.

[Wil90] F. Willeke. Analysis of particle tracking data. *Proc. CERN Accelerator School Advanced Accelerator Physics, Uppsala, CERN 90-04*, pages 156–183, 1990.

[Win87] H. Winick. Synchrotron Radiation. *Scientific American 257*, pages 72–81, 1987.

[WR88] F. Willeke and G. Ripken. Methods of beam optics. *DESY 88-114*, 1988.

[Wru84] A. Wrulich. RACETRACK. *DESY 84-026*, 1984.

[Wru88] A. Wrulich. The simulation of insertion device effects on single particle motion with racetrack. *Sincrotrone Trieste ST/M-88/12*, 1988.

[Wru94] A. Wrulich. Single-beam lifetime. *Proc. CERN Accelerator School General Accelerator Physics, Jyvaeskylae, CERN 94-01*, pages 409–435, 1994.

[Zim93] F. Zimmermann. Trapped dust in HERA and DORIS. *DESY 93-08*, 1993.